Intrinsic Point Defects in a-SiO_2 with Embedded Si Nanoparticles Probed by ESR

Mihaela Andreea Jivănescu

Promotor:
Prof. Dr. André Stesmans

Jury members:
Prof. Dr. Margit Zacharias, University of Freiburg - IMTEK
Dr. Liviu Giurgiu, INCDTIM, Cluj-Napoca
Dr. Geoffrey Pourtois, IMEC, Leuven
Prof. Dr. Chris Van Haesendonck, KULeuven
Prof. Dr. Valery Afanas'ev, KULeuven
Prof. Dr. Michel Houssa, KULeuven

Dissertation presented in partial
fulfillment of the requirements
for the degree of
Doctor in Science

June 2010

Legal depot number D/2010/10.705/43
ISBN number ISBN 978-90-8649-350-0

Thank you word

For this thesis to exist I had the support of many people in different areas of my life, to whom I want to thank here.

I want to thank my promoter Prof. Dr. André Stesmans for teaching me science, ESR and much more, through stimulating discussions, but also how to write a good text and for the time he put in thoroughly correcting this thesis and the articles I wrote. I appreciate very much his dedication for science and teaching it to us, his students.

I also want to thank the members of the jury, Prof. Dr. Margit Zacharias, Dr. Liviu Giurgiu, Dr. Geoffrey Pourtois, Prof. Dr. Chris Van Haesendonck, Prof. Dr. Valery Afanas'ev, and Prof. Dr. Michel Houssa for the evaluation of this thesis and the stimulating discussions we had.

For the fruitful collaboration and nice friendship, I want to thank Stefanie and Daniel.

The people in Semiconductor Physics group welcomed me and made my days at KUL a lot nicer, for which I thank them. Koen, Monica, Ellen, Pieter, Sheron, Duc, Mugwort, Hsing-Yi, Francesca, Thoan, Sang, Emilio, Mikhail, Rao and Gonda made science, lunches, breaks and parties a lot more fun. I want to thank Gonda also for helping me very much with all the administrative things.

Şi nu în ultimul rînd, vreau să mulţumesc familiei pentru suportul neconditionat pe care mi l-a dat toţi aceşti ani. George, sotul meu, vreau să iţi multumesc pentru că mi-ai fost alături, m-ai încurajat şi mi-ai ridicat moralul în aceşti ani cu multe seri prin laborator. Am avut şi prieteni extraordinari, atata in Leuven cand si in alte parti ale lumii, care sa mă inveseleasca şi incurajeze şi carora vreau sa le multumesc.

Contents

List of symbols

$\hat{A}$	hyperfine matrix
a	hyperfine splitting constant
a_{iso}, a_{aniso}	the isotropic and anisotropic components of a
$a_{\parallel}$, $a_{\perp}$	the parallel and perpendicular components of a
$\overrightarrow{\mathrm{B}}$	magnetic field
$\mathrm{B_l}$	local magnetic field
B_m	magnetic field modulation amplitude
B_μ	microwave field amplitude
$\Delta\mathrm{B}_{pp}$	peak-to-peak line width
χ	magnetic susceptibility
η	natural abundance
g, $\hat{g}$	spectroscopic splitting factor/ matrix
g_0	free electron g factor
g_c	zero crossing g value; central g value
$\mathrm{g}_{\parallel}$, $\mathrm{g}_{\perp}$	parallel and perpendicular components of an axial $\hat{g}$
g_{iso}, g_{aniso}	the isotropic and anisotropic components of g
g_1, g_2, g_3	principal g values
h	Planck's constant
$\mathcal{H}_S$	spin Hamiltonian
I	nuclear spin
$\mathcal{I}$	signal intensity (area under ESR absorption curve)
κ	dielectric constant
$\overrightarrow{J}$	total angular momentum
$\overrightarrow{L}$	orbital angular momentum
λ	spin-orbit coupling constant
μ	magnetic moment
μ_0	free space magnetic permeability
ν	microwave frequency
N_s	number of spins
N_{ref}	number of spins in the marker sample
P_μ	microwave power

Ψ	wave function
Q	quality factor
R_{hf}	the ratio of the intensity of a hf multiplet to the main Zeeman resonance line
$\overrightarrow{S}$	electron spin
T	measurement temperature
T_{an}	annealing temperature
T_C	Curie temperature
T_1	spin-lattice relaxation time

List of abbreviations

a-	amorphous
AFM	atomic force microscopy
c-	crystalline
CMOS	complementary MOS
C-V	capacitance-voltage
CVD	chemical vapor deposition
cw	continuous wave
DB	dangling bond
DFT	density functional theory
ED	electron diffraction
EFM	electrostatic force microscopy
ESR	electron spin resonance
FWHM	full width at half maximum
hf	hyperfine
G-V	conductance-voltage
HRTEM	high-resolution transmission electron microscopy
I-V	current-voltage
LCAO	linear combination of atomic orbitals
LED	light-emitting diode
MOS	metal-oxide-semiconductor
MOSFET	metal-oxide-semiconductor field-effect transistor
n-	nano
np	nanoparticle
nc	nanocrystalline
ODC	oxygen deficient center
OHC	oxygen-related hole center
PDA	post-deposition annealing
PIA	post-implantation annealing
PCVD	plasma chemical vapor deposition
p-	porous
PL	photoluminescence

PES	photoelectron spectroscopy
SAXS	small angle X-ray scattering
TEM	transmission electron microscopy
US	ultrasonic
UST	ultrasonic treatment
UV	ultra violet
VUV	vacuum ultra violet

Introduction

People like to express enthusiasm with extremes: biggest, smallest, fastest, highest etc. When it comes to technology and consumer market, having the smallest gadgets with highest performance is the thing everybody wishes for. The evolution from the initial computer filling a large room to the current small laptops and smart phones that fit in the palm of your hand and are being even more powerfull in performance is due to the possibility of integrating an ever larger number of transistors on a chip, increasing performance and decreasing costs. A smart phone you can buy today is much faster and much smaller than the computer for which you paid almost a fortune not longer than 15 years ago. This is the silicon-based revolution.

Silicon, as enabler of the current information age, keeps running high. What keeps it so attractive for the electronics technology draws on various facts, such as unlimited resources, availability of a superb natural insulator (SiO_2), good thermal and mechanical properties and, as a result of the unprecedented technological and scientific efforts invested over decades, the extraordinary progress reached in material assets, e.g, the extremely high level of purification. Yet, while still accounting for more than 95% of the whole electronics market, based on the CMOS and integrated circuit concepts, Si-based technology needs to drastically improve on short terms in order to delay the so-called "red brick wall" [1], projected to "ghost up" soon due the relentless aggressive scaling –the basic pillar in boosting performance– entering the (sub) nm range. Revolutionary redirectioning would imply, among others, the introduction of alternative materials, such as both low and high-κ insulators in replacement of the classic SiO_2. Without doubt, one element that would drastically add to stretch the all-Si dominance would be the ability to produce optically active parts based on Si and integrate them with the existing industrial production lines. It would enable to realize in an inherent way the unconditional optical branch in the integrated circuit technology with minimal impact on the current production lines, and hence, production costs.

Being able to tune the optical properties of silicon by controlling the size is a breakthrough achieved over the last two decades. Si nanoparticles (np's) have

emerged as a pursued solution, combining adequate mechanical strength (when embedded in oxides) with good optical properties, thus opening the route to achieve outstanding realizations such as Si lasers and quantum computers [2], with integration of optical components into the current Si-based semiconductor technology [3]. The Si np's are also introduced in complementary metal-oxide-semiconductor (CMOS) technology [4, 5], flash memories [6], and photovoltaic applications [7]. This makes the synthesis of Si np's of controlled size and particle/matrix interface quality of both fundamental and technological interest. Routinely, Si np's are embedded in SiO_2 as it enables realization of the high quality interface it naturally forms with Si.

But over the rollout of the Si-era, the silicon heterostructure based device development has been hampered by defects in all possible forms such as constituting charge traps when electrically active or decreasing mechanical or optical properties. With the current evolution, this keeps being true not less than ever before. The smaller the components grow, the larger the interface area-to-volume ratio, with a projected growing relative impact of interface defects as consequence. Point defects are blamed (some demonstrated, some hinted) for virtually all electrical and optical imperfections, so understanding how, why, and where they appear, and, as epitome, revealing their atomic nature, would provide us with a solid advantage in the fight for suppressing their presence or influence.

In the half century since its invention by Zavoiskii [8], ESR emerged as a noninvasive technique to provide detailed information on a variety of paramagnetic defects occurring in organic and inorganic, gaseous, liquid and solid systems. The multitude of systems to which the technique is applicable and the underlaying clear insight into its fundamental concepts based on quantum mechanics make ESR a most powerful fundamental research technique. It has proven to be very useful not only for physics but also for chemistry, biology, geology etc. When it comes to paramagnetic defects, ESR provides the keys. One of the most powerful features of ESR is that it can sense defects at an atomic level in a solid.

The aim of this thesis is to extensively investigate, using ESR, Si nanoparticles embedded in a-SiO_2 from sizes of $\sim$5 nm down to 4-5 Si atoms manufactured by different methods. Using unpaired electrons in the sample structure we can "see" the atomic surrounding and get an accurate picture of the crystallinity of the Si nanoparticles and the quality of the embedding matrix.

Chapter 1 includes a short overview of the main ESR principles and the features used to extract useful information within the context of the presented work. Point defects in a-SiO_2 known from previous ESR investigations and encountered in the structures presented in this thesis are briefly discussed next, emphasizing their salient parameters.

Chapter 2 presents an extensive ESR analysis (X, K, and Q-band spectrometers, combining two detection modes) on structures composed of Si nanoparticles (2 nm

across and larger) embedded in a-SiO_2 matrix obtained by annealing of SiO/SiO_2 superstructures. As one result, it will be shown that in fact the P_{b0} point defects at the nanocrystal (nc-)Si/SiO_2 interface, when paramagnetic, are responsible for quenching photoluminescence (PL).

Chapter 3 deals with the results of the ESR study on the influence of in situ ultrasound treatment (UST) during implantation at 300 K of Si^+ ions into thermal SiO_2 on (100)Si before and after subsequent high-T annealing (1100 °C) intended to promote formation of embedded Si nanoparticles.

While the previous chapters deal with Si nanoparticles embedded in a-SiO_2, in **Chap. 4** we will address a case of a *very small nanoparticle*, consisting of only 4-5 Si atoms that is, the E'_δ point defect, member of the particular class of intrinsic O-vacancy related point defects in a-SiO_2, an E' variant. Since its first observation in 1986, for this paramagnetic center no definitive model could yet be conceived by the scientific community. Using multi-frequency ESR measurements at different temperatures we are addressing the E'_δ spectrum in pertinent detail. A main aim is to assemble a meaningful statistical set of data on the relative intensity of the resolved ^{29}Si hf interaction to provide a solid ground for decisive E'_δ atomic modeling. The results point to a configuration of an unpaired electron delocalized at the place of a 4- or 5-Si mini-cluster.

So, all outlined chapters can be considered as dealing with the investigation of point defects that appear when Si nanoparticles are embedded in a-SiO_2, from a size of 4-5 nm down to 4-5 Si atoms.

The most important conclusions as well as ideas for future work related to the studied subjects are summarized in the final section.

Chapter 1

Electron spin resonance investigation of paramagnetic point defects

With decreasing size of electronic and optic components the relative influence of (interface) point defects on performance and reliability increases dramatically. The aim of this thesis is to assess, characterize, and identify the different point defects present and their influence on nc-Si/SiO_2 structures obtained by various techniques. Additionally, by means of an in-depth ESR study, we will also address the atomic nature of the E'_δ point defect occurring in O-deficient SiO_2 for which an atomic model is still elusive.

The most detailed atomic-scale models of point defects generally derive from probing them by ESR [9], of which the results can then be linked with other spectroscopic results obtained experimentally or theoretically. When it comes to atomic scale assessment of defects, ESR offers the ability to detect and register the unpaired electrons wave function interaction with the surrounding (other unpaired electrons and nuclei), thus giving not only a picture of the nearby atoms but also an indication of the crystal field pattern around the paramagnetic center.

Detailed information on the ESR principles and applications can be found in many books and review articles that extensively describe both theory and technique [10, 11, 12, 13]. In the next paragraphs, a brief description of ESR is given to provide the reader with working knowledge on how information has been extracted and interpreted within the framework of this thesis.

1.1 Electron Spin Resonance

Electron spin resonance is the study of spin transitions, generally, between two adjacent Zeeman levels resonantly induced by absorption of microwave photons of which the energy hν equals the difference between the two Zeeman levels. The Zeeman splitted electronic levels are the result of the interaction of the electronic magnetic moment with a magnetic field and the gap is equal to the energy needed to reorient the electronic magnetic moment $\overrightarrow{\mu}$ in the effective magnetic field $\overrightarrow{\mathrm{B}}$ (the sum of externally applied field B and the local field B_l) at the electron, along the classical interaction:

$$E = -\overrightarrow{\mu} \cdot \overrightarrow{\mathrm{B}}. \tag{1.1}$$

For a free electron with spin angular moment $\hbar\overrightarrow{S}$, where $2\pi\hbar$ is Planck's constant, we have:

$$\overrightarrow{\mu} = -g_e\beta_B\overrightarrow{S}, \tag{1.2}$$

where β_B is the Bohr magneton and g_e the spectroscopic splitting factor (commonly simply referred to as the g-factor) of the free electron. We note that the electronic magnetic moment is antiparallel with the angular moment. If taking into account both the spin angular momentum of the electron and the orbital angular momentum $\hbar\overrightarrow{L}$ due to its motion around the nucleus,

$$\overrightarrow{\mu} = -\mu_B(g_e\overrightarrow{S} + \overrightarrow{L}), \tag{1.3}$$

and, the quantum mechanical Zeeman Hamiltonian term is given as

$$\mathcal{H}_Z = \mu_B(g_e\overrightarrow{S} + \overrightarrow{L}) \cdot \overrightarrow{B}, \tag{1.4}$$

which can be rewritten as:

$$\mathcal{H}_Z = \mu_B g\overrightarrow{J} \cdot \overrightarrow{B} = \mu_B g J_z B, \tag{1.5}$$

where $-\mu_B g\overrightarrow{J}$ is the overall magnetic moment, μ_B the Bohr magneton, and g the effective (Landé) g factor. The total angular momentum $\overrightarrow{J} = \overrightarrow{S} + \overrightarrow{L}$ may take the values |L-S| , |L-S+1|, ... , |L+S-1|, |L+S|, where the lowest energy state is that with either the minimum (lower half of an unfilled shell) or maximum (upper half) J value. For the particular J, the magnetic quantum number m_J corresponding to J_z takes the values -J, -J+1,..., J, so the gap between each two consecutive energy levels is

$$\Delta E_Z = g\mu_B\mathrm{B}. \tag{1.6}$$

Under the selection rule $\Delta m_J = \pm 1$, as applying for inter level induced transitions by photon absorption, this gives rise to the resonance condition:

$$h\nu = g\mu_B\mathrm{B}. \tag{1.7}$$

In solids the electronic orbital motion interacts strongly with the crystalline (c-) electric fields and becomes decoupled (a phenomenon called 'quenching') from the spin so, the g value gets closer to the free electron value $g_e = 2.002319$ [10]. Generally, the interaction energy of a spin system in a magnetic field $\overrightarrow{B}$ includes, besides the Zeeman term, more interactions which may significantly depend on the actual spin system. It is more accurately described by the spin Hamiltonian, for which a simplified form is:

$$\mathcal{H}_{\mathrm{S}} = \mu_\beta \overrightarrow{B} \cdot \hat{g} \cdot \overrightarrow{S} + \overrightarrow{I} \cdot \hat{A} \cdot \overrightarrow{S} + \overrightarrow{S} \cdot \hat{D} \cdot \overrightarrow{S} + \mathcal{H}_{\mathrm{cf}} + ..., \tag{1.8}$$

thus respectively written as the sum of the Zeeman term, the hyperfine (hf) (for $\mathrm{I} \neq 0$) interaction, the spin-spin interaction ($\mathrm{S} > \frac{1}{2}$; fine structure or zero-field splitting term), and the crystal field energy. Here, I represents the nuclear spin and $\hat{g}$, $\hat{A}$, and $\hat{D}$ are the corresponding matrices (dyadics).

g values

With such overall complex interaction, the field symmetry is rarely spherical at the unpaired electron, resulting in the fact that g value has to be replaced by a matrix $\hat{g}$, which, however, is always diagonalizable along the principal axes (x, y and z). In an orthorhombic system, the principal values are sometimes renamed as $g_1 \geq g_2 \geq g_3$. In the case of axial symmetry, z is conventionally taken as the symmetry axis, thus:

$$\begin{aligned} g_\parallel &= g_z \\ g_\perp &= g_x = g_y. \end{aligned} \tag{1.9}$$

Using the principal g values and θ_i, the angle that the principal axis i ($\mathrm{i} = x, y, z$) makes with the magnetic field direction, the effective g value g_c can be written as:

$$g_c = \sqrt{g_x^2 \cos^2\theta_x + g_y^2 \cos^2\theta_y + g_z^2 \cos^2\theta_z}. \tag{1.10}$$

In an axial symmetric case, the equation can be simplified as:

$$g_c = \sqrt{g_\parallel^2 \sin^2\theta + g_\perp^2 \cos^2\theta}. \tag{1.11}$$

A crystalline surrounding is allowing only specific orientations of a defect structure, and hence, also of the associated unpaired electron wave function, producing angle dependant signals (g_c), one for each allowed defect orientation, as in the case of, e.g., P_b-type point defects at the Si/SiO_2 interface. In an amorphous or polycrystalline system, defects, and hence the unpaired electron wave functions are randomly oriented and the spectral properties are averaged over all possible orientations of the defect, giving rise to an angle independent *powder pattern*.

1.1.1 Hyperfine interaction

The *hyperfine coupling constant* A is a measure of the electron hf interaction with the surrounding nuclei with a nuclear spin I $\neq$ 0, resulting, for interaction with one nuclear site, in a splitting of the main resonance line into (2I+1) ESR signals. The hf interaction is generally anisotropic and the hf interaction matrix $\hat{A}$ can be written as

$$\hat{A} = A_{iso}\hat{1} + \hat{T}, \tag{1.12}$$

that is, the sum of the isotropic hf interaction matrix $A_{iso}\hat{1}$ and of the anisotropic hf interaction matrix $\hat{T}$. The first term corresponds to the isotropic Fermi-contact interaction and the second one to the anisotropic electron nuclear dipole-dipole coupling. The Fermi-contact Hamiltonian $\mathcal{H}_{\mathrm{f}}$ can be written as

$$\mathcal{H}_{\mathrm{f}} = A_{iso}\,\overrightarrow{S}\cdot\overrightarrow{I}, \tag{1.13}$$

where

$$A_{iso} = \frac{2}{3}\mu_0 g_e \beta_B g_N \beta_N |\Psi_0(0)|^2, \tag{1.14}$$

and where μ_0 represents the permeability of free space, β_N the nuclear magneton, g_N the nuclear g factor, and $\Psi_0(0)$ the ground state electron wave function at the interacting nucleus. From Eq. 1.13 it is evident that the measurement of the isotropic hf interaction may result in the determination of the probability density of the electron at the site of the interactive nucleus of the chemical identity if the nucleus is known. Obviously, there is only an A_{iso} contribution for the s-state wave function of the magnetic nucleus.

The electron nuclear dipole-dipole coupling Hamiltonian $\mathcal{H}_{\mathrm{dd}}$ can be written as

$$\mathcal{H}_{\mathrm{dd}} = \frac{\mu_0}{4\pi} g_e \beta_B g_N \beta_N \left[\frac{(3\overrightarrow{S}\cdot\overrightarrow{r})(\overrightarrow{r}\cdot\overrightarrow{I})}{r^5} - \frac{\overrightarrow{S}\cdot\overrightarrow{I}}{r^3}\right] = \overrightarrow{S}\cdot\hat{T}\cdot\overrightarrow{I}, \tag{1.15}$$

where $\overrightarrow{r}$ is the average distance vector between the electron and the nucleus.

For most of the hf structure of point defects confronted within the current thesis, in fact with what concerns the ESR work on the basic semiconductors in general, the unpaired electron wave function can, to a good approximation, be considered as a *sp*-hybrid, i.e., composed of s and p orbitals only. It applies to the analysis of defects in solids with conduction and top valence bands made up by sp^3 hybrid orbitals. Then, in the LCAO (linear combination of atomic orbitals) approximation the ground state wave function of the unpaired electron orbital can be written as

$$\Psi_0(\overrightarrow{r}) = \sum_i \eta_i \Psi_i(\overrightarrow{r}) = \sum_i \eta_i [\alpha_i(\Psi_{s,i}(\overrightarrow{r})) + \beta_i(\Psi_{p,i}(\overrightarrow{r}))], \tag{1.16}$$

where $\Psi_i(\overrightarrow{r})$ are sp-type hybrids at nuclear sites i composed of the atomic s-state $\Psi_{s,i}(\overrightarrow{r})$ and p-state $\Psi_{p,i}(\overrightarrow{r})$ orbitals, and where normalization requires $\sum_i \eta_i^2 = 1$ and $\forall i$, $\alpha_i^2 + \beta_i^2 = 1$; the sum $\sum_i$ runs over all (identical) nuclear sites where the wave function has an appreciable density. Here, η_i^2 is the wave function density at the i-th nuclear site, and α_i^2 and β_i^2 represent its s and p character, respectively.

The restriction to s and p type orbitals implies that the hf matrix $\hat{A}$ is majorly axially symmetric. In general, principal values of $\hat{A}$ can be written in terms of an isotropic (A_{iso}) part (s part: Fermi contact interaction), an anisotropic (b) part (p part: dipolar interaction), and an orthorhombic (c) part (deviation from perfect sp character:

$$A_1 = A_{iso} + 2b \tag{1.17}$$

$$A_2 = A_{iso} - b + c \tag{1.18}$$

$$A_3 = A_{iso} - b - c. \tag{1.19}$$

Within the assumption of a perfect sp^3 hybridization (c = 0), the combination of Eqs. 1.8, 1.13, 1.15, and 1.16 renders:

$$| < \Psi_{s,i} | \Psi_0 > |^2 = \eta_i^2 \alpha_i^2 = \frac{A_{iso,i}}{A_s} \tag{1.20}$$

$$| < \Psi_{p,i} | \Psi_0 > |^2 = \eta_i^2 \beta_i^2 = \frac{b_i}{A_p} \tag{1.21}$$

$$1 = \alpha_i^2 + \beta_i^2, \tag{1.22}$$

where A_s and A_p are, respectively, the atomic s and p-state hf coupling constants, inferred from theory. Thus the LCAO analysis of the hf interaction presents a simple method to investigate the localization (η_i^2) of the electron wave function on an atom i and extract the s (α_i^2) and p (β_i^2) character of the orbital composition of the unpaired electron.

For axial symmetry, the relationship between the principal values of hf coupling constants and the measured values $A_\parallel$ and $A_\perp$ is given as

$$A_{iso} = \frac{A_\parallel + 2A_\perp}{3} \tag{1.23}$$

$$A_{aniso} = \frac{A_\parallel - A_\perp}{3}, \tag{1.24}$$

Table 1.1: The values of R_{hf}, the ratio of the hf structure intensity to that of the main resonance line, calculated using Eq. 1.25. Here, P_{29} represents the probability for the occurrence of only one ^{29}Si ($\eta = 4.67$ %) over the n possible sites, while P_{28} is the probability for none. R^*_{hf} is the exact value of the ratio for all the combinations of the two isotopes.

n	P_{29}	P_{28}	R_{hf}	R^*_{hf}
1	0.047	0.953	0.049	0.049
2	0.089	0.908	0.098	0.098
3	0.127	0.866	0.147	0.147
4	0.162	0.825	0.196	0.195
5	0.193	0.786	0.245	0.243
6	0.221	0.749	0.294	0.290

where A_{aniso} is a measure of the hf coupling anisotropy. When expressed in magnetic field units, it is conventional to use the symbols $a_{\rm iso}$ and $a_{\rm aniso}$, now referred to as *hf splitting constants*.

The ratio $R_{hf}(\eta,$ n) of the intensity (area under absorption curve) $\mathcal{I}_{hf}$ of a hf multiplet to that of the central main (Zeeman) signal $\mathcal{I}_c$, is reflecting the distribution of the unpaired electron wave function (spin density) over the defect's constituent atoms –*not always paid sufficient attention to when the ESR sensitivity is limited*. This ratio is a function of η, the (natural) abundance of the hf-originating nuclear isotope, and n, the number of such atoms in a shell of equivalent sites with which the unpaired spin is interacting. With η known, inferring n provides a basic clue to convincing atomic modeling.

The correct determination of $R_{hf}(\eta,$ n) for small η values is given to a good approximation by the expression

$$R_{hf} = \frac{\mathcal{I}_{hf}}{\mathcal{I}_c} = \frac{\eta n(1-\eta)^{n-1}}{(1-\eta)^n} = \frac{\eta n}{1-\eta}, \tag{1.25}$$

which is restricted to the occurrence of only one $I \neq 0$ isotope in a shell. Values of the intensity ratio R_{hf} calculated along Eq. 1.25 for the interaction with n Si atoms are listed in Table 1.1. P_{29} represents the probability for finding one ^{29}Si isotope in a shell, while P_{28} is the probability of all atoms being ^{28}Si ($I = 0$) nuclei.The value R^*_{hf} is calculated taking into account all the possible combinations of ^{28}Si and ^{29}Si isotopes in a cluster of n Si atoms. A difference between the former and the latter values is observed only for higher n values, reaching 0.4 % for $n = 6$. Thus, we can safely use in further work the easier to calculate R_{hf} value.

1.1.2 ESR detection modes

ESR signals are measured as the microwave power P_μ absorbed by the sample at resonance. As it is often the case (point defects are often present in a low density $\sim 10^{12}$ per sample), utmost sensitivity is required from the ESR, mandating an optimized design. The "bridge" method [13] consists in placing the sample in a resonance cavity to enhance, using the high quality factor Q of the cavity (even $\gtrsim$10000), the microwave field amplitude B_μ at the sample site. The detected absorption measures χ'' (imaginary part of the complex susceptibility) induced by the resonance.

In a classical way, the magnetic resonance phenomenon can be very convincingly described by the phenomenological Bloch equations. As solved, these are are only valid in the stationary state, i.e., thermal equilibrium, so, to avoid or minimize "passage" effects, the external field must be slowly varied as to allow the continuous adaptation of the energy levels system (quasi-stationary). For narrow lines (long spin-lattice relaxation time T_1) the passage has to be slow enough and the power sufficiently low not to saturate and, correlated herewith, deform the signals, thus hampering sensitivity. As commonly used, sensitivity can be drastically enhanced by applying the lock-in technique. So here, instead of χ''(B) we measure its first derivative $\frac{d\chi''(B)}{dB}$. This is performed by superimposing on the static magnetic field $\overrightarrow{B}$ a small field, $\overrightarrow{B}_m = \overrightarrow{e}_B B_m cos\omega_m t$, oscillating along the same axis, referred to as modulation field. The amplitude of the modulation field has to be adapted to the broadness of the signal and the frequency is usually taken to be around 100 kHz not to affect the slow passage condition.

The ESR spectrometer sensitivity is influenced by many factors, including the microwave power, detection system and the spectrometer band (observational frequency), the unpaired electron system in the sample and the loaded cavity sample response. A typical detection limit is $<1 \times 10^{11}$ spins per sample, but this level depends very much on the saturability, the width of the signal, and observational temperature.

In the case of highly saturable centers, appropriately decreasing P_μ is decreasing the sensitivity and in some cases (e.g., the Bruker Q-band set up described later in this chapter) even the spectrometer stabilization cannot handle the required low power level. While not yet fully theoretically understood, empirical evidence [14, 15] indicates that the second harmonic out of phase detection mode [16] allows for higher values for B_m and P_μ, while showing the *absorption* shapes of the saturated signals and the second harmonic of the unsaturated ones (e.g. the markers). The shape and peak position of the high power second harmonic out of phase signals correspond to the absorption spectra and g_c values of the correctly measured dP_μ/dB ones, respectively, and thus can be used for signal attribution and identification purposes. Yet it cannot be used for reliable intensity calibration

[14, 15]. For the same spectrometer parameter settings, some signals saturate more than others, even in the same sample, resulting in different amplitudes of their corresponding second harmonic spectra, one reason for which the intensity of a saturated signal can never be trusted in inferring accurate densities. However, centers pertaining to the same family show similar saturation behavior [17] and a relative comparison can sometimes be made, but one has to be careful.

1.1.3 Spectrometers

Four ESR spectrometers were used to measure the different samples in the studies presented in the next chapters. The most used one is a K-band ($\nu \sim 20.5$ GHz) spectrometer built in this laboratory with very high sensitivity especially at low temperatures and it can also operate at very low microwave power (even $\sim 10^{-12}$ W) enabling a correct detection of weak and/or very saturable signals. It is equipped with a liquid He bath cryostat, allowing sample temperatures between 1 and 300 K, but it is used usually for measurements at 4.2 K. The same construction can be also equipped with a home-made X-band ($\nu \sim 8.9$ GHz) modulus. The other two spectrometers, a commercial Bruker EMX Q-band ($\nu \sim 33.9$ GHz) and a Jeol JES-FA 100 X-band, are equipped with a liquid He and N_2 flow cryostat, respectively, allowing a good temperature control down to ∼10 K for the first and ∼200 K for the latter. The Jeol X-band was mostly used at room temperature (RT).

Each of the four systems is equipped with a cylindrical TE_{011} microwave reflection cavity, routinely driven in the absorption mode under conditions of slow adiabatic passage. All the four spectrometers were used in the low power first harmonic as well as in the second harmonic out-of-phase detection mode. The modulation amplitude was chosen not to distort the narrowest signal in a spectrum but also to obtain good signal-to-noise ratio. Other parameters that influence the quality of the measured signals are the time constant of the lock-in detector, the analog-digital conversion time, number of data points (usually 1024), all affecting especially narrow lines, and the receiver gain which affects only the absolute amplitude of the signals. The spectrometers averaging capabilities are extensively used to improve the signal-to-noise ratio. While typically 100-200 scans were usually sufficient, in the case of the very low density signals like the E'_δ hf discussed in Chap. 4 up to 10000 scans were added to obtain a good spectrum.

The main difference the spectrometer band is bringing is that the g-spread induced line broadening is smaller for low microwave frequency than for higher frequency (e.g., in Q-band it is enlarged by $\sim 3.6\times$ compared to X-band), as it comes out of the resonance condition in Eq. (1.7). The splitting of the hf signals, however, remains constant since it is not influenced by the externally applied magnetic field to first order. Thus, using at least 2 different observational frequencies (bands) is

enhancing deconvolution chances as well as the reliability of inferred parameters through simulation.

1.1.4 Signal lineshapes

Besides its magnetic field position (g_c) and hf splitting, an ESR first derivative absorption signal (dP_μ/dB) is characterized by its peak-to-peak width ΔB_{pp} and lineshape, which, when correctly interpreted, can offer useful information about the local atomic field distribution and intensity. The common lineshapes in the study of point defects are Gaussian, Lorentzian and Voigt, a convolution of Lorentzian and Gaussian profiles, resulting in an intermediate shape between the first two. The kind of dominant broadening (or narrowing) mechanism of the unsaturated undistorted ESR signals gives rise to one of the above lineshapes, also influencing the line width ΔB_{pp}. The spin-lattice relaxation time is primarily influencing the signal intrinsic broadening because of the Heisenberg-type relationship it has with energy ($\Delta E \cdot \Delta t \geq \frac{\hbar}{2}$). Thus a short relaxation time leads to a "smearing out" of energy involved, transposed in a broader intrinsic ESR line width.

When the magnetic field differs slightly from defect site to site, only a small fraction of centers is simultaneously in resonance for a particular field value as the external magnetic field is swept, giving rise to a superposition of individual components slightly shifted, producing a Gaussian lineshape. Main origins for such inhomogeneity include anisotropic interactions in solid, among randomly oriented systems and unresolved hf structure, or even undesired inhomogeneity of the external magnetic field (large samples).

In the case of an homogenous broadening, the instantaneous magnetic field is homogenous over the whole spin system but changes from one moment of time to the other (static and time averaged fields are uniform for all spins), resulting in a signal of Lorentzian lineshape. This broadening mechanism is determined by the spin-spin interaction, occurring in all but most dilute samples.

1.1.5 Signal intensity

The intensity (area under absorption curve) of the ESR signal $\mathcal{I} \sim \chi$, which enables direct determination of the number of unpaired spins (defects) N_s in the sample spin system present. It is a highly esteemed capability, with much diagnostic value, of the conventional ESR technique. Yet, as is the case in general for any ESR signal measurement, the response appearance may be affected by many spectrometer parameters and settings. If not handled correctly, some may, often inadvertently, distort signals in an unacceptable way. So, as discussed below, one has to be very cautious when aiming correct determination of defect densities. As amply demonstrated, there is no doubt that the method of co-mounted reference sample is

the method of choice, leading to the most accurate and reliable results. Then, many of the variables affecting signal intensity cancel. In this approach, a (usually small) marker sample is mounted together with, usually next to, the studied sample in the cavity, and its number of spins N_{ref} is used as reference to calculate the density of the sample spin system. It gives accurate numbers (unlike using absolute signal intensity), allowing one to neglect the influence of parameters like Q or absolute value of incident P_{μ} –both samples, if mounted together, are affected in the same way. It is the method customarily applied in this work.

Under conditions of no significant saturation and overmodulation, the number of spins(defects) N_s is then given by

$$N_s = \frac{\mathcal{I}_s}{\mathcal{I}_{ref}} \cdot \mathrm{N}_{ref} \cdot \frac{\mathrm{g}_{ref}^2}{\mathrm{g}_s^2} \cdot \frac{\mathrm{S}_{ref}(\mathrm{S}_{ref}+1)}{\mathrm{S}_s(\mathrm{S}_s+1)} \cdot \frac{< \mathrm{B}_{\mu}^2 >_{ref}}{< \mathrm{B}_{\mu}^2 >_s} \cdot \frac{\mathrm{T} - (\mathrm{T}_C)_s}{\mathrm{T} - (\mathrm{T}_C)_{ref}} \cdot f, \tag{1.26}$$

where $< B_{\mu}^2 >$ is the sample (marker) averaged value of the square of the applied microwave magnetic field amplitude and the factor containing T accounts for (possible unequal) temperature dependances of the spin systems involved, here both supposed to exhibit Currie-Weiss paramagnetism. The intensities are obtained usually by integration of fitted computer simulations of each signal, but also direct integration of the measured lines is usable in the absence of signal overlapping. The absolute number of spins N_{ref} producing the reference signal has to be *independently* obtained. The factor f becomes 1 when both the unknown and reference signals are measured in the same scan, otherwise, when the signals compared are obtained from different scans (spectra) it has to be calculated as:

$$f = \frac{(\delta \mathrm{B}_s)^2}{(\delta \mathrm{B}_{ref})^2} \cdot \frac{(\mathrm{P}_{\mu})_{ref}^2}{(\mathrm{P}_{\mu})_s^2} \frac{(B_m)_{ref}}{(B_m)_s} \frac{G_{ref}}{G_s}. \tag{1.27}$$

Here δB indicates the sweep width of the spectrum from which the corresponding signal intensity is calculated and G is the used receiver gain. Unless the division of the output spectrum by the number of scans is done in the spectrometer program itself, as the Jeol spectrometer does, but instead, it just adds the different scans, the intensity of each signal has to be normalized by the corresponding number of scans performed before using Eq. (1.26). For the intensity comparison to be reliable when the two signals are not registered in the same sweep, it is important to emphasize that both the sample and marker signals have to be measured closely in time, one after the other, thus minimizing the quality factor changes.

Finally, proper corrections have to be included regarding the position of the unknown and marker sample relative to each other and relative to their positioning

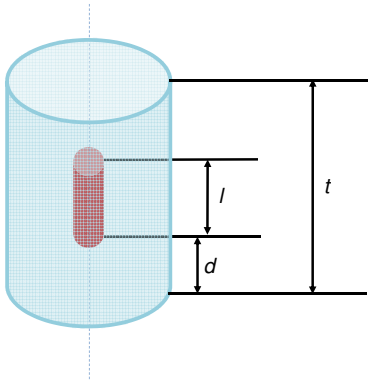

Figure 1.1: The relative position of the studied sample (red) in the cylindrical TE_{011} microwave cavity (blue) with characteristic lengths indicated.

in the cavity (the marker is almost always point like). It may be termed the shape-position correction factor, which is very important to take into account. It stems from the fact that the power absorption, and hence ESR signal intensity, is proportional to the square of the actual microwave magnetic field component (B_μ) at each point:

$$\mathcal{I} \propto \chi'' \propto B_\mu^2. \tag{1.28}$$

In Fig. 1.1 a cylindrical TE_{011} is sketched and the position and characteristic lengths of the studied sample (l) and cavity (t) are indicated. Using those notations, the correction factor to be taken into account is given as

$$\mathcal{I} \propto \frac{2\pi\frac{l}{t} - \sin\left(2\pi\frac{d+l}{t}\right) + \sin\left(2\pi\frac{d}{t}\right)}{4\pi\frac{l}{t}}. \tag{1.29}$$

All of the above corrections have to be taken into account for a correct evaluation of the number of ESR centers.

1.1.6 Markers

To be suitable as a marker, a sample has to show a narrow signal in an appropriate part of the spectrum not to interfere with the sample signals, it has to be out of

saturation even at high powers –so, high level of nonsaturability–, it has to have have a small volume –so it does not reduce the effectively available sample space–, and all the ESR signal salient parameters and density have to be well known, to good accuracy, from independent measurements. The markers are also used, besides density calibration, for an accurate g value calibration when the microwave frequency or the static magnetic field at the sample site can not be read correctly by the equipment. For the research performed in this work, four types of markers have been used:

- Si:P marker [18]: S=1/2, g(4.2K) = 1.99869 ± 0.00002, g(30K) = 1.99876 ± 0.00002 and g(RT) = 1.9982 ± 0.00005, $\Delta B_{pp} < 1$ G (1.25 K < T < 45 K). The signal pertains to a high density of implanted P atoms in c-Si, affected by exchange narrowing, and having a Currie-Weiss behavior ($\chi \sim \frac{1}{T-T_C}$) with T_C = - 2.7 ± 0.3 K. The signal is stable in time, but broadens and changes g_c value with changing temperature, limiting its usability to low-T (T < 100K) studies.

- Li:F marker [19]: S=1/2, g = 2.00229 ± 0.00002, constant g_c and ΔB_{pp} values over a large T interval ($4.2 \leq T \leq 300$K), but the lineshape changes from a single Lorentzian at RT to a sum of two Lorentzians of identical g but different widths ($\Delta B_{pp} = 0.65$ G, $\Delta B_{pp} = 2.18$ G) at low temperature. The signal arises from conduction electrons in Li nanoparticles produced by neutron irradiation of LiF. The number of spins is T-independent, showing a Pauli paramagnetic behavior.

- DPPH (2,2-diphenyl-1-picrylhydrazyl) marker [20, 21]: S=1/2, g = 2.00357 ± 0.00005, T_C = 20 - 36 K (see e.g., [22] and references therein). It was used as a RT marker. The Lorentzian-like line appearing in solid DPPH is due to exchange narrowing and the width varies depending on the solvent from which it was precipitated. For the DPPH used here broader wings than Lorentzian were observed, which can be simulated by two overlapping Lorentzians of equal g_c values but with different widths ($\Delta B_{pp} = 2.8$ and $\Delta B_{pp} = 4.9$ G). Unfortunately, the corresponding signal intensity decays in time (∼ days) but slow enough to be used as a reference for a few hours, so a calibration against Li:F at RT is made right before and/or right after its usage as a marker for calibrating an unknown signal. Furthermore, one has to be careful when using DPPH as reference because it also saturates, but only at high power levels ($\gtrsim$1.6 μW in the Bruker Q-band). This marker was only used in the research related to the E'_δ point defect, since Si:P partly overlaps the signals and broadens too much at RT, while Li:F marker is too close to the signal of interest (E'_δ), partly overlapping it.

- The MgO:Mn^{2+} marker (S=5/2; η = 100 ^{55}Mn % natural abundance I=5/2) was supplied together with the Jeol X-band spectrometer in the shape of a small rod that can be electromechanically inserted from outside into the

microwave cavity. The Mn^{2+} in MgO matrix gives a spectrum of 6 sharp hf lines (Lorentzians in X-band measurements) separated by ∼85 G [9]. For sensitivity reasons, in spectra taken for density calculations, we only include the closest line of the Mn^{2+} to the signal of interest or, at maximum, the two closest ones (usually the 3^{rd} and 4^{th} line). In practice, we considered the lines as independent but of equal intensity and performed the density calibration individually against the Li:F marker at RT. At X-band, the g values of the third and forth lines of the Mn^{2+} sextet were calibrated as 2.0338 ± 0.0001 and 1.9807 ± 0.0001, respectively. The electromechanical positioning (sliding) system of the marker provided by the manufacturer does not guarantee perfect reproduction in the absolute position of the MgO:Mn rod in the cavity for the same software application parameters. Thus, the density calibration of the Mn^{2+} line/lines has to be performed each time before and/or after each individual measurement session (during a session the rod should not be moved).

1.2 Paramagnetic point defects in SiO_2 and Si/SiO_2 entities

In the present study, we are, among others, involved with sensing by ESR nc-Si particles embedded in different oxides, mainly a-SiO_2. An important problem for technology are defects in the various, ever smaller and smaller structures. The main types of defects encountered are both interface and bulk defects, some intrinsic, some extrinsic related to impurities, and many occur inherently, or are generated by implantation or irradiation. The main ESR parameters of known defects are summarized in Table 1.2.

1.2.1 Si/SiO_2 interface paramagnetic defects

Conventionally, a-SiO_2 is thermally grown on Si by heating the substrates in O_2 ambient at high temperatures (800-960 °C), resulting in a low defect density Si/SiO_2 system (where interface defects can additionally be efficiently passivated by H –diffusion length of H^0 and H_2 in a-SiO_2 at RT is ≈ 200000 and 2500 nm, respectively [52]) with a stable interface. The oxide has a large bandgap ∼9 eV, being a very good insulator. The interfaces of c-Si/a-SiO_2 have been extensively studied by ESR for different, mainly (111) and (100), orientations of the crystalline Si interface planes. But these ESR studies have almost exclusively been performed on macroscopic Si/SiO_2 entities of extended interface area (∼1 cm^2). So, what happens for interfaces extending over only a few nm^2? Some answers will be given

Table 1.2: The summary of ESR active point defects discussed in this chapter. All those paramagnetic centers were observed at various occasions during the research work presented in this thesis.

Material	Defect	g_1	g_2	g_3	a_{iso} (G)	a_{aniso} (G)	References
a-Si	D	2.008	2.008	2.004	73 ± 3	18 ± 3	[23, 24]
			$g_c = 2.0055$				
(111)Si/SiO_2	P_b	2.0086	2.0086	2.0013	112 ± 6	22 ± 4	[25, 26, 27]
(100)Si/SiO_2	P_{b0}	2.0081	2.0081	2.00185	99 ± 4	24 ± 3	[28, 29, 30]
	P_{b1}	2.00735	2.00577	2.0022	127 ± 3	20 ± 4	[28, 31, 30]
(110)Si/SiO_2	P_b	2.0081	2.0075	2.0016			[32]
SiO_x	S		$g_c = 2.0027$		279 ± 12	-	[33, 34, 35, 36]
					162 ± 5	-	[37, 35]
a-SiO_2	E'_s	2.0018	2.0000	2.0000	420 ± 3	-	[38]
	E'_γ	2.0018	2.0006	2.0003	420 ± 3	22 ± 4	[39, 40]
	E'_α	2.0017	2.0013	1.9998	455 ± 3	20 ± 3	[39], Chap. 4
	E'_β	2.0018	2.0004	2.0004	420	-	[39]
	E'_δ	2.0019	2.0021	2.0021	100 ± 2	-	[41], Chap. 4
	$[AlO_4]^0$	2.06000	2.00854	2.00195	8.4	-	[42, 43, 44, 45]
	[a]Al E'	2.0025	2.0004	2.0004	419	17	[46, 47]
N-related	K	2.0027	2.0033	2.0033	364	16.6	[48, 48]
	N	2.0035	2.0078	2.0078	11	12.5	[49]
C-related	C		$g_c \approx 2.003$				[50, 51]

[a] with nearby Na^+ charge compensator

later in this thesis, but first, let's introduce the systems of known ESR-active interface point defects in Si/SiO_2 structures, and summarize their properties.

In a nutshell, the different types of Si DB-type defects observed, invariably introduced at the c-Si/SiO_2 interface as a result of lattice mismatch [27, 53, 54, 55], correlate with interface orientation, in registry with the crystallinity of the underlying Si substrate. In ESR terminology, those paramagnetic centers are called P_b-type point defects. All the P_b-type defects presented next are encountered some way or the other at the nanocrystralline-Si/SiO_2 interfaces discussed in Chapters 2 and 3 of this thesis.

(111)Si/SiO_2 interface

At the (111)Si/SiO_2 interface, only one point defect type was observed —specifically termed P_b— and identified as trivalent interfacial Si ($Si_3 \equiv Si^\bullet$, where the dot represents an unpaired electron in a dangling Si sp^3 hybrid) backbonded to three Si atoms in the bulk as illustrated in Fig. 1.2. Poindexter and Caplan [25, 26] investigated the $\hat{g}$ matrix of the P_b signal as having axial symmetry with $g_\parallel$ along the [111] crystalline direction and the principal values presented in Table 1.2. Since the dangling bonds at the (111) interface have the same orientation, perpendicular to the plane, only one P_b center signal for each value of φ_B angle is observed. The other orientations along $[\bar{1}11]$, $[1\bar{1}1]$, and $[11\bar{1}]$ directions are unlikely to appear for a standard relatively smooth interface, thus the signals corresponding to those branches are also unlikely. Yet, in confirmation of the P_b atomic model, these defect directions have been observed in 'poorly' oxidized Si, that is, grown at ∼965 °C in a low oxygen pressure ($P_{ox} < 8 \times 10^{-5}$ Torr) [56]. The P_b center exhibits a hyperfine doublet with $a_{\rm iso} \approx 112$ G [27] as a result of the unpaired electron interaction with the ^{29}Si nucleus on which it is localized.

The P_b center (as well as the other P_b-type centers) can be passivated [57, 58, 59] by bonding to H atoms starting from $T_{\rm an} \gtrsim 225$ °C onward (in H_2 ambient), becoming diamagnetic, thus ESR invisible. The process is reversed [25, 26, 57, 60] under vacuum anneal (pressure $P \leq 10^{-4}$ at $T_{\rm an} \gtrsim 550$ °C), by dissociation of the bonded H atom. This passivation/depassivation mechanism is fully reversible both in atomic structure and number of point defects [53, 61, 62]. It has to be kept in mind that both passivation and depassivation are occurring simultaneously but at different rates depending on the ambient type, pressure, temperature and time of the annealing [62, 63, 64]. The natural density for standard (111)Si/SiO_2 interface is $[P_b] \sim 5 \times 10^{12}$ cm^{-2} (Refs. [28, 31, 53, 65]).

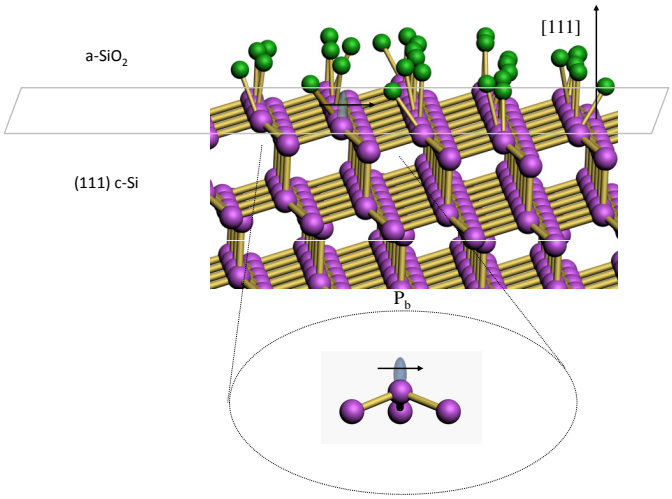

Figure 1.2: Ball-and-stick structure of the (111)Si/a-SiO_2 interface at the atomic level, where the P_b point defect is magnified.

(100)Si/SiO_2 interface

At the (100)Si/SiO_2 interface two types of point defects appear to ESR, termed P_{b0} and P_{b1}. The experimental evidence (identical lattice orientation of the principal axes, the near equal g principal values and similar hf coupling constants) is that P_{b0} is chemically identical to P_b, but now residing at microscopical (111)-oriented Si/SiO_2 facets (interface) (see Fig. 1.3, with the salient parameters shown in Table 1.2). The P_{b1} center is assigned to a distorted defected interfacial Si-Si dimer (Si_3 ≡Si–$Si^{\bullet}$= Si_2 defect, where the endash symbolizes a strained bond, with the unpaired Si sp^3 hybrid oriented $3^\circ \pm 1^\circ$ off the <211> direction), as pictured in Fig. 1.3, [30, 66] the model explaining also the orthorhombic $\hat{g}$ matrix (see Table 1.2). Thus both variants, like P_b, were shown to be interfacial trivalent Si centers, naturally occurring, for standard oxidation temperatures (800-960 °C) in areal densities of $[P_{b0}]$, $[P_{b1}] \sim 1 \times 10^{12}$ cm^{-2} [28, 31]. It is the low natural defect density (interface charge trapping center) and the higher electron mobility [67] that influenced the decision of using (100)Si substrates for electronic applications. But the (100)Si/SiO_2 interface shows low hole mobility [67], traditionally compensated by a larger p-MOSFET size to balance against the n-MOSFET, which creates other problems like increasing the gate and parasitic capacitances [68].

Combination of electrical measurements with ESR probing has established the

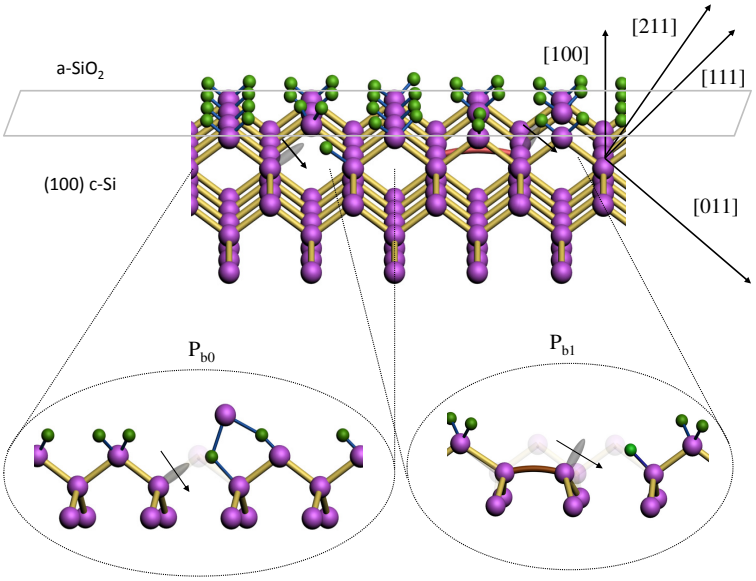

Figure 1.3: Schematic structure of (100)Si/SiO_2 interface at atomic level, where the occurring P_{b0} and P_{b1} point defects are shown enlarged in the bottom part.

$P_b(P_{b0})$ centers as major systems of detrimental electrically active interface traps [31, 69]. The electrical activity of P_{b1}, initially accepted, is still in dispute [31, 70, 71].

(110)Si/SiO_2 interface

The research on vertical transistors [72, 73, 74, 75] indicates that important electrical parameters depend strongly on the shape and orientation of the trench sidewall and raised the need to investigate properties of other interfaces than the classical (100)Si/SiO_2. The (110)Si/SiO_2 interface orientation has a higher mobility than the two interfaces discussed before in the case of PMOS, but lower for NMOS [76]. The facets naturally occurring at the nc-Si/SiO_2 interface can have different crystalline orientations, even (110)Si.

At the (110)Si/SiO_2 interface also, only one P_b-type center, a P_b0 variant [32, 54], is observed having almost axial symmetry (see Table 1.2), but it was not as extensively investigated by ESR as the other variants at the (100) and (111)Si/SiO_2 interfaces. At this interfacial plane there are two possible orientations of the unpaired electron

orbital [69] (cf. Fig. 1.4). Thus, two angle dependant signals can be observed by ESR in any plane where the sample is rotated in relative to the magnetic field. The signals overlap only when the φ_B angles for all dangling bond orientations are equal, that is, for $\overrightarrow{B}$ ∥[110], the interface normal, or $\overrightarrow{B}$ ∥[001].

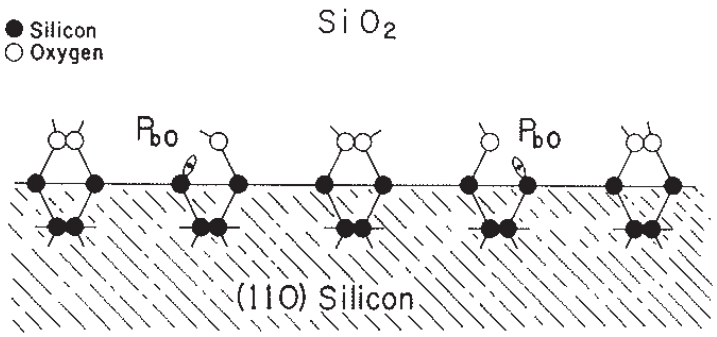

Figure 1.4: Schematic of the (110)Si/SiO_2 interface at the atomic level, illustrating the P_b point defects.

1.2.2 a-Si point defects

D center

While pure lone standing amorphous Si is not so much used, it is widely incorporated in the polycrystalline (usually hydrogenated) state in solar cells and flat panel displays [77]. From the ESR point of view, the amorphous and polycrystalline states appear quite similar, both containing randomly oriented unpaired electrons localized on Si atoms, named D centers, giving rise to an isotropic Lorentzian signal with ΔB_{pp} = 4-8 G [23, 24] and $g_c \sim 2.0055$ [78], depending on the preparation method [23, 79]. The D centers were mostly studied in hydrogenated a-Si, where the interference of H with the Si DB appears negligible [80], so the point defect has the same characteristics as in the nonhydrogenated a-Si. When looked at more carefully the signal can be simulated by a powder pattern with the g values listed

in Table 1.2 convoluted by a Gaussian function [24]. This simulation is useful to prove that also this defect concerns a Si dangling bond P_b-type center [81], but randomly oriented ($Si_3 \equiv Si^{\bullet}$ as shown in Fig. 1.5). Practically an isotropic Lorentzian function can be used as well; it is faster and gives the same values for defect densities.

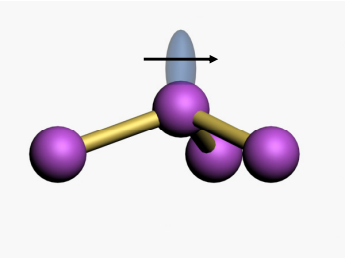

Figure 1.5: The basic atomic structure of the P_b -type point defect, which in an amorphous Si surrounding is called a D center —an unpaired electron localized in an sp^3 hybrid on a Si atom backbonded to three Si.

1.2.3 a-SiO_2 point defects

The E'-type centers are the most prominent class of point defects encountered in irradiated c- and a-SiO_2, essentially pictured as the class of single oxygen vacancy centers. It is composed of defects, where the unpaired electron is localized on a single or multiple Si atoms backbonded to oxygen atoms in the SiO_2 matrix. All the E' paramagnetic centers have one $\hat{g}$ principal value in the vicinity of 2.0018. Numerical subscripts are used to distinguish between the different E' centers in c-SiO_2: E'_1 [82], E'_2 [83], and E'_4 [84], while Greek letters are used for a-SiO_2, : E'_α, E'_β, E'_γ, and E'_δ.

The optical activity of a-SiO_2 is important since the material is broadly used for optical applications and there are possibilities for future integration with Si in all-Si based electronics. This brings this material back under attention in the scientific world. Skuja [85] presented an extensive overview of the optically active O-deficient centers in a-SiO_2 and concluded that E'_α, E'_β and E'_γ centers are active in the energy interval 5.7-5.8 eV, while E'_s at 6.0-6.3 eV energies. Until now, there seem to be no reports of E'_δ or EX being optically active, but, the possibility of these being so cannot be overlooked –maybe a correlation could not be made yet between a known optical center and one of those ESR centers.

The E' generic entity; E'_s point defect

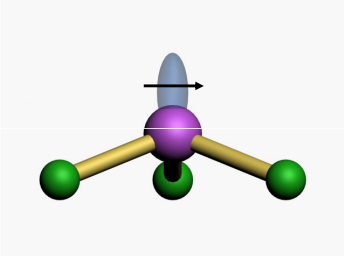

Figure 1.6: The E' generic entity. The unpaired electron is localized on a Si atom backbonded to three O. This model can also be associated with E'_s surface defect, where the unpaired electron orbital points out of the SiO_2 surface.

As pictured in Fig. 1.6, the class of E' centers is typified by the generic entity $O_3 \equiv Si^{\bullet}$[86], where the dot represents an unpaired electron localized in an sp^3-type orbital on a Si atom at the site of an O-vacancy, and backbonded to three O-atoms in the SiO_2 matrix. Some variants may concern multi-Si atoms at the site of multi-vacancies. The symmetry of the atomic configuration is transposed into axial symmetry of $\hat{g}$, if no other perturbing elements are present in the vicinity. The value of $g_3 \approx 2.0018$ (the attribute of the E' family) close to g_e is explained, from angular dependence studies (e.g., E'_1 point defect in α-quartz), by the fact that the unpaired electron orbital has the same direction as a Si–O bond would have [9].

When the E' generic entity is situated at the surface of the SiO_2, facing the ambient, so that the unpaired electron orbital points out of the material, the defect is referred to as E'_s. It can be produced by crushing α quartz or fused silica under high vacuum [87]. Since the perturbation by the ambient of the unpaired orbital is negligible, the axial symmetry of the generic entity is kept as it can be seen from the salient parameter listed in Table 1.2.

E'_γ point defect

ESR has proven to be a very useful tool for point defect investigation of SiO_2 since 1956, when R. A. Weeks [82] first reported a paramagnetic center in neutron-bombarded quartz and fused silica, a center from the E' family, denoted E'_γ. The E'_γ center in a-SiO_2 is the closest analog to E'_1 in α-quartz. The angle dependance of the E'_1 point defect was characterized in detail by Silsbee [86] and theoretically interpreted and atomically described by Feigl et al. [88] and Yip and Fowler [89]. A later refinement by Rudra and Fowler led to the prevailing model of the E'_1 (E'_γ) center pictured as in Fig. 1.7, that is, the called puckered configuration. It is

pictured as a $O_3 \equiv Si^{\bullet} \ldots {}^{+}Si{\equiv}O_3$ unit at the site of an O-vacancy, composed of sp^3-hybridized Si DB ($\equiv Si^{\bullet}$) and a positively charged Si back-puckered through its basal O_3-plane towards a lattice oxygen which effectively becomes three-coordinated [90, 91, 92, 93].

The E'_γ point defect is the most commonly observed variant of the four known E' centers in a-SiO_2 and also, the most studied one. It is envisioned as an unpaired electron strongly localized on a sp^3-type hybrid orbital of the Si atom, backbonded to three O (as the E'_s in Fig. 1.6) but the orbital points in random directions into the silica matrix [38, 94]. While the complete E'_γ model is still under dispute [95], conventionally it is pictured as a positively charged [96, 97] oxygen vacancy ($O_3 \equiv Si^{\bullet}\ {}^{+}Si{\equiv}\ O_3$) [98] as shown in Fig. 1.7, having as precursor a Si–Si bond. There are also reports that incline towards a Si–H bond [99] as the starting point, that, after the dissociation of H, becomes paramagnetic resulting in a neutrally charged E'_γ ($O_3 \equiv Si^{\bullet}\ SiO_4$).

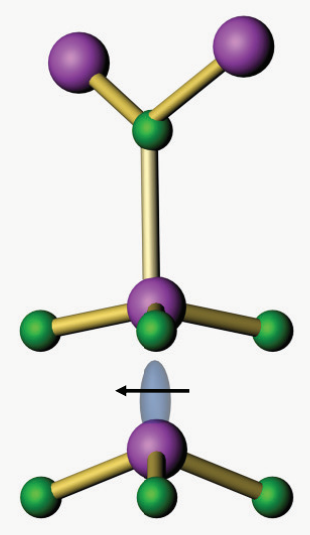

Figure 1.7: The E'_1 (E'_γ) point defect model in the current understanding.

The ground-state configuration of this defect is characterized by a large local relaxation of the atomic network, which leads to a localization of the unpaired electron on a Si dangling bond [93]. The ^{29}Si hf structure of the E'_γ center in γ-irradiated a-SiO_2 was observed first by Griscom et al. [40], revealing an associated doublet with the splitting of $\sim$ 418 G (in relaxed SiO_2), indicating a resemblance of E'_γ to the E'_1 defect in α-quartz first observed by Weeks [82]. Griscom et al. reported an anisotropic contribution on the hf coupling constants $a_{\text{iso}} \approx$ 420 G of $a_{\text{aniso}} \approx$ 22 G [40, 100].

It has been shown that the hf splitting of E'_γ center can change between 410 and 465 G depending on the type and amount of stress at the center site, compressive stress increases, while tensile one decreases the hf coupling and increases the angle the dangling bond makes with the backbonding Si [101]. An extensive overview was given by Stesmans et al. [102] showing again that the E'_γ point defect and the associated hf structure are very good atomic probes of the local structure of the a-SiO_2 matrix.

The presence and density of the E'_γ centers are closely related to the material quality and kind of irradiation damage applied. For standard thermally grown SiO_2 on Si substrates the value of $[E'_\gamma] \approx 3 \times 10^{17}$ cm^{-3} is typically observed [103]. Very long fibers are obtained by drawing a-SiO_2, a process that can break Si–Si bonds (preexisting structural defects) or Si–O bonds, so defects identical to the ones created by irradiation are produced [104], i.e., E' centers [105] made by mechanically induced atomic rearrangement.

E'_α point defect

Griscom [100] first reported the E'_α center as having orthorhombic principal axis g values and a corresponding hf doublet as a result of interaction with ^{29}Si, split by $\sim$ 420 G, the same as for E'_γ and E'_β. The asymmetry of the g matrix is supposed to arise from a Si dangling bond that has in a second neighborhood position an oxygen in a peroxy-like linkage as illustrated in Fig. 1.8, an atom that was displaced from its normal position as a result of irradiation. Initially Griscom [100] reported that the center is stable only at temperatures up to $\approx$ 200K and by exposing the samples at natural light it converts into E'_γ. Later the same author [41] reports the same center as being stable also at RT and with no light-induced conversion to E'_γ.

After Griscom reexamined previously published data, he concluded that the E'_α ^{29}Si hf structure could consist of a doublet split by $\sim$130 G instead of the 420-G split one reported before. On this basis, he revised the atomic modeling, now suggesting a structure consisting of a two-fold coordinated Si (O=Si$^{\bullet}_{\bullet}$, where $^{\bullet}_{\bullet}$ symbolizes a lone pair) which has trapped an electron [9]. Later quantum mechanical calculations [106] also suggested that the E'_α defect could arise from a hole trapped at a two-fold coordinated Si, where it was later inferred that, upon hole capturing, the system relaxes into a metastable state with an unpaired sp^3-like hybrid characterized by a projected $a_{\rm iso} \sim 440$ G. Furthermore, upon hole capture, it may relax into a metastable state of which the stable structure is the E' ($O_3 \equiv Si^{\bullet}$) moiety, giving an explanation for the E'_α - E'_γ conversion reported [100] in some cases.

Buscarino et al. [107] recently reported an E'_α point defect stable even at 630K, with 490 G hf splitting constant that has an associated $\hat{g}$ matrix with values close to the ones listed in Table 1.2, which are observed in the studied materials presented in Chap. 4. Supported by previous experimental [108] and theoretical work [109],

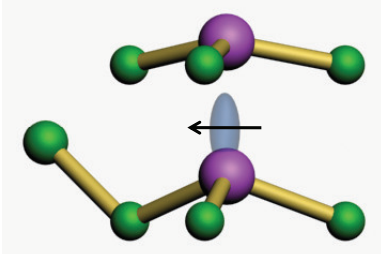

Figure 1.8: The E'_α point defect initially proposed by Griscom [100]. The unpaired electron is localized on a Si atom backbonded to three O atoms, one of them being in a peroxy-type linkage.

they assigned the defect to a hole trapped in an oxygen vacancy, where the unpaired electron sp^3 orbital points away from the vacancy in a back-projected configuration, and interacts with one more O atom in the a-SiO_2 matrix, as depicted in Fig. 1.9 [107]. Trukhin et al. [110] introduces the idea that the E'_α center reported by Griscom [100] and the one reported by Buscarino et al. [107] are not the same point defect because of the different g_2 values —2.0013 vs 2.0009— and dissimilar thermal stability. In a recent report, Buscarino et al. [111] combine optical absorption with ESR to show that the high temperature stable E'_α point defect is optically active at $\sim$ 5.8 eV as also reported before (see Ref. [85] and references therein). They attribute the E'_α center to the atomic structure shown in Fig. 1.9 and explain the wider hf splitting of 490 G by a stronger localization of the unpaired electron on the $O_3 \equiv Si^\bullet$ group rather than to a sharper $O_3 \equiv Si^\bullet$ tetrahedron as is the case for E'_s and densification-caused E'_γ enlarged splitting [101, 112]. It seems that, so far, no unique atomic model has been agreed upon.

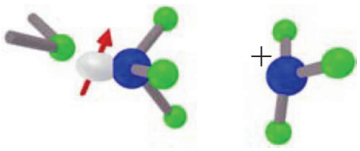

Figure 1.9: The E'_α point defect as introduced by Buscarino et al. [111] and Mukhopadhyay et al. [109], where the green balls represent O, the blue ones correspond to Si. Note that there is no H involvement in this structure.

E'_β point defect

The E'_β point defect [113] exhibits an ESR signal very similar to the one of E'_s but has a somewhat larger $g_\perp$ value as may be seen in Table 1.2. The associated ^{29}Si hf structure is split by 420 G [100], all indicating that the atomic model should be based on the generic E' entity. As pictured, the E'_β creation process is supposed to result of the interaction of a mobile H^0 with some kind of precursor site. Assuming for the latter a preexisting O-vacancy, the E'_β creation is proposed to occur in the range 100-130 K along the process [9]

$$O_3 \equiv Si^{\bullet}_{\bullet} \quad Si \equiv O_3 + H^0 \longrightarrow O_3 \equiv SiH \quad O_3 \equiv Si^{\bullet}. \tag{1.30}$$

It may explain also the axial symmetry of the signal, similar to the one of E'_s, in the absence of a major off-axis perturbation in its vicinity [100].

The E'_β center atomic model is identical to the one ascribed to the E'_2 [83] point defect in α quartz, but better relaxed to account for the negligible proton hyperfine interaction characterized by the presence of a hydride bond in the O vacancy [9]; For E'_2 the splitting due to this proton is $a_{\rm iso} = 0.2$ G [83, 114].

E'_δ defect

The E'_δ center was first reported by Griscom and Friebele [41] in an ESR study (measurement temperature $\sim$ 110 K or higher) on fused silica of diverse OH contents subjected to 100-keV x-ray irradiation at 77 K. The atomic modeling of the E'_δ center remains perhaps the most controversial among all known E'-type centers, where the fact that the E'_δ centers are not as often and as easily observed as the E'_γ signal may play a role. The acquired experimental evidence from ESR analysis in conjunction with electrical probing points to a positively charged [115, 116] defect when ESR active, thus electrically active (a hole trap).

The presumed involvement of Cl impurities in the atomic structure together with the measured spliting of $\sim$100 G of the associated ^{29}Si hf doublet and the fact that the ESR signal is nearly isotropic, led to the idea of a delocalized E'-type defect [39]: the E'_δ center was tentatively modeled as a SiO_4 vacancy dressed with three Cl atoms, with the unpaired spin delocalized over four Si atoms. Thus, its precursor is seen as a SiO_4 vacancy decorated by four Cl atoms bonded to the four Si atoms, from where a Cl atom has been removed by irradiation. The possible involvement of Cl has been disproved in later experimental work [117, 118], herewith raising the need for adapted modeling.

Since various other atomic models have been advanced, including the Si_2 [117], Si_4 [119] which Si_5 [118] models, and all have been subjected to thorough theoretical analysis [109, 120, 121]. Yet, it appears that as yet no convincing assignment could

be made, leaving the scientific community divided on this matter. In this, it comes to the fore that the observed 100-G split hf doublet, that is, correct *quantitative* experimental assignment, plays a key role. It may tip the balance. As part of this work, it has been precisely aimed, as a main target, to significantly expand the experimental knowledge on this E'_δ center through carrying out a multifrequency and temperature ESR study on various types of vitreous silica subjected to three types of irradiation, of which the results are presented in Chap. 4. So, any further detailed discussion of the advanced atomic models for E'_δ, and the various pro's and con's raised over time, will be deferred to Chap. 4.

EX point defect

The EX center was reported as a first inherent point defect grown in during oxidation in thermally grown a-SiO_2 thin layers on c-Si. This is in contrast with the other centers being introduced by post-fabrication treatments (annealings, irradiations, or mechanical actions). First observed in standard a-SiO_2 thin layers thermally grown in dry O_2 on (111)Si [17] or (100)Si substrates [122], it has since been observed in a variety of Si/SiO_2 entities and SiO_2 materials (see Ref. [123] for an overview). In the current work, it is also observed after internal reorganization of low-Si silica materials, i.e., SiO/SiO_2 superstructures (see Chap. 2) and Si^+ implanted SiO_2 discussed in Chap. 3.

The EX center shows an isotropic Voigt shape of width $\Delta B_{pp} \sim 1$ G and with g_c value reported [17, 124, 125] between 2.00247 and 2.0027, and very characteristic, it is accompanied by a hf doublet [17] split by $a_{iso} = 16.1$ G.

The center appears in thin layers when the Si substrate is oxidized at a temperature in the range 700-930 °C, reaching a maximum EX density for $\sim$ 800 °C and is not observable for annealing temperatures outside this interval [122]. It was observed that the EX density increases even four times if the oxides are annealed in vacuum at 775 °C for 65 min [122] or VUV irradiated (as it can be seen in Chap. 2). The defects can be totally passivated (below ESR detectivity levels) by treating the samples in 110 kPa H_2 at 361 °C for 21 min and reactivated by degassing (starting at T $\gtrsim$ 400 °C with a full dehydrogenation obtained for T $\gtrsim$ 550 °C), the passivation-activation cycle [17] thus being reversible. It has been observed that the defect density is not influenced by the specific Si surface crystalline orientation but rather by the precleaning treatments, related with surface roughness and top layer composition.

Depth profiling of the EX centers showed that it resides in the top $\sim$ 4.0 nm, with a maximum at the SiO_2/ambient interface. The density increases with grown oxide thickness up to 12.5 nm, to decrease for larger thicknesses [122]. On the basis of its characteristic ESR parameters, the resolved hf structure, and measurements carried out on ^{17}O-enriched SiO_2 layers, the defect has been tentatively modeled

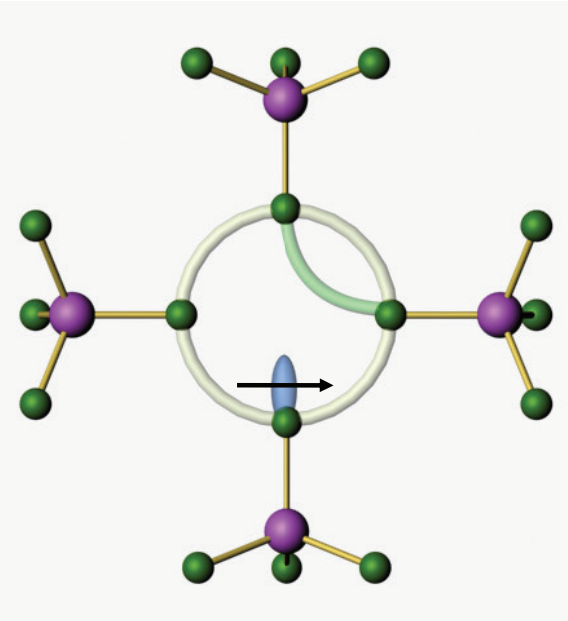

Figure 1.10: Tentative model for the EX center, where the unpaired electron is delocalized over four O atoms at the site of a Si vacancy.

as a structure, where an unpaired electron is delocalized over four O atoms at the site of a Si vacancy, as depicted in Fig. 1.10. In another view, it can be looked at as an agglomerate of four oxygen-related hole center (OHC's).

74 G hf doublet

The 74 G doublet centered at g $\approx$ 2.0016, stems for the E'_{74} defect, ascribed to an E'-type structure [126], where one of the back bonded O atoms in the generic entity is replaced by one H ($O_2H{\equiv}Si^{\bullet}$) [15, 127]. The model is supported by theoretical calculations [128]. The presence of the 74 G doublet is evidence that the O-deficient silica is containing OH groups [129].

120 G hf doublet

The 120 G-doublet is associated with a defect of axial symmetry ($g_\perp = 1.999 \pm 0.001$, $g_\parallel = 1.992 \pm 0.001$), which was attributed by Vitko [126] to an electron trapped at a hydrogen compensated substitutional Ge impurity in ($O_2H{\equiv}Ge^\bullet$) in ^{60}Co γ-irradiated fused silica, which contain a few ppm Ge and hydroxyl ions. The defect does not form when γ-irradiating the glasses at 4 K, but only appears upon allowing the samples to warm up to RT, indicating that H migration might be involved in the defect formation. The two doublet lines differ in shape, indicating that the hf anisotropy contributes significantly to the observed broadening [105]. Hibino and Hanafunsa [105] observed the centers as drawing-induced defects both when starting from GeO_2 doped silica or a-SiO_2 containing only a few ppm Ge. The doublet intensity was found to increase with the surface area of the fiber, indicating that the hydrogen hf interaction takes place at or near the optical fiber surface. As it will turn out in this work, this observation is in accordance with the detected 120-G doublet relative intensity higher than the intensity of other occurring defect hf doublets in the VUV surface activated samples compared to same glasses, where the γ-irradiation is activating defects throughout the bulk of the sample.

Al-related point defects

In the present thesis, we will encounter two Al-related centers: Al E' [46, 47] and $[AlO_4]^0$. The ESR signal of the Al E' center consists of a 6-line structure resulting from the hf interaction of the unpaired electron with an Al nucleus (I = 5/2; η = 99.9 %). The 6-line signal was first observed by Brower [46, 47] in natural vitreous silica exposed to ionizing irradiation and was attributed to Al E' centers, an electron captured on an ^{27}Al atom in a Si-substitutional position bonded to three oxygen atoms in the a-SiO_2 matrix.

Noteworthy is that this center, $O_3 {\equiv}Al^\bullet$, is in the negative charge state when ESR active (an electron trap), unlike, along current understanding, the familiar Si E'-type centers, such as E_1' (E_γ'). Pertinent also is that the center was found to require a charge compensator in its vicinity to remain paramagnetic (ESR-active) above 57 °C; it stays paramagnetic up to 277 °C if stabilized by alkali ions, and up to 377 °C if hydrogen is involved. Otherwise it turns to its neutral, diamagnetic $Al{\equiv}O_3$ ($AlO^0_{3/2}$) state. As analyzed in detail [46, 47], both the hf coupling matrix but also the g matrix are affected by the compensating agent (see [47]).

The $[AlO_4]^0$ signal is attributed to an Al atom substituting for a four-coordinated Si with an unpaired electron in a 2p nonbridging oxygen orbital [43], as illustrated in Fig. 1.11. The center is neutral when ESR active. It is almost axially symmetric, characterized by the principal g values $g_1 \sim 2.06000$, $g_2 \sim 2.00854$, $g_3 \sim 2.00195$,

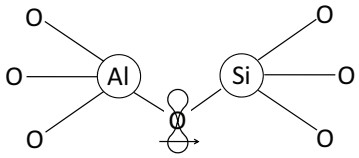

Figure 1.11: Schematic of the neutral, ESR active $[AlO_4]^0$ center in SiO_2.

as reported in the literature for the center in crystalline [46, 47] and vitreous [44] silica. The X-band spectrum can be well simulated by a powder pattern using these g values and a Lorentzian broadening function of 6, 6.5 and 10.5 G for the directions g_1, g_2, and g_3, respectively, with inclusion of a a_{iso} = 8.5 G ^{27}Al hf splitting (this work).

1.2.4 SiO_x materials

The S center

Using X-band ESR spectroscopy, Friebele et al. [104] reported in 1976 on an unknown center, labeled S center, at g= 2.0022 with ΔB_{pp} = 3-4 G observed in dry silica drawn into fiber and subsequently heated above 350 °C under vacuum. The center was speculated to arise as a result of removing O from a silica network. The signal disappeared after annealing the samples in oxidizing atmosphere. When measuring SiO_x ($0 < x < 2$) material, Holzenkampfer et al. [130] observed, besides the well known P_b ($Si_3 \equiv Si^\bullet$) –the archetypal (111)Si/SiO_2 interface defect– and the a-SiO_2-specific E'_γ centers (both introduced above), two signals with g_c between 2.001 and 2.004 which were attributed to $Si_nO_{3-n} \equiv Si^\bullet$ (n=1, 2) [130] as depicted in Fig. 1.12. Later, these centers were called either S (the n = 1 variant and/or a combination of both) [131], or X (n = 1) and Y (n = 2) [132] centers. According to current understanding, the S center [33, 34] (see Table 1.2) is attributed to [37] the n=1 variant ($SiO_2 \equiv Si^\bullet$) intermediate [130, 133] between E'_γ and P_b. This signal is reported to be Lorentzian, with a slight g matrix anisotropy [35]. It is not only observed in SiO_x but also in high temperature vacuum annealed SiO_2 after X-ray irradiation [131], in Si/SiO_2 structures after post-oxidation high temperature annealling in O deficient ambient [33], in high-purity quartz [134], and in Cr ion-implanted a-SiO_2 [132].

Stesmans et al. [35] reported two (^{29}Si) hf doublets, of splitting $a_{\text{iso}} = 162 \pm 5$ G and 279 ± 12 G with relative intensity to the central line indicating the unpaired electron to be delocalized over one Si atom, in accordance with the proposed models. Yet, the interpretation is obstructed by the low intensity of the hf signals intensity. Two hf doublets centered on the S main signal can indicate the hybrid to be a mix

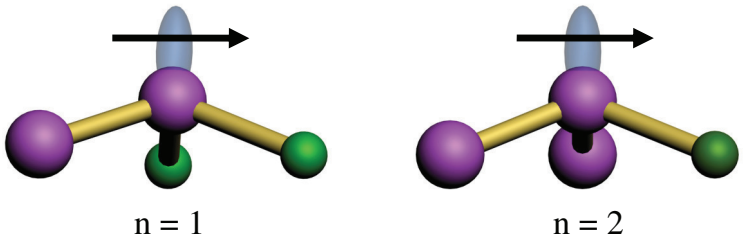

Figure 1.12: The Si_nO_{3-n} ≡$Si^{\bullet}$ entities, assigned to S (a combination of the two or only the n = 1 variant) or X and Y for the n = 1 and 2 respectively.

of the two variants (n = 1 and 2) or a result of only [37] the n = 1 configuration influenced by the two Si sites. From *ab initio* Hartree-Fock calculations a hf doublet for each (n = 1 or n = 2) configuration was obtained [135]: $a_{\parallel}$ = 294 G and $a_{\perp}$ = 224 G for n = 1, and $a_{\parallel}$ = 245 G and $a_{\perp}$ = 169 G for n = 2. Later, Stirling and Pasquarello [37], using the generalized gradient density functional approach, found two doublets split by 315 and 202 G, for the SiO_2 ≡$Si^{\bullet}$ configuration. These results were concluded to be well in agreement with experiment if taking into account the tendency for their theoretical approach to predict larger than actual values [136]. Although the main signals named as S or X are very similar and were ascribed to the same atomic models, there are differences between the two concerning the hf structure, where for the latter often a single doublet is reported with the splitting fluctuating [34, 36, 133] between 230 and 289 G. The smaller splitting doublet signals were calculated to be broader [37], or observed to be slightly less intense [35], thus more difficult to be observed.

1.2.5 C-related point defect

Photolitography, using photosensitive material, is a standard technique to obtain the desired 'layout' for semiconductor electronics by selectively covering/removing, as many times as needed, areas of thin layers or bulk materials. Usually the photoresist material is C-based, so, the substrate on which it is deposited can be contaminated. Also SiC materials have been intensively studied for their bandgap changing from 0 to 4 eV by just varying deposition conditions [137]. An ESR signal is visible in all those C based materials, a Lorentzian [50] with $\Delta B_{pp}\sim$ 1-3 G [51] of $g_c \sim 2.003$ arising from disordered SiC regions or C agglomerations [138] in a-SiO_2 [139], SiC [140], or graphite [141].

1.2.6 N-related point defects

N_2 is a common ambient for annealing Si/SiO_2 structures but cannot be considered as an inert gas above $\sim$ 1200 °C for shorter annealing times and above $\sim$ 925 °C for long ones. There are numerous reports on this matter, with effects on various physical/chemical parameters. Nitrogen competes with O for the Si reaction sites [142], thus decreasing the paramagnetic defect density [143], mainly P_{b1} [144], but it can also create fixed oxide charge [145] after reduction. Incorporating N into a SiO_2 glass matrix can be beneficial for creating a diffusion barrier layer, improving thermal stability and electrical properties, and increasing κ [146]. When impurities are present in the gas phase in the N_2 ambient (as, e.g., H_2 in forming gas), the nitrogen reacts with Si even at $\sim$ 760-1050 °C, creating ultrathin oxinitride films near the interface [147] and reducing the concentration of strained Si–O bonds, inhibiting [148] the generation of interface states during electrical stress of the Si/SiO_2 interface. In manufacturing nc-Si/SiO_2 structures, the choice of the annealing ambient between Ar, N_2 or forming gas (5% H_2 in N_2) is found to influence the shape and intensity of luminescence emission by varying the attained nc size (smaller in the case of N_2 annealing) and defect states at the nc-Si/SiO_2 interface. It has been concluded that the annealing in N_2 results in a thermal relaxation compounded by the exchange of N with the oxide network, improving the degree of surface passivation [149].

Perhaps the best known N-related defect in $Si_xO_yN_2$ and Si_3N_4 materials is the K center [48], where the unpaired electron is localized mainly on a Si atom, bonded to three N atoms, usually in stoichiometric Si_3N_4 (used as insulator in insulated gate field effect transistors, non volatile memory devices [150], MOS solar cells, etc.). The signal can be simulated by a $\hat{g}$ matrix and hf coupling constant resulting from hf interaction with the Si atom as listed in Table 1.2. The interaction with the N nucleus gives rise to a triplet characterized by $a_{\text{iso}} = 4.6$ G and $a_{\text{aniso}} = 0.45$ G [151] overlapped by the main signal. This signal, of $g_c \approx 2.003$, is usually $\sim$ 12 G broad and looks like an isotropic symmetric signal, somewhat similar to the C center described above. When ESR active, the center is neutral but may capture an electron or hole, becoming charged but diamagnetic [48], assumed to be the dominant trapping center [151, 152] in silicon nitride-based materials. The K centers are ESR activated by UV photons which change the spin state, and thus the charge of the point defect [48].

Part of the same family is the N center observed in a-Si_3N_4. It is ascribed to a dangling bond localized ($\sim$ 69 % [49] experimental value and $\sim$ 85 % [153] theoretical one) on a N atom, bonded to two Si atoms [49]. This signal is characterized by $g_c \approx 2.003$ and an associated hf doublet split by $\sim$ 61-70 G [49].

Now that the ESR point defects encountered during the research presented in this thesis have been introduced, we proceed to present the subjects studied and results obtained. In the next two chapters, Si nc's embedded in a-SiO_2 obtained

by two different fabrication methods (superstructure approach and UST during Si^+ implantation in a-SiO_2) will be discussed. The fourth chapter is focused on the identification of the E'_δ point defect studied in various types of a-SiO_2 by a multifrequency ESR approach.

Chapter 2

Inherent paramagnetic defects at the nanocrystalline Si interface with SiO_2 layered Si/SiO_2 superstructures

2.1 Introduction

Bulk Si, an indirect band-gap semiconductor, is known for being an inefficient light emitter because of the low probability of band-to-band optical transitions and the non-radiative recombination of most of the electron-hole pairs. Neither nanometer-size Si appears to become a direct semiconductor [154], but was shown to be room-temperature photoluminescent [155]. In order to stabilize the surface of nc Si and at the same time preserving, and even improving the luminescent properties [156], the preferred approach is embedding it in an insulating oxide, preferably a-SiO_2 given the generally high quality offered by the (thermal) Si/SiO_2 interface. This type of structure is being introduced in everyday life, such as CMOS where Si nc's are embedded in the gate oxide [4, 5], with applications in FLASH memories [6], silicon [156] LED's that are yet not stable enough for the market requirements [157, 158, 159], and usage in photovoltaic applications [7] and solar cells reaching an efficiency over 16%, both on rigid and flexible substrates [2, 160]. Two more eye catching applications are the Si-based laser [2, 161] and quantum computers [161], both thought to be achievable with this type of structure. Therefore, what bulk Si may inherently not enable, the nc form might do. Evidently, with so many applications already present and many more projected for the future,

a good theoretical and practical understanding of the properties of the nc-Si is desired.

Starting with Canham [162] and Lehmann and Goesele [163], quantum confinement [154, 155, 164, 165, 166, 167, 168] was suggested as explanation for the observed Si room temperature luminescence. Later, other models have been invoked, including generic defects at Si/SiO_2 interfaces (yet, without rigid quantification and identification of the varieties [169, 170, 171, 172, 173, 174]), the influence of multiple Si=O bonds at the cluster surface [175, 176], and the Auger effect [177, 178]. As it appears, not all the data so far assembled can be explained based on only one hypothesis: According to the current insight, the PL may be originated by a superposition of two or more mechanisms [179, 180, 181, 182, 183]. Increasing effort is put in the understanding of the PL processes and its improvement, with some questions still left not wholly answered.

Since the initial discovery of PL properties, research on nc-Si has boomed, with many analyzing tools being introduced. Theory, experiment, and technology collaborate with the intent of understanding the optical processes that take place and make more efficient and industry friendly optically active Si-based materials. Many top characterization techniques have been applied, such as the morphological tools (TEM [6, 184, 185], AFM [4, 186] and EFM [186]), in combination with SAXS [187] and optical measurements, mainly PL [162, 177, 188, 189, 190]. Additionally, a growing number of electrical analyzing techniques, like I-V [190], C-V [4, 191], G-V [6], electron beam induced current [190], as well as theoretical in situ calculations of different physical properties [192, 193] are being used in the attempt to understand the origin of the exhibited PL phenomena.

The morphological methods mentioned can investigate only a small fraction of the np's, present in a certain volume, and most of them cannot discriminate between a-Si and a-SiO_2, making it unable to draw conclusions about the presence of a-Si np's. Here, ESR can provide an answer, being a technique sensing the whole body of the sample and being able to distinguish between different materials by using paramagnetic defects as a probe: ESR can identify these paramagnetic defects and infer their location within the sample structure.

Efficient photoluminescent Si np's, generally crystalline, embedded in SiO_2 can be fabricated through a variety of methods, including (oxidation of) p-Si [194], CVD, rf cosputtering method [166], PCVD [155], Si^+ implantation in high purity SiO_2 [195, 196], and so forth. Yet, major problems these techniques suffer from include the tight and, in particular, density independent control of the nanoparticles size, the control of the inter-nanoparticle distance and prevention of particles agglomeration. Evidently, such "hands-on" tight control of the incorporated particle size and spacial (statistical) distribution would be highly desirable to enable a systematic study. Interestingly, the above mentioned inconveniences may be avoided by using the SiO_x/SiO_2 superlattice approach [197], where different morphological parameters

of the obtained structure can be independently controlled, essentially an inherent attribute of the systematic fabrication approach.

Previous ESR investigations

There have been various studies on n-Si entities in SiO_2, the reports generally encompassing five types, i.e., D (Si dangling bonds in disordered Si), $P_{b(0)}$, P_{b1}, E'_γ and EX (vide infra). All works invariably report on a generally featureless line –commonly referred to as the Si DB signal– of zero crossing g value g_c in the range 2.005-2.006. A first series of ESR measurements have been performed on Si np's embedded in SiO_2 and phosphosilicate glass fabricated by Si^+ ion implantation and subsequent annealing [198, 199, 200]. A rather broad signal with peak-to-peak width ΔB_{pp} = 7.0 - 7.9 G situated at around g_c = 2.006 was observed, which was suggested as originating from P_b-type centers.

Three more works pay particular attention to the determination of the exact defect origin of the above signal. Two of these concern Si nanowires (SiNWs) embedded in SiO_2 [201, 202], proposing two different explanations: One [201], studying c-SiNWs of ∼10-15 nm in diameter and reporting the signal at g_c = 2.0065, proposes Si DBs or P_b centers at the SiNW/SiO_2 interfaces as the source, excluding D centers as candidates as the signal was found almost entirely eliminated after removal of the Si oxide by immersing in aqueous HF (5%) solution. Without further addressing the type(s) of P_b centers, these authors also report the observation of a weak E'_γ resonance and a prominent EX signal in the as grown sample. The other work [202] argues in favor of the a-Si specific D center, adducing support from the observation of a similar feature [81] in a-Si:H. Here, we should point to the dimensional and morphological difference between NWs and np's that could result in dissimilarities regarding crystallinity and presence of defects.

A more detailed ESR analysis on the origin of the Si DB signal was reported by Bratus et al. [203] studying nano-Si particles formed in evaporated SiO films after annealing. After annealing at 1100 °C (15 min), a Si DB signal was observed at g_c ∼2.0061, which, via computer simulation, was described as a superposition of three components implying a strong D line, modeled as a Lorentzian signal at g_c = 2.0058 and ΔB_{pp} = 6 G, and powder pattern signals from chaotically oriented P_{b0} and P_{b1} defects in a ratio 5.5:1:1, respectively. Remarkably, the observed substantial density of D centers would indicate that most of the Si np's are in fact amorphous (or polycrystalline), contradicting previous morphological investigations. As in all previous reports, the applied X-band (∼9.4 GHz) spectroscopy clearly delimits spectral resolution and disentanglement. More in depth and reliable signal discrimination will require experimental extension, e.g. additional observational frequencies.

2.2 Paramagnetic point defects at the nc-Si/SiO_2 interface in layered superstructures

2.2.1 Introduction

In an attempt to take the ESR signal discrimination and assignment to the next decisive level, we here present an ESR analysis on a prototype SiO/SiO_2 superstructure with regular arrays of Si np's embedded in an a-SiO_2 matrix, where the experimental ESR range has been extended to three observational frequencies (X, K, and Q-band) and two detection modes (first and second harmonic). With reliable attribution of the signals, dangling bonds can be used as probes providing information about the crystallinity and bordering of the Si np's.

As a major result, the occurring main DB signal could be disentangled as solely composed of a mix of the Si/SiO_2 interface specific $P_{b(0)}$ and P_{b1}, resulting in particular conclusions regarding the Si np's state, morphology and crucial defect nature. Using the inherent point defects as local probes, it leads us to inferences on the nature and quality of the inner nano-Si/SiO_2 interfaces and a-SiO_2 matrix these are embedded in.

2.2.2 Experimental details: sample preparation

The samples studied were prepared using the SiO_x/SiO_2 superlattice approach, as extensively described by Zacharias et al. [197]. In short, an alternation of SiO and SiO_2 layers with thicknesses of 2 nm respectively 4 nm is deposited on a 500 μm thick p-(100) Si wafer by reactive evaporation of SiO powder in low pressure of the oxygen of $\sim 1 \times 10^{-7}$ mbar and $\sim 10^{-4}$ mbar, respectively, to obtain the desired stoichiometry of the layers. In the current case, 45 such two-step processes were sequenced, resulting in a total thickness of the superstructure of 270 nm. Finally, the sample was subjected to 1100 °C annealing in pure N_2 (1 atm) for 1 h. During this step, first a phase separation of SiO molecules into Si and SiO_2 [204, 205] takes place, followed by atomic/molecular migration resulting in Si agglomeration. The anneal temperature should be sufficiently high for the Si nanoparticles to become (nano)crystalline [206].

Prior to ESR observations, PL measurements were carried out on the samples to establish the size of the Si np's. With respect to ESR observations, the influence of this irradiation can safely be disregarded because it will only have affected a surface size with a diameter of $\sim$0.3 mm (area $\simeq 7.07 \times 10^{-4}$ cm^2), insignificant when compared to the total surface of the ESR sample: the defects that might have created/activated will be well below the detection limit of current ESR measurements.

For the ESR measurements, slices of 2×9 mm^2 were cut of which, after protective covering of the front side, the cutting damage and backside oxide were selectively removed though wet chemical etching (CP4). The protective cover was removed before subjecting the superstructure face to irradiation treatments (photon flux). Typically, for dimensional reasons, only four slices could be stacked in one ESR sample, thus limiting the probed superstructure surface to $\sim$0.72 cm^2, and hence the number of the paramagnetic centers that could be probed in one sample, rendering spectroscopy rather laborious.

2.2.3 Experimental details: sample structure

To get more morphological insight, PL measurements [207] were performed on samples investigated here concluding the presence of n-Si particles with average diameter (Gaussian distribution) of 2 ± 0.25 nm.

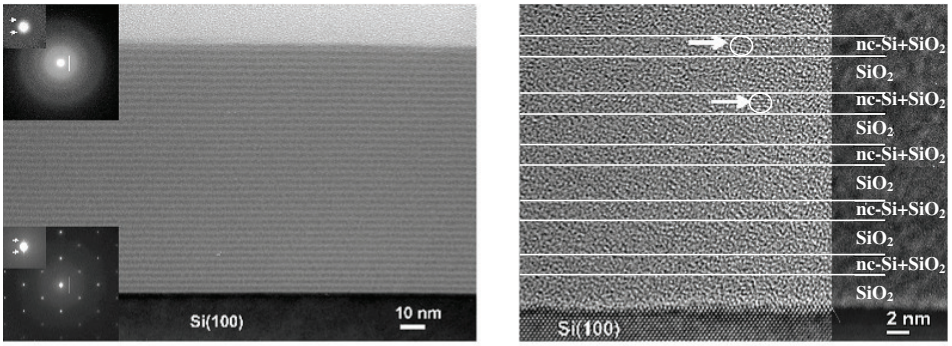

Figure 2.1: Cross-sectional TEM images of the same annealed SiO/SiO_2 superlattice sample as measured by ESR. (a) as-annealed structure: the lighter layers represent the SiO_2 layers, which do not change during annealing, while the darker ones are the the initial SiO layers in which the nc-Si are formed during annealing. Here, 37 bi-layers can be measured as being left after annealing from the 45 deposited one. The inserts are ED patterns taken on the Si-substrate/film (bottom) and from the film only (top). This proves the formation of nc-Si. (b) The HRTEM image of the annealed structure where the agglomerated Si particles are seen to be present only in the former SiO layers and none in the SiO_2 ones as indicated on the right side. For clarity, two nc-Si are indicated by arrows but are not the only nc-Si observable.

Physically the same samples as measured by ESR have been investigated by high resolution transmission electron microscopy (HRTEM) and some images are shown in Figs. 2.1 and 2.2. The two layer alternation is evident in Fig. 2.1(a), the light color indicating the SiO_2 layers deposited to delimit the SiO layers in which, during high-T anneal, Si atoms agglomerate and crystallize into nc-Si shown in darker color.

Electron diffraction (ED) patterns taken from the Si-substrate/film (bottom insert in Fig. 2.1(a)) and from the film only (upper insert in Fig. 2.1(a)) exhibit two major structural features of the film: the presence of superlattice spots due to the almost perfect multilayer structure of the film; a diffuse weak intensity ring pattern of the film. This ring pattern can be indexed based on the structure of Si and the diffuse rings can be explained by the very small size of the nanocrystals. The TEM investigation showed the presence after annealing of only 37 bi-layers (instead of the initially deposited 45), indicating that part of the deposited layers have been annealed away during fabrication. Noteworthy is that there are no nc-Si precipitates in the initial a-SiO_2 layers, the Si particles being all formed only in the deposited SiO layers as seen from Fig. 2.1(b). These HRTEM data confirm the presence of n-Si particles with size in the range of 1.5 - 3 nm, somewhat extended laterally, the growth perpendicular to the layers apparently being confined by the SiO_2 layers. Thus, the resulting sample is composed of generally nc-Si particles as theory would suggest [208, 209, 210], positioned within the initial SiO layers, embedded in an SiO_2 matrix [204]. Theoretical reports [209, 210] indicate the nanoparticles to be strained .

In an attempt to investigate the nc-Si facets, HRTEM imaging [207] was performed on individual Si agglomerations as illustrated in Fig. 2.2. The Si particles formed after high temperature anneal are crystalline and appear bordered by (100) and (111) facets amid a surrounding SiO_2 matrix as it will be concluded also from ESR measurements (see later), conferring confidence to the Si nanocrystals modeling in Sect. 2.2.10.

From PL intensity data and inferred flatband shifts from C-V measurements previously reported [211] for samples prepared along the same fabrication lines, the number of Si np's is estimated at 3×10^{12} cm^{-2} per SiO/SiO_2 bilayer –a figure that we will later use in inferring ESR defect densities.

2.2.4 Experimental details: ESR spectroscopy

In the attempt to identify and quantify as accurately as possible all the paramagnetic defects within the Si np's/SiO_2 superstructure, ESR experiments were carried out at multiple frequencies of the microwave excitation, using three different spectrometers, i.e., X- (∼9.5 GHz), K- (∼20.5 GHz) and Q-band (∼34 GHz), usually driven in the adiabatic mode. Routinely, conventional low-power first

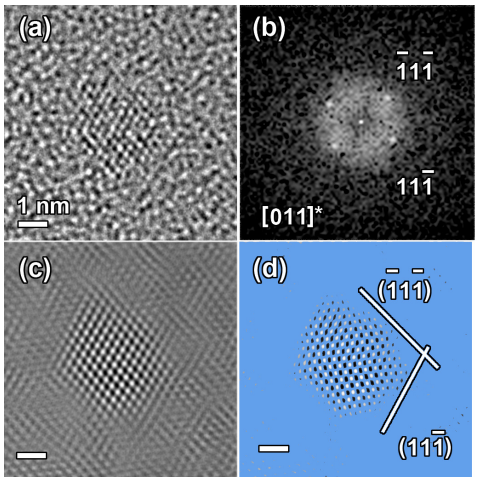

Figure 2.2: Imaging of Si nanoparticles by HRTEM. (a) Image of a single Si nanoparticle along the [011] zone axis. (b) Corresponding Fourier transform. (c) Bragg-filtered HRTEM image. (d) Bragg filtered image after subtraction of the background. This clearly highlights the (111) and (100) faceting of this nanoparticle. [207]

derivative-absorption (dP_μ/dB) spectra were measured through applying sinusoidal modulation ($\sim$100 kHz; amplitude $B_m \simeq 0.77$ G) of the externally applied static field $\overrightarrow{B}$. These were complemented with high-power second harmonic dispersion mode measurements (See e.g., Ref. [14]) (saturation spectroscopy) in an endeavor to unequivocally disentangle all the appearing signals. For microwave dissipation reasons, ESR experiments routinely had been carried at a temperature $T \lesssim 30$K. While generally beneficial for signal detectivity (Boltzmann factor, noise levels, etc.), low-T measurements suffer from enhanced sensitivity to signal saturation (distortion) effects with decreasing entropy, which mandated appropriate reduction of incident microwave power P_μ, as well as B_m, to such levels causing no visible first-derivative signal distortion. Signal-to-noise ratio was improved by appropriate signal averaging (typically $\sim$100 scans).

Paramagnetic defect densities were determined through double numerical integration of the detected dP_μ/dB signals by comparison to the signal of a co-mounted point-like Si:P marker [18] (S=1/2), which also served as a g marker (see Sect. 1.1.6). Proper corrections for the relative position of the sample and of the marker in the cavity were taken into account when calculating the absolute intensity of detected signals.

Table 2.1: Overview of applied irradiations on the Si/SiO_2 phase separated samples

Label[1]	Irradiation source	Wavelength (nm)	Energy (eV)	Irradiation time (h)
1a	*as received sample*			
1b	He-Cd laser	325	3.80	22.5
1c	Xe lamp	362	3.42	71
1d	Xe lamp	180-1000	1.23-6.87	10
1e	Kr lamp	123	10.02	0.17
2a	*Annealing in H_2 (99.9999 %, 1 atm) for 30 min at 400 °C*			
2b	Ar-ion laser	351-364	3.40-3.52	330

[1] Digits 1 and 2 refer to two physically different samples cut from the same wafer, while the letter symbol marks different post manufacturing (photonic) treatments, as detailed in the table.

2.2.5 Experimental details: post manufacturing treatments

The as manufactured sample (termed 1a) was extensively investigated by low-power first harmonic K-band ESR to reveal occurring defects and assess densities. After initial ESR observations on the *as received* samples, physically the same sample slices have been successively exposed to different photonic treatments, as summarized in Table 2.1 (sample sequentially labeled 1b to 1e according to applied irradiation step).

The application of the various irradiation steps is multi purposed. (1) A first one is the investigation of the possible presence and effect of hydrogen on the various types of paramagnetic point defects. For example, as well known, Si-dangling bond type defects, such as P_b-type centers at the Si/SiO_2 interface, D centers in amorphous or polycrystalline Si and E' centers in SiO_2 may readily be ESR inactivated through bonding to H. So, while distinct systems of defect sites may occur, these may fully escape ESR detection. Here, VUV has been found to be very effective in cracking Si-hydrogen bonds, thus enabling to reveal defects through ESR observation; (2) Appropriate photonic irradiation may reveal weak (strained) bonding sites at interfaces and amorphous networks through bond breaking, thus enabling through ESR identification to asses inherent interface and layer quality in terms of such less-than-ideal bonding sites; (3) In relationship to the latter, an interesting, and perhaps most vital item, is to investigate how the laser irradiation may "in situ" affect the point defect system during the process of PL measurements, thus potentially modifying the PL response –drift– in the course of the measuring process itself with corresponding uncertainty on the PL data interpretations as

a result. For one, gradual production of paramagnetic point defects would likely affect PL properties, such as intensity and range. While PL investigations so far did not report such variation occur, it has not been accurately analyzed in combination with ESR observation.

It is important to note that all the irradiations performed were applied to the entire surface area of interest (the superstructure side) of the samples, to ensure a maximum effect on the ESR signals. In the case of laser irradiation, this required use of defocusing lenses, a process that strongly decreases the illumination efficiency thus mandating significantly extended exposure times if to obtain equivalent photonic impact per sample area as effectuated by a laser spot. The first optical irradiation was made using a He-Cd laser emitting at ∼325 nm (∼3.80 eV) for 22.5 h (sample 1b), the electrical power of the source being 15 mW. Because the irradiation by this lamp might not be sufficient to activate all occurring intrinsic defects, second and third irradiations (labels 1c and 1d) were performed using a Xe lamp with an electrical power of 40 mW, more than twice stronger than the first. For the second irradiation (1c; first Xe lamp step, 71 h) an interference filter was initially interfaced between the lamp and the defocusing lens to select a photon window of 362 ± 20 nm (∼3.42 eV), close to the wavelength of the first irradiation. In the third irradiation, the full UV spectrum, (∼180-1000 nm), of the lamp was applied for another 10 h (sample 1d). The fourth irradiation was done in the VUV spectral range using a Kr resonance discharge lamp foreseen with MgO_2 output window at wavelength of ∼123 nm (10.02 eV) for 10 min. All the above luminous treatments have been applied successively on the same sample, where after each step K-band ESR measurements were performed to analyze the effect brought about on paramagnetic defects.

To investigate the influence of the Ar-ion laser used as excitation source in the PL measurements performed on these type of samples, a fresh *as received* sample, cut from the same part of the wafer, was subjected to the same thinning and cleaning processes as applied to the previous sample. As a first step, this sample was exhaustively passivated in molecular hydrogen (1 atm; 400 °C) for 30 min (sample step 2a), leaving, indeed, no observable ESR signal. Next, the sample was subjected to 351-364 nm (3.4-3.5 eV) Ar-ion laser irradiation using a defocusing lens, for 330 h, followed by another K-band ESR observation (sample 2b), the equivalent of the doses applied in PL measurements [212].

Both of the above described samples, 1e and 2b, were additionally subjected to extensive X and Q-band ESR with the intent to provide one more experimental dimension, i.e., observational frequency, in helping to discriminate between and disentangle the various occurring type of defects, in particular, the different types of dangling bonds corresponding to Si.

2.2.6 Results: occurring paramagnetic defects

Figure 2.3 shows a low-power first derivative K-band spectrum measured at 4.2 K on the *as received* sample (1a). Besides the reference signal, we observe a rather broad signal exhibiting some additional features. Provisionally, we label the signal as DB, as its zero crossing g value g_c ∼2.0055 situates in the range of Si DB signals, such as P_b-type defects at the Si/SiO_2 interface [28] ($g_{iso} = \frac{g_{\parallel}+2g_{\perp}}{3} \approx 2.0058$) or dangling Si bonds in disordered Si (g_c ∼2.0053-2.0058) [79]. We can also safely say that the feature is a superposition of at least two signals, but any attempt of reliable disentanglements is deferred to the availability of additional measurements.

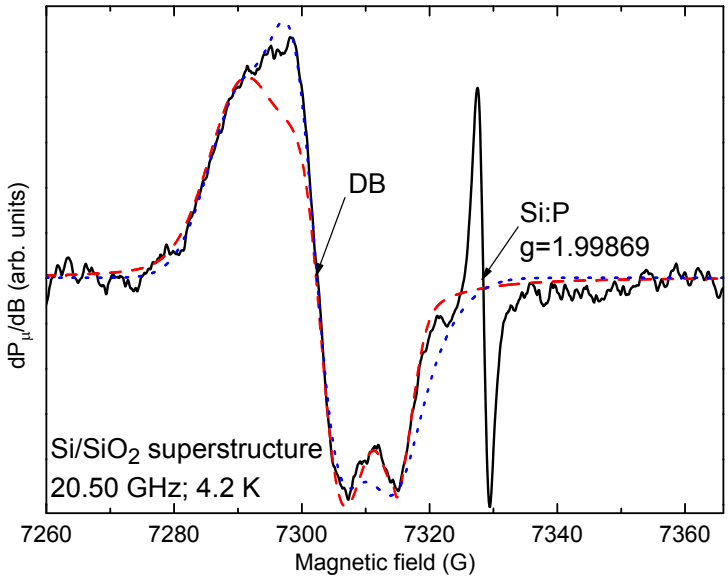

Figure 2.3: First derivative-absorption K-band ESR spectrum (sample 1a; 41 cumulative scans) observed on *as received* phase separated Si/SiO_2 superstructures, measured at 4.2 K using B_m = 1.0 G and reduced $P_\mu = 7.9 \times 10^{-10}$ W to avoid signal distortion. The broken curves represent optimized simulations of the main left signals (denoted DB) through combining overlapping powder patterns corresponding to randomly orientated $P_{b(0)}$ and D centers (dashed curve) and randomly orientated $P_{b(0)}$ with P_{b1} centers (dotted curve), respectively, using the principal g values listed in Table 2.2. The signal at g ∼1.99869 stems from a co-mounted Si:P marker sample.

Angular dependent ESR observations as a function of the direction of the applied field $\overrightarrow{B}$ with respect to the sample surface normal $\overrightarrow{n}$ (angle φ_B) indicated the signal to be isotropic, i.e., φ_B-independent. Taking into account the composition of the

Table 2.2: Principal g tensor values used for the D, $P_{b(0)}$ P_{b1} defects in simulating the ESR spectra of phase separated Si/SiO_2 superstructures, as shown in Fig. 2.3. These values have been used also for the simulations needed for each of the defect density determinations (error: $\pm$ 0.0001).

Type of defect	g_1	g_2	g_3
D	2.0055	2.0055	2.0055
$P_{b(0)}$	2.0015	2.0080	2.0087
P_{b1}	2.0020	2.0055	2.0070

samples, that is Si np's, embedded in an a-SiO_2 matrix, defects can appear within a-Si (we disregard the possibility of defects in the inner part of nc-Si particles), at the Si/SiO_2 interface, and inside the bulk of the SiO_2. As to the first two cases, predominant defect types will entail Si-related dangling bonds. Among this defect family, we can distinguish, depending on location, two kinds, i.e., D centers and the P_b-type centers. The former concern Si dangling bonds located in disordered Si, characteristic, e.g., for amorphous (and polycrystalline) Si, where the long distance order is disturbed and not all the atoms are completely bonded, giving an isotropic signal [79, 80, 81]. The second kind, the P_b-type centers, concerns the inherent three fold Si type Si/SiO_2 interface centers, whose modalities (occurrence, type, density, etc.) and orientation strictly correspond with the c-Si substrate face [26, 213, 214] [e.g., (100), (110) or (111)]. Moreover, for each P_b-type, the g matrix is anisotropic (axial or orthorhombic), the ESR signals thus exhibiting φ_B dependence. But obviously, when occurring in an ensemble of randomly orientated c-Si/SiO_2 interfaces (as, at least for a main part, evidenced to be the case in the current samples [197]), if only for one type of c-Si face and one type of P_b defect, a general overall 'isotropic' signal will appear, a *powder pattern*. If more than one type of c-Si substrate face and/or kind of P_b-type defect involved, accordingly more powder patterns will be found superposed, thus aggravating the task of signal disentanglement, and hence delineation of occurring types of (interface) defects and sorts of c-Si/SiO_2 interfaces. In case of the current n-Si/SiO_2 superstructure, such deconvolution is highly desired in order to assess the true microscopic nature of the Si/SiO_2 interface of the embedded (c-) Si particles in terms of, e.g., occurring c-Si faces, interface strain, etc. It is here where detailed ESR study may provide a major contribution.

So, in case of a particular interface defect at a particular c-Si/SiO_2 interface orientation, e.g., P_{b1} in (100)Si/SiO_2, with many (100) planes (facets) occurring spatially randomly orientated, a P_{b1} powder pattern ESR shape will result. This, for example, would be expected for (100)-facetted nc-Si particles embedded in a SiO_2 matrix with no correlation between interparticle orientations. On the other

hand, should the nc-Si particles occur in crystallographic registry, then of course the anisotropic P_{b1}, ESR signal(s) as pertaining to the macroscopic (100)Si/SiO_2 interface would be observed. Clearly, on this matter, ESR may provide exclusive information. Clearly also, the above will apply for each type of interface defect at each type of interface orientation (facet). Thus, if we would expect to deal with an ensemble of facetted nc-Si particles randomly oriented within an otherwise a-SiO_2 matrix, we might expect an overlap of several P_b-type powder patterns, i.e., P_b at (111)Si/SiO_2, P_{b0} and P_{b1} at (100)Si/SiO_2, and P_b at (110)Si/SiO_2.

Depending on preparation conditions there are some minor differences in ESR parameters between P_b and P_{b0} (and P_b in (110)Si/SiO_2) as well (see e.g., Ref. [28] for more details). However, within the current simulation context, we consider any achievable discriminative analysis on this matter beyond reach. So, we will as onset restrict defect involvement in the observed DB signal to two P_b-type powder patterns. Forcing a fitting of the observed spectrum with a multiple of powder patterns would of course boost a successful, apparently perfect fitting, but obviously at the cost of scientific credibility. Further, given the fundamentally identical nature of P_b and P_{b0}, and thus the close g tensors [25, 28], we will henceforth use the notation $P_{b(0)}$ in denoting the common powder pattern. Thus, as synthesis, we consider we might have to differentiate between three overlapping powder pattern signals, corresponding to D, $P_{b(0)}$ and P_{b1}-centers, and proceed computer-assisted simulations of the observed DB spectrum that way.

In Fig. 2.3 are shown two optimized fittings to the experimental K-band spectrum, each based on two overlapping components, i.e., $P_{b(0)}$ and D centers (dashed curve) and $P_{b(0)}$ and P_{b1} signals (dotted curve), using the principle g values listed in Table 2.2. These appeared the best simulations attainable. Both may seem reasonable, with successful fitting parts for each, the latter one appearing perhaps somewhat better, yet not decisively. Stepping to fittings based on the inclusion of all three types of signals, with more fitting parameters, were not of much help either in achieving a conclusive result. So, it turned out that this kind of best fitting approach to ESR spectrum did not prove fruitful in distinguishing between the occurring signals, and the presence or absence of one or the other type couldn't be confirmed of disproved using this routine. Clearly, any progress here has to come from experiment. However, while not perfect, what the fittings so far do bear out, as a first main result, is the occurrence of at least one P_b-type center.

Thus, to improve on this, ESR experiments were extended in two ways: (1) Low temperature X and Q-band observations; (2) In addition to first harmonic detection, out of phase second harmonic measurements under signal saturation conditions (saturation spectroscopy). Although, dependent on specific signal properties (relative g values, dominant line broadening mechanism, signal shape, etc.), the potential benefit for disentanglement of overlapping signals from ESR observations at different observational frequency is obvious; it may further add to the reliability of signal defect identification. As to the high-power second harmonic

spectra, these are known, under appropriate experimental conditions, to resemble direct absorption shapes (χ"), as empirically evidenced [14]. So, peak maxima here would correspond to the zero crossing g values of the regular $dP_\mu dB$ spectra.

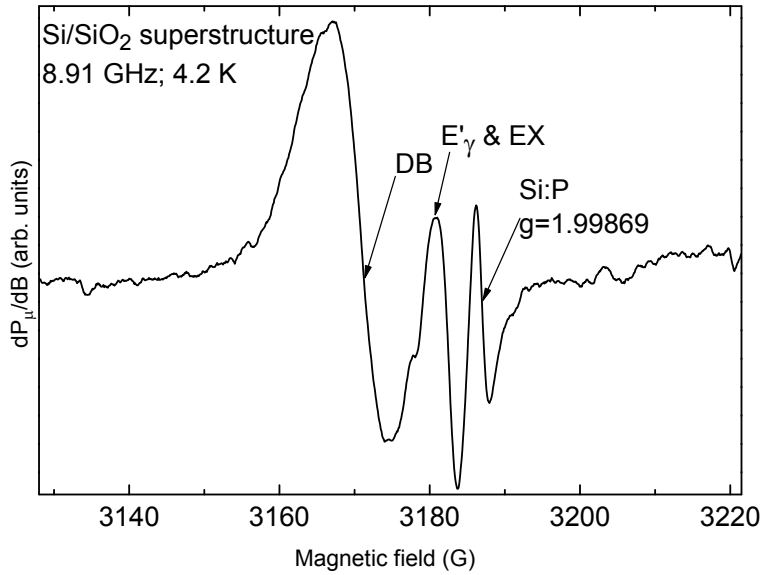

Figure 2.4: First derivative X-band (8.91 GHz) spectrum measured on a phase separated SiO/SiO_2 superstructure at 4.2 K using $P_\mu = 3.95 \times 10^{-7}$ W subjected to VUV irradiation (sample 1e). The DB response appears as a single, rather featureless, signal, indicating the limited appropriateness of lower frequency observations regarding signal discrimination (cf. Fig. 1).

The result of lowering the observational frequency is illustrated in Fig. 2.4. Here, is shown a representative conventional X-band dP_μ/dB spectrum observed on sample 1e, which may be compared with the similarly observed K-band result (see Fig. 2.5(e)). Apart from the main DB feature, we see the appearance of two more signals, i.e., E'_γ and EX, which will be addressed later. Clearly, with respect to (DB) signal resolution enhancement, X-band observations provide no progress. More hope then was put in Q-band observations. However, particular limitations of the Q-band spectrometer (i.e., operational reduction of P_μ), in combination with sample losses, prevented us to obtain correct undistorted first harmonic spectra at low T. However, at the rescue, second harmonic saturation spectroscopy, exploiting the high (differing) saturability of the various ESR signals at low T appeared more successful. For such spectroscopy, the applied P_μ has to be high (enough) in order to saturate the signals to appropriate levels. It is important to note that this method appears reliable only to obtain the "position" (g value) of the signals and, likely, lineshape. Not, however, for inference of the signal intensities, not even in a

relative comparison because different signals exhibit different saturation properties, the precise effect of which on signal response appears less transparent. The different saturation levels are depicted in Fig. 2.6, where we can finally distinguish the signals constituting feature DB.

Figure 2.6 shows a typical out-of-phase high power second harmonic signal observed on sample 1e, finally enabling to discriminate the signals contributing to the DB feature. Apart from the Si:P marker signal, four absorption type signals may be discerned. These include the readily assigned E'_γ and EX signals (at g_c =2.00055 and 2.0025, respectively), and two more prominent, broader signals characterized by g_c =2.007 and 2.0045, respectively, which values correspond to the zero crossing g_c values of the P_{b0} and P_{b1} powder patterns. There is no evidence for the presence of a D signal at g_c ∼2.0055, allowing us to conclude that, on ESR grounds, the Si np's are predominantly crystalline, delimited by (100), (110) or (111)Si/SiO_2 interfaces (and possibly others, as P_b-type centers might occur as well at other c-Si/SiO_2 interface types, but, as to ESR, this remains so far unexplored). The DB signals appear to be majorly, if not solely, composed of $P_{b(0)}$ and P_{b1} powder pattern signals, in accord with what was already suggested by the successful fitting (doted curve) illustrated in Fig. 2.3. In addition, if there would also occur some amorphous (disordered) np's, their number remains below the, albeit rather impressive, detection limit –so the occurrence is disregarded. This provides first firm ESR evidence for the crystalline state of the majority of the Si-np's, in compliance with previous inference [197, 215]. Accordingly, we shall henceforth refer to nc-Si particles.

2.2.7 Results: irradiation treatments and ageing

Having succeeded in tracing the DB signal composition as originating from P_b-type defects at c-Si/SiO_2 interfaces, we can focus on the evolution of this signal, and possibly other appearing ones as well as a function of time and additional treatments (irradiation, annealing). In Fig. 2.5, the evolution of the low-temperature (T= 4.2 K) first harmonic K-band signals is compared for the *as received* sample (a) and after each of the 4 consecutive irradiation steps (cf. Table 2.1), that is: (b) He-Cd lamp with 325 nm output; (c) Xe lamp with an interference filter interposed between the source and the diffusion lens, to deliver light at 362 ± 20 nm; (d) full Xe lamp UV spectrum (180-1000 nm), and (e) VUV Krypton lamp photons with λ ∼123 nm. The evolution of inferred defect densities is histogrammed in Fig. 2.7.

The top panel in Fig. 2.5 shows a K-band spectrum observed on the *as received* sample. When compared to this, the (low power) He-Cd laser irradiation (spectrum (b)) did not ensue any observable effect: the DB response is not affected nor do any additional signals appear. This situation changes after the second illumination treatment (spectrum c; Xe lamp with filter) as the EX signal [124] appears,

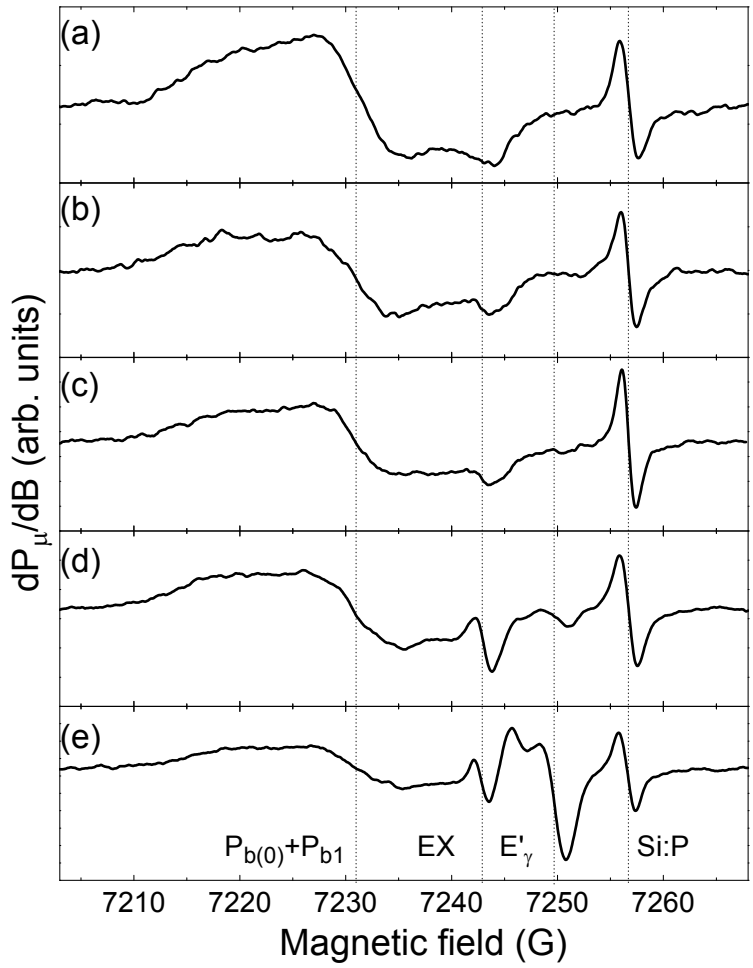

Figure 2.5: Evolution of the first derivative K-band ESR spectra (4.2 K) measured on the phase separated Si/SiO_2 superstructure, under various (photonic) irradiation treatments. Spectrum (a), observed on the as-received sample 1a, is the one presented in Fig. 2.3 and repeated here for the completeness of the comparison. Subsequent spectra are observed after sequential illumination using (b) a He-Cd laser (∼325 nm), (c) a Xe lamp in combination with an interference filter (∼362 nm) or (d) without (full spectrum: 180-1000 nm), and (e) a Kr VUV lamp (∼124 nm). All spectra were measured using $B_m < 1$ G and $P_\mu < 7.9 \times 10^{-10}$ W. Vertical lines mark the zero crossing field values of the various observed signals.

characterized by $g_c = 2.0025$; the DB signals still remains unaffected. After the

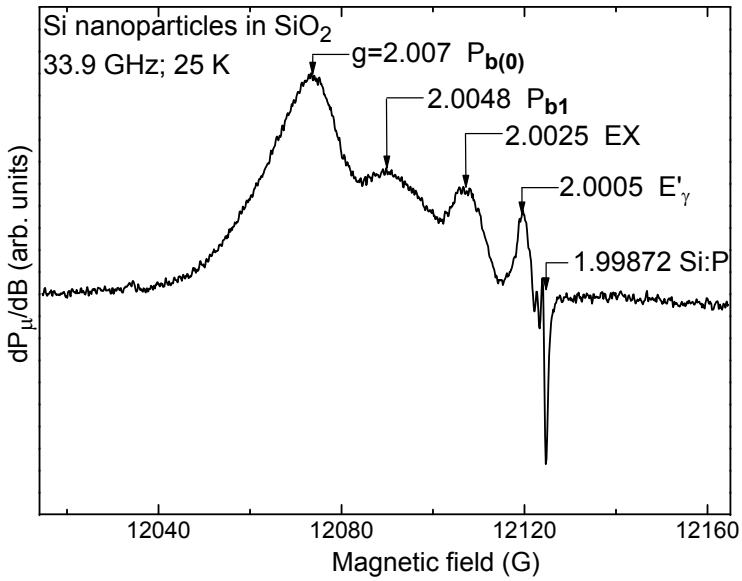

Figure 2.6: High power (saturation) second harmonic out-of-phase Q-band spectrum taken at ∼25 K on a SiO/SiO_2 superstructure subjected to VUV irradiation (sample 1e). The absorption type signals provided by this detection mode, in combination with dissimilar responses to the spectroscopical settings, reveals the various constituent signals in the spectrum as marked by the maximum-absorption g values (corresponding to the respective g_c values in the first harmonic spectra). The spectrometer settings ($B_m = 0.37$ G and $P_\mu = 1.7 \times 10^{-6}$ W) were chosen to optimize resolution of the various spectral components. In particular, the nature of the DB signal (first harmonic detection; see Fig. 2.3) as predominantly composed of $P_{b(0)}$ and P_{b1} components is exposed.

next illumination (full Xe lamp (UV) spectrum), EX increases slightly and one more SiO_2-associated defect appears (spectrum (d)), i.e., the E'_γ defect [39], with its typical double-peak characteristic powder pattern shape, at $g_c = 2.00055$. The next Kr lamp VUV irradiation basically increases this signal (Fig. 2.5(e)), while leaving the other signals unaffected. Both the EX and E'_γ type of defects pertain to the SiO_2 matrix in which the nc-Si are embedded and might thus have been anticipated.

Possible aging effects on the ESR active centers have been checked as well; remeasuring sample 1e about one year after the 'final' VUV treatment, indicated the P_b-type signals to have remained unchanged, regarding both line shape and intensity.

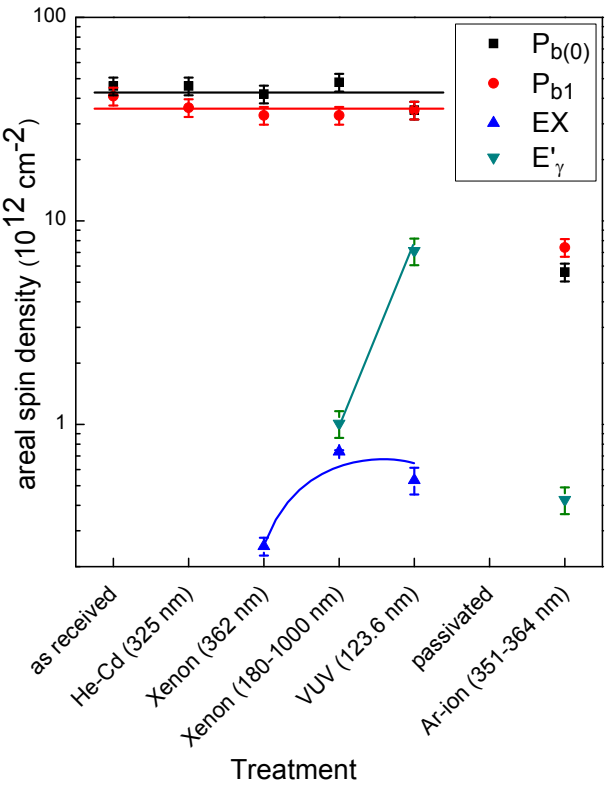

Figure 2.7: Intensity histogram for all paramagnetic defects observed in phase separated SiO/SiO_2 superstructures over the various applied post-manufacturing treatments (photonic irradiations and passivation). The intensities were inferred by use of optimized computer simulations of the separate signals (i.e., $P_{b(0)}$, P_{b1}, E'_γ and EX centers) on undisturbed low power ($P_\mu < 7.9 \times 10^{-10}$ W) first harmonic K-band spectra measured at 4.2 K under equivalent conditions over all sample treatments. Note that for the unpassivated sample (1a-1e) the $P_{b(0)}$ and P_{b1} densities remain constant within experimental error over the different irradiations, indicating the absence of hydrogen at the nc-Si/SiO_2 interfaces. Passivation in H_2 is seen to inactivate all P_b-type defects, and only a fraction of ∼16 % gets reactivated by the Ar-ion laser photons. With respect to the SiO_2-specific defects, the Xe lamp (full spectrum) maximally activates the EX centers, while the E'_γ centers start to appear in the spectrum after the full UV irradiation, and are further enhanced by VUV irradiation. The curves and lines are only meant to guide the eye.

The evolution of inferred areal defect densities over the various post-manufacturing treatments applied is plotted in Fig. 2.7, showing noteworthy aspects: (1) Over the various luminous treatments, the $P_{b(0)}$ and P_{b1} densities remain unchanged within experimental error at the values of $(4.3 \pm 0.2) \times 10^{13}$ and $(3.6 \pm 0.2) \times 10^{13}$ cm^{-2} respectively, giving a fixed total P_b-type defect density of $(7.9 \pm 0.2) \times 10^{13}$ cm^{-2}; (2) EX centers are generated (ESR activated) after the first Xe lamp UV (3.42 eV) irradiation to a density of $(2.5 \pm 0.4) \times 10^{11}$ cm^{-2}, and reaches a maximum value of $(6.3 \pm 1.0) \times 10^{11}$ cm^{-2} after the full UV illumination, to remain unchanged after the VUV treatment; (3) The E'_γ center first appears after the second Xe lamp UV irradiation, at the density of $(1.0 \pm 0.2) \times 10^{12}$ cm^{-2}, but is strongly enhanced by the final VUV irradiation, attaining the value $(7.1 \pm 0.4) \times 10^{12}$ cm^{-2}.

2.2.8 Results: defects and PL measurements

Having achieved identification, localization and quantification of the occurring (intrinsic) paramagnetic defects in the phase separated Si/SiO_2 superstructures, we may find ourselves in an adequate position to evaluate the possible effect of in situ defect generation (ESR activation) during the process of PL measurement itself. As mentioned, for this we have taken four fresh slices (2×9 mm^2 each) from the same part of the wafer as the first sample was taken from. In a first step, this sample was subjected to H passivation to ESR-silence all defects. This appeared very efficient, as evidenced by K-band ESR spectrum shown in Fig. 2.8(a), indicating no ESR signal being left. Then, the sample was placed in front of a defocused Ar-ion laser beam, usually used for PL measurements, for 330 h, after which the ESR spectrum, shown in Fig. 2.8 (b) was taken. Clearly, same P_b-type centers were reactivated, albeit in substantially less quantities than initially observed in the as-fabricated sample; the inferred reactivated density was $(5.6 \pm 0.7) \times 10^{12}$ cm^{-2} and $(7.4 \pm 0.4) \times 10^{12}$ cm^{-2} for $P_{b(0)}$ and P_{b1} signals respectively. Such reactivation of P_b-type centers may not come as a surprise. Indeed, once created, a P_b-type center exhibits fully reversible hydrogen passivation-depassivation kinetics [64]. Beside P_b's, E'_γ defects got activated to a density of $(4.3 \pm 0.4) \times 10^{11}$ cm^{-2} –more than one order of magnitude smaller than the maximum revealed by VUV. No EX defects could be traced within experimental accuracy.

Magneto-PL experiments were performed on the samples both in the as-crystallized, passivated, and depassivated state, as detailed by Godefroo et al. in Ref. [207]. The technique consists, principally, of placing the sample in a variable magnetic field between 0 and 50 T while the sample is kept at 85 K. The PL emission is recorded and the center of mass of the PL peak is plotted against the magnetic field value as shown in Fig. 2.9. Graphs (a) and (c) are obtained on the samples in which defects are ESR active (paramagnetic), while (b) is taken for the sample passivated by H. A clear parabolic field dependence, such as exposed in graph (b), is characteristic of

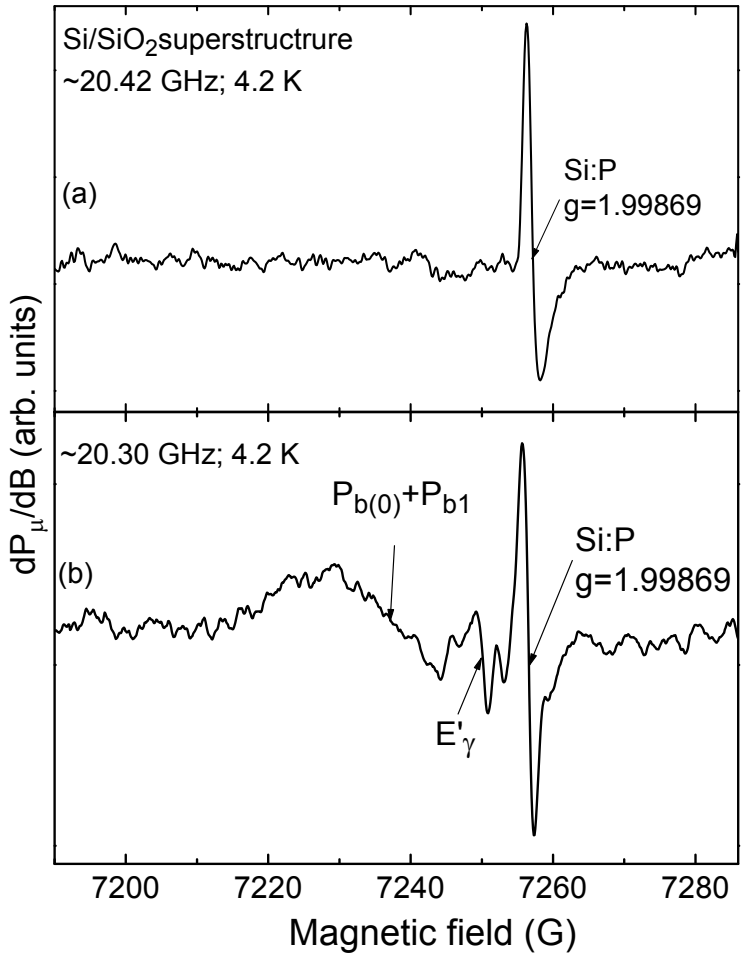

Figure 2.8: First harmonic K-band ESR spectra observed under similar spectroscopical settings ($P_\mu < 7.9 \times 10^{-10}$ W, $B_m = 0.8$ G) on sample 2, subjected to (a) passivation in H_2 (1 atm; 405 °C) and after subsequent Ar-ion laser irradiation (351-364 nm) for 330 h. The latter step is seen to partly reactivate the $P_{b(0)}$, P_{b1} and E'_γ signals; all are inactivated after the first step (a).

PL from a state that is quantum confined by the nanocrystal, whereas no detectable field dependence indicates that a very highly localized (defect) state is responsible for the PL (a and c) [207]. This investigation clearly shows how a system can be switched from defect to quantum confinement originated PL and back.

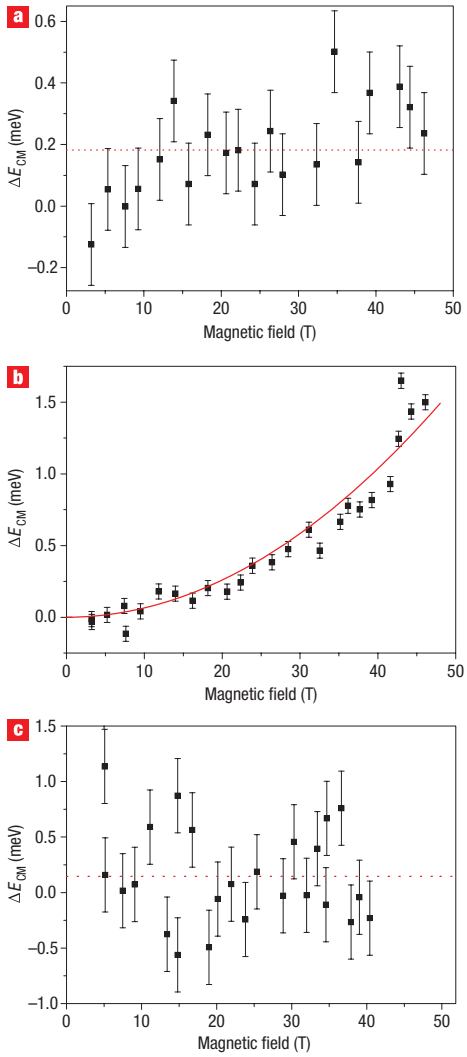

Figure 2.9: Shift of the center of mass of the PL peak (ΔE_{CM})as a function of externally applied magnetic field, measured at 85 K [207]. (a) As-crystallized sample; The dotted line indicates the mean value of the measured points. (b) Passivated sample. The solid line, showing a parabolic fit, indicates the quantum confinement origin of the PL. (c) Sample partially depassivated by the Ar-ion laser UV irradiation (351-364 nm). The dotted line indicates the mean value of the measured data [207].

2.2.9 Analysis and discussion

As outlined, the investigated system is comprised of nc-Si particles about 2 nm across, yet somewhat enlarged laterally, embedded in a SiO_2 matrix, whose particles have formed during the high-T phase separation treatment within the 37 layers of deposited SiO, interspaced by 4 nm thick layers of SiO_2. The ultimate inter-core distance of the formed Si-np's is determined by the stoichiometry of the initial SiO_x layer [211] –SiO in this case– and the attained size of the nanocrystals, at least on the direction perpendicular to the layers, is in close connection with the initial thickness of this SiO layer. On the basis of the studied properties of the composing materials, but at microscopic size, such Si/SiO_2 nanostructures may be anticipated to exhibit point defects. For one, unless properties on the nanoscale would differ drastically from those at the macroscopic one, the Si/SiO_2 interfaces must exhibit their inherent 3-fold coordinated Si defects resulting from the lattice/network mismatch between the two materials. And indeed, as turns out from the current ESR study, in combination with appropriate defect activation treatment, the system appears beset with point defects. It has been a main goal of this work to typify (identify) the occurring defects, determine densities, and infer the location of these with particular parts of the heterogeneous superstructure. Four types of defects could be isolated, i.e., the $P_{b(0)}$ and P_{b1} Si/SiO_2 interface defects, and the SiO_2-associated E' and EX defects. According to the current atomic understanding, all these concern intrinsic point defects. While point defects are generally highly unwanted for aimed technological applications, in converse, such defects may well serve as very local probes of utmost (atomic) sensitivity, where the structural environment is sensed through the spatial extend of the unpaired electron orbital. It is a basic attribute of the magnetic resonance technique. We may now address the information potential provided by each of these defects concerning the superstructure.

For clarity, it needs to be remarked that these, by nature of detection, only concern ESR-active centers, which number will represent an underbound of all present. There likely are still present other types of defects, either ESR-inactive or only occurring in densities insufficient to enable successful ESR detection.

2.2.10 Analysis and discussion: interface defects

We first may address the predominant (Si) DB signal, ascribed (generically) to $Si_3 \equiv Si^{\bullet}$ type defects. At least five results stand out:

1. As outlined, by virtue of the combination of (several) observational frequencies and detection modes, this DB signal has been quite reliably disentangled as being composed of an overlap of $P_{b(0)}$ and P_{b1} powder patterns. For clarity, here it should be added that the P_b and P_{b0} centers at microscopic Si/SiO_2

interfaces, basically being identical defects of axial symmetry, generally do show some (weak) differences in principal g values (and in signal shape properties as well), the kind of overlap did not enable us to attain any discriminative conclusion on this level. So, if both types of defects would occur, the corresponding signals, rather than attempting fitting two, have been united into one powder pattern. This inability to discriminate may appear unfortunate as to drawing potentially useful conclusions afterwards as the P_b and P_{b0} centers, at least for the microscopic case, do pertain to crystallographically different interfaces, i.e., (111)Si/SiO_2 and (100)Si/SiO_2, respectively. A particularly noteworthy result of the signal disentanglement is the conclusion of absence of the D center, at least within experimental accuracy. Based on the known properties of a-Si, where D centers are abounding, it indicates the major part of the n-Si particles, if not all, to be highly crystalline, well in compliance with previous conclusion from HRTEM and soft x-ray spectroscopy [216] studies. It constitutes the first solid ESR evidence on this matter.

2. The fact that the uncovered $P_{b(0)}$ and P_{b1} signals appear as powder patterns, rather than anisotropic multi-branched ESR spectra, indisputably indicates the nc-Si particles to be randomly oriented, i.e., not crystallographically in registry, thus appearing as a "powder" of nc particles. Given the kind of preparation method, with no crystallographic 'seeding' element present, this conclusion perhaps does not come as a surprise. (This differs from the "reverse" method of c-Si-particles-in-SiO_2 formation, as e.g. in the separation by implantation of oxygen [217] (SIMOX) method, where c-Si islands are formed in the buried oxide through oxygen implantation of a c-Si substrate).

3. In this respect, one more finding is that within experimental accuracy, no anisotropic (φ_B dependent) spectra are observed. This would tell us that we cannot discern against the "background" of isotropic signals the anisotropic P_b-type signals undoubtedly present at the microscopic c-Si substrate/SiO_2 interface, viz. each defect occurring in densities of $\sim 1 \times 10^{12}$ cm^{-2} in standard thermal [30] (100)Si/SiO_2. But as these values would give for our sample area a total number of $\sim 0.7 \times 10^{12}$ cm^{-2} for each defect type, that is less than 1% of the actual number involved in the inferred $P_{b(0)}$, P_{b1} powder patterns, resolving these signals may not be feasible. Reassuringly, it further affirms the observed P_b-type defects to pertain to the nc-Si/SiO_2 interfaces.

4. In passing, the data also provide one more conclusion on the possible involvement of H in the superstructure. As shown in Fig. 2.5, the number of $P_{b(0)}$ and P_{b1} centers stays constant within experimental error (± 30 %), both in total number and relative ratio (summing to a total density of $\sim 7.8 \times 10^{13}$ cm^{-2}). Over the various photonic treatments applied, including a final VUV irradiation, known to be efficient in depassivating the preexisting defects that might have rendered inactive (hydrogen passivated) during the

fabrication process, the constant values indicate that no P_b-type defects had been left H-passivated in the as-received sample as might have been expected from the final high-T phase separation anneal in pure N_2, viz. thermal H removal in an N_2 ambient sufficiently lain in H-related species.

5. Further focusing in, we may attempt to assess what information the disclosed P_b-type defect spectra may provide about the nc-Si particles properties. Provided that our broad knowledge of the microscopic Si/SiO_2 system can be transferred down to the nanoscale, i.e., the nc-Si/SiO_2, we may arrive at some tentative conclusions. A first one concerns the shape of the nc-Si particles. Established as being (mono) crystalline, the Si nanocrystals are likely bordered by a mix of (nanosized) facets of c-Si planes, e.g., (100), (110), (111), etc. Previous HRTEM investigations [197] have evidenced (at least part of) the Si particles to be crystalline in a spherical like shape, yet with however no further information on the particles' precise morphology. This though may be of fundamental interest. In such embedded case, where c-Si particles grow through thermally stimulated atomic agglomeration (diffusion) amid an a-SiO_xO_{2-x} (x $\leq$ 1) matrix, such as in the current case of the layered SiO/SiO_2 superstructure approach, or after Si implantation in an SiO_2 matrix (see, e.g., Cheylan et al. [218]), it is not a priori known what would be the ultimate naturally determined bordering morphology of the growing Si nanocrystals. It has raised substantial theoretical interest within the nanoscience world [219, 220]. Likely, it will entail a net lowest entropy compromise between an intricate mix of influential factors encompassing local strain, surface tension, crystal energy (i.e., the particles do not grow amorphous), bond strengths and lengths, and particle size.

The influence of strain may be drastic. As possible root causes for strain, there is the difference in thermal expansion coefficients of Si and SiO_2, the volume shrinkage (molar volume ratio of SiO_2 to Si of $\sim$2.2) associated with the transformation of an a-SiOx region into denser c-Si, and changing surface/volume ratio with varying nc size.

From the above analysis, we have concluded the observation of the $P_{b(0)}$, P_{b1} interface centers, with no evidence for a D signal. Occurrence of only P_{b0} and P_{b1} defects would, in a plane "bulk" reasoning, hint at predominantly (solely) (100) faceted nanocrystals. But, as outlined, since the data did not enable making a more in depth distinction between P_b and P_{b0} signals (the spectra at the microscopic (100) and (111) planes appearing largely identical), the objective conclusion should rather entail the occurrence of all three types of P_b centers (P_b, P_{b0}, P_{b1}). So, on this basis, a first order inference would be the Si nanocrystals to be bordered by a mix of the low index (100) and (111) facets. But, as reported [214], since the P_b center signal at the (111), (110) and (100) faces would appear very similar, in an objective attitude one arrives at a mix of all three low index facets (100),

(110), (111). Furthermore, in lack of any information on Si/SiO_2 interface defects for higher index Si planes, we even cannot a priori exclude additional occurrence of these. Likely, however, low index plane will be predominant, as hinted from previous observations (SIMOX). In striving to probe still deeper, we may next, in addition to the *kind* of defects observed, address the observed defect numbers (densities). Again, we use the microscopic Si/SiO_2 case as step stone. Then, if all three low index facets would prevail in equal areal proportions, we would expect a defect ratio $R \equiv [P_{b(0)}]/[P_{b1}] \geq 8$, in contrast with current observations. So, on this basis, the 'equal low index facets occurrence' diagnosis would be incorrect. Instead, the inference R$\sim$1.2 –a well know attribute of the standard microscopic (100)Si/SiO_2 interface [221]- would rather hint at nc-Si particles with a mix of (111), and predominant (100) facets, perhaps as appearing in a [100] truncated (111) Si octahedron, as shown in Fig. 2.10. This, apparently is corroborated by theoretical simulations [192, 208, 219].

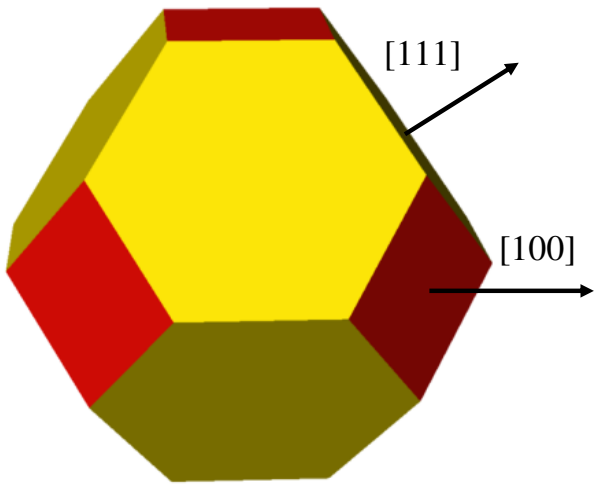

Figure 2.10: Idealized average morphology ([100] truncated (111) octahedron) of embedded nc-Si particles in phase-separated SiO/SiO_2 entities as inferred from the occurring $P_{b(0)}$ and P_{b1} (Si/SiO_2) interface defects, based on microscopic defect properties.

But again, it should be cautioned that the above inferences draw on the assumption that microscopic properties may be carried over to the nanosize, an at least questionable approach. We must be aware of a potential drastically different behavior. For one, at the nanoscale, it might well be that the incorporation (generation) of the P_{b1} defect does not require such situation as a real (100)Si/SiO_2

facet. The defect, viewed as a defected Si dimer [30, 66], might grow in from a totally different angle. The occurrence of a relatively high density of P_{b1} type centers may be related, given the envisioned atomic nature of the defect [30], to an enhanced density of step edges at bordering facets. In this respect, we should also point to the distinctly different realization of the Si/SiO_2 interface, i.e., nc-Si particles grown from inside out within an existing SiO_x matrix, in a sense opposite to the standard procedure of (thermal) oxidation of c-Si. Circumstances differ.

Further assessing the quality of the interface, we may calculate the P_b-type defect density per effective nc-Si particle (interface) area. For nc-Si particles of $\sim$2 nm across (in average) and taking into account that the revealed P_b-type defects exclusively pertain to the nc-Si/SiO_2 interfaces, we obtain an effective areal density of $\sim(2.5 - 4.7) \times 10^{12}$ cm^{-2} assuming spherical or prolate spheroid shaped particles (compressed spheres along the sample normal $\overrightarrow{n}$), respectively. This value is comprised within the range $(2 - 5) \times 10^{12}$ cm^{-2} of naturally inherent defects characteristic for the standard quality thermally grown interfaces. If not purely coincidental, it could indicate the interfaces of both systems to be comparable, i.e., that the microscopic Si/SiO_2 interface properties are retained down to the nanoscale, at least regarding occurring intrinsic interface defects. Then c-Si particles diameters of $\geq$ 2 nm would suffice to realize such properties. But again, we should be extremely cautious about the actual density of interface defects to be expected.

For the given Si particle density, we find a P_b-type defect for every $\sim$1.4 nc-Si particle –*close to about one defect per particle*. Here, within the view that P_b-type centers are incorporated in adopting c-Si/a-SiO_2 interfacial mismatch, one may then wonder, for similar particles, why not occurring one such defect for each particle, should the one-defect occurrence be the adaptation norm? Probably not so, for various possible reasons, such as statistical variations in particle size, morphology, and purity. Moreover, adding to the complexity of such consideration, one should also recall that the true particle size in the current nanostructures may not be so uniquely defined, cf., in relationship with the 'inevitable' presence of a non-stoichiometric (suboxide) transition intermediate ('reactive') layer [222] between the c-Si core and surrounding SiO_2, as also well known from the macroscopic case; The interface is not atomically abrupt [216]. Interestingly, given this finding, the nc-Si particles system appears as divided in two about equal parts, i.e., one composed of nanocrystallites with an interface relaxing interface defect, the other part without. As the Si DB type defects were found to be highly efficient in quenching of PL above 1.1 eV [223, 224], it would leave this system PL inactive. Indeed, in related work, this has been exquisitely demonstrated though inactivation of the Si DB centers, resulting in unequivocal demonstration of quantum confinement (QC) determined PL from high-magnetic field magneto-PL measurements [207]. In fact, through repeated activation and inactivation of the P_b-type interface centers, the origin of PL could be reversibly switched between QC and defect determined. Without elimination of the P_b defect system, no QC determined PL could be revealed. Such

inverse correlation between the density of active P_b-type defect centers and PL has been observed before [225].

2.2.11 Analysis and discussion: SiO_2 associated defects

Upon photonic irradiation, two types of SiO_2-associated defects are ESR activated. First appears the EX defect after ∼362 nm (filtered Xe lamp) irradiation, with density of (2.5 ± 0.4) × 10^{11} cm^{-2}, increasing to (6.3 ± 0.4) × 10^{11} cm^{-2} (corresponding to a volumetric value of [EX] = (4.1 ± 0.6) × 10^{16} cm^{-3}) after further full spectrum Xe lamp irradiation, to remain constant after subsequent VUV illumination. The presence of EX centers, albeit in rather low intensity, may be indicative for a somewhat lower quality of the ultimate $SiO_{2(x)}$ matrix, which may be linked with the kind of deposition or phase separation annealing procedures applied. So far, nothing is known about the (impact on) PL or optical activity of these centers. Yet, electrically, it has been inferred these to be in the positive charge state when ESR active [226], so because of the charge trapping nature, their presence may play a role.

After VUV irradiation, the E'_γ center reaches a maximum density of ∼(7.1 ± 0.6) × 10^{12} cm^{-2}. The center, identified as an unpaired electron at a 3-fold coordinated Si (generic entity $O_3 \equiv Si^\bullet$), may thus be taken as a measure for the presence of oxygen-vacancies, or at least, oxygen deficiency of the SiO_2 matrix -a quality label in that sense. In thermal a-SiO_2, it has been concluded the center to be in the neutral charge state when ESR active [99]. From the successive irradiation treatments we may conclude that EX center is easier activated, at lower photon energy than E'_γ, reaching its maximum density after the full spectrum Xe lamp irradiation while the latter defect becomes just observable in the spectrum. The upper limit of the activation for the E'_γ centers is reached after VUV irradiation, i.e., related to substantial increase in hν, not the exposure time as it can be seen from Table 2.1. Volumetrically, based on the estimated amount of SiO_2, the observed E'_γ density corresponds to $[E'_\gamma] \simeq (4.6 \pm 0.3) \times 10^{17}$ cm^{-3} of SiO_2, which may be compared with the value of ∼3 × 10^{17} cm^{-3} found for the standard thin thermal SiO_2 on Si after exhaustive VUV irradiation [103]. Assuming 10 min VUV irradiation to activate the E'_γ centers in this structure exhaustively, this would indicate the quality of the current SiO_2 matrix reaching that of standard thermal SiO_2.

2.2.12 Analysis and discussion: reactivation of defects

The importance of hydrogen passivation of defects in Si, SiO_2, and at Si/SiO_2 interfaces has long been proven [52, 57, 227, 228] and used in the fabrication process of CMOS transistors for example. There are also reports on the beneficial influence

of the passivation on PL [229]. The beneficial impact of the hydrogen-passivation treatments (400 °C; 30 min; 1 atm H_2) is immediately clear from Fig. 2.8(a), where it seems that all ESR-active signals have disappeared. We applied the treatment to our sample with the aim of "eliminating" the defects, thus creating a virgin sample to enable evaluation of the potential (perturbing) influence that the PL measurement may have by itself (photonic impact) on defect activation, i.e., what kind of defects might be (re-activated) by the Ar-ion laser used to perform PL measurements. As illustrated in Fig. 2.8 (b), we observe reactivation of both $P_{b(0)}$ and P_{b1} centers. While comparable, P_{b1} centers appear to be reactivated slightly faster. One explanation may be that the irradiation tends to reactivate faster entities that are more strained. Summing the two intensities, we obtain one P_b-type defect every 8.6 Si-nc. So, applying the equivalent of a photon dosis used in a standard PL measurement seems to activate only a fraction ($\sim$0.16) from the pre-existing P_b-type defects. The total number of Si/SiO_2 interface centers activated by the equivalent of the photon irradiation applied during one day of PL measurement reaches only about one sixth of the fraction of c-Si particles with an initial P_b-type defect. The exciting (instrumental) irradiation will weakly distort the PL results, yet not substantially.

2.2.13 Conclusions

The current multifrequency ESR study has addressed inherent point defects in phase separated Si/SiO_2 superstructures with embedded Si nanocrystallites ($\sim$2 nm across). The occurrence of four types of paramagnetic defects, i.e., $P_{b(0)}$, P_{b1}, E'_γ, and EX, has been delineated.

For the as-manufactured sample state, a main result is that the principle Si DB signal has been found to be composed of overlapping powder patterns of $P_{b(0)}$ and P_{b1} Si/SiO_2 interface-specific defects, pertaining to the nc-Si/SiO_2 interfaces. The absence of a D signal provides independent ESR evidence for most part, if not all, of the Si particles to be crystalline, which occur randomly oriented. Assuming that the known properties of the standard thermal microscopic Si/SiO_2 interfaces may be transferred down to the nanoscale, the specific signatures of the revealed $P_{b(0)}/P_{b1}$ systems would comply morphologically with the nc-Si particles, in average, being principally bordered by (111) and (100) facets as, e.g., in a [100] truncated (111) octahedron, in compliance with theoretical modeling.

This P_b-type system density remains unchanged under subsequent various UV/VUV irradiations for substantial times, indicating an inherent defect system with no involvement of H passivation, as might have been expected from samples prepared without (deliberate) presence of H, subjected to the final high-T phase separating anneal in N_2 at 1100 °C.

Disregarding the occurrence of more than one defect at a Si nanocrystal, we find about one P_b-type defect every 1.4 Si particles, indicating the nc-Si system to be comprised of two subsystems, one with and one without having incorporated a strain relaxing P_b-type defect -the latter within the view, as generally adopted for the macroscopic Si/SiO_2 system, that P_b-type centers are introduced to account for interface lattice (c-Si)/network (a-SiO_2) mismatch. For as far as paramagnetic defects may affect physical properties, rather ubiquitous in fact, this will have repercussions for experimental response, e.g., PL behavior, where the current quantification by ESR may appear much useful. Given the known PL quenching properties of Si DB type defects in general, we are left with two subsystems with drastically different PL behavior, as has indeed been demonstrated elsewhere.

In addition to qualitative aspects, the absolute density of P_b-type defects per effective nc-Si (interface) area is found right in the range of standard microscopic Si/SiO_2 entities. It bears out the encountered nc-Si interfaces to be of standard thermal (high) quality, meaning that even with growing the Si nanocrystallites from within the SiO_2 environment one ends up with an interface quality competing with the best of the classical macroscopic growing techniques –probably not a straightforward matter given the totally 'opposite' ways of Si/SiO_2 growth. Intriguingly, the P_b-type defects evolve in the same fashion. It seems to underscore the *universality* of the P_b-type centers as archetypical Si/SiO_2 interface defects unavoidably inherently connected with the natural Si/SiO_2 mismatch, which needs to be incorporated in theoretical modeling. Thus as it is not the case for the classical thermal Si/SiO_2 entity, there neither in the current nc-Si/SiO_2 case does there exist a 'magic' recipe to realize a P_b-type defect lain Si/SiO_2 interface. And if no post formation action is taken (i.e., inactivation), these will show up as detrimental unpaired-spin defects.

After UV/VUV irradiation, two SiO_2-associated defects, i.e., E'_γ and EX, have been resolved. Based on the measured exhaustive volume densities of E'_γ, the attained quality of the Si oxide in the superstructure would match that of standard thermal SiO_2 on Si –quite remarkable, indeed. So, all together, the unveiled properties of the inherent paramagnetic point defects, serving as atomic probes, point to (top) standard quality of the inner nc-Si/SiO_2 interfaces as well as the SiO_2 matrix. Thus, as to the control of inherent point defects (detrimental charge traps), it may be hard to still improve on this nc-Si-in-SiO_2 structure.

The EX centers, typically observed in densities one order of magnitude less than E'_γ, are ESR-activated at lower photon energy than E'_γ. Since its atomic attributes are less well known, the relevance of the EX center, concluded to be in the positive charge state when ESR-active, to the oxide quality is less clear. But overall the defects seem to play an inferior role.

In combination with exhaustive H passivation treatments, the photon excitation (Ar-ion laser) applied in PL measurements is observed to (re)activate paramagnetic

defects, i.e, P_b-type and E'_γ centers. Though the activation appears weak in terms of defect fractions, the phenomenon should urge caution in performing extensive PL measurements as it may in situ obfuscate results. The affect is not unexpected as UV/VUV ESR-activation of (preexisting) defects excitation in a-SiO_2 and Si/SiO_2 systems is long known.

2.3 Annealing ambient influence on paramagnetic centers: P_{b0} point defect at the origin of PL quenching

2.3.1 Introduction

In the first section of this chapter, the result of a first in depth ESR investigation on layered nc-Si embedded in a-SiO_2 obtained by the superstructure approach (annealing of SiO_x/SiO_2 bi-layers stacks) have been presented. As one inference, we concluded that point defects inherent to the structure are quenching quantum confinement PL, yet no further specification has been attained as to which type of defect is causing this. This will be addressed into more detail in this second part of ESR research.

The superstructure technique is offering a good nc size and density control by independently changing deposition parameters like SiO_x layers thickness or stoichiometry, minimizing the influence on PL of defects and variations in nc-Si size, thus facilitating the discrimination process.

It has been shown that the annealing ambient is affecting [149, 230] the PL observed from nc-Si/SiO_2 structures in the sense that the growth of the Si nc's is restricted in the case of N_2 compared to Ar annealing. To understand the mechanism, we are here analyzing ESR measurements on a wide number of samples (annealed in N_2 or Ar) and the results are combined with the conclusions drawn from PL measurements on physically the same samples, this in an attempt to find out how the annealing ambient is affecting the attained superstructure and thus get better understanding about which defects influence PL.

2.3.2 Experimental details: sample preparation

All samples were deposited (single side) on 150-μm thick p-type (100)Si wafers cleaned initially by piranha (H_2SO_4:H_2O_2 mixture for 10 min at 70 °C) and HF (1 % HF in H_2O) solutions. Three sample sets were prepared using the superstructure approach as described in more detail in Sect. 2.2.2. In the current case, SiO powder

was evaporated either under high vacuum ($<1 \times 10^{-6}$ mbar) or O_2 pressure ($\approx 8 \times 10^{-4}$ mbar). On two Si wafers 50 SiO/SiO_2 bi-layers were grown with thicknesses of 2 nm/4 nm (sample A2) and 5 nm/4 nm (sample A5), respectively, while on a third substrate one 300-nm thick SiO layer was evaporated to produce a control sample, named B for convenience. For the layered samples the estimated total thickness of the SiO layers is 100 and 250 nm, respectively, values lower than the compact SiO layer thickness. All three samples were capped with a 10 nm a-SiO_2 layer to avoid the evaporation during high-T annealing of some top layers as it happened for the sample described in Sect. 2.2.3. Each of the three wafers were cut in two, one half being annealed in Ar and the other half in N_2 ambient at 1100 °C for 1h (gas purity > 99.9999 % obtained with additional point-of-use purification) in a quartz tube furnace equipped with a turbomolecular pump and electrically controlled pressure regulation. The annealed samples got "Ar" or "N_2" added to their labels.

To increase sensitivity by of the ESR measurements on passivated samples, a 75 μm thick p-type (100)Si wafer was used as substrate for the deposition on *each* side of 45 SiO_x/SiO_2 bi-layers 3 and 4 nm thick, respectively, thus enabling us to increase the volume of the superstructure fitted in the cavity. The sample was labeled A3. Rutherford backscattering measurements on similar samples fabricated using the same pressure parameters indicate the stoichiometry of the SiO_x layer to be $x = 1.2$ [231]. A 10-nm SiO_2 capping layer was deposited over the superstructure to avoid partial sample evaporation during high temperature annealing. The wafer was cut in two, one piece annealed in N_2 and the other in Ar (labeled A3N_2 and A3Ar, respectively). Those samples were to be used for determining by ESR low density impurities incorporated in the structure, thus, much attention was payed to the purity of materials used in the process. The furnace tube was evacuated to 1×10^{-6} mbar prior to establish a N_2 or Ar gas flow of 50 sccm at a constant pressure of 1050 mbar. The leak rate in the system was measured to be negligible ($\sim 10^{-5}$ mbar l s^{-1}) and the purity of the gases is better than 99.9999 %. So, we have obtained two thin samples ($\sim$75 μm) labeled A3N_2 and A3Ar.

2.3.3 Experimental details: post manufacturing treatments

The samples A2, A5 and B annealed either in Ar or N_2 were cut again in half, one piece of each type being additionally annealed in forming gas (5 % H_2 in N_2) for 1 h at 500 °C, now "FG" being added to their label. Following this procedure 12 samples have been produced at IMTEK, Germany, by varying three parameters: initial SiO layer thickness (influences c-Si size after annealing), annealing ambient and passivation of the structures.

The sample A5ArFG was additionally passivated in this laboratory in H_2 ambient at 410 °C for 45 min to check whether the passivation in FG can be improved

("H_2" was added to the label).

Samples $A5N_2$ and A5Ar were subjected to VUV irradiation (adding also "VUV" to their label) emitted by a krypton resonance discharge lamp (10.02 eV; see Sect. 2.2.5) for 15 min to maximally activate defects.

Half of sample $A3N_2$ and half of A3Ar were annealed in pure H_2 ambient at 450 °C for 1 h to passivate the intrinsic point defects present in the structure as seen in sect. 2.2.8 ("H_2" was added to the sample label).

For ESR measurements the quarter wafers were cut in slices of 2×9 mm^2. A typical ESR sample is obtained by stacking ∼12 slices (total area ~ 2 cm^2) in the case of samples A2, A5, and B, and ∼20 slices (both sides; ~ 7 cm^2) from sample A3. The parts with the superstructure on were protectively covered, after which the cutting damage was removed by wet chemical etching (CP4). Dipping in aqueous HF solution was carried out before each measurement to remove any SiO_2 grown on Si when kept in room ambient.

2.3.4 Experimental details: ESR spectroscopy

To assess the paramagnetic point defects present in the samples A2, A3, A5 and B and their derivates described above, extensive low temperature (4.2 K) ESR studies were carried out using the K-band spectrometer (highest sensitivity and stability for low-T measurements), usually driven in the adiabatic absorption mode. Conventional low-power first derivative-absorption dP_μ/dB spectra was obtained applying $B_m \leq 0.5$ G and $P_\mu \sim (0.7 - 4) \times 10^{-8}$ mW, properly adapted to avoid any noticeable signal distortion. The paramagnetic point defects have been calibrated against a co-mounted Si:P marker for determination of densities and g values. The attained absolute and relative accuracies are estimated to be ∼20 % and ∼10 %, respectively and ~ 0.00005 for g value determination.

2.3.5 Paramagnetic point defects

K-band ESR spectrometry was used to investigate the eight as-annealed samples (A2, A3, A5 and B thermally treated in N_2 or Ar) at 4.2 K. A representative spectrum observed at 4.2 K on sample $A5N_2$ is shown in Fig. 2.11. Three types of point defects are observed in all the as-annealed samples: $P_{b(0)}$, P_{b1} and EX. All three have been introduced in Chap. 1, and their presence in the superstructure type samples has been extensively discussed in sections 2.2.6 and 2.2.10. The inferred defect densities for the samples studied in the current section are compiled in Table 2.3.

Table 2.3: The densities of point defects observed by ESR in nc-Si/SiO_2 superstructures. The listed values are the defect densities divided by the Si substrate surface (cm^2 *units*). It should be noted that in the case of samples A5 and A2, 50 bi-layers were initially deposited while it were 45 bi-layers in the case of sample A3. Defect densities for samples A3 are given per superstructure side.

Sample code	$[P_{b(0)}]$ (cm^{-2})	$[P_{b1}]$ (cm^{-2})	[EX] (cm^{-2})	[K] (cm^{-2})	$[E'_\gamma]$ (cm^{-2})
$A2N_2$	$(3.9 \pm 0.2) \times 10^{13}$	$(3.7 \pm 0.1) \times 10^{13}$	$(2.8 \pm 0.1) \times 10^{12}$		
$A2N_2FG$	$(3.1 \pm 0.4) \times 10^{12}$	$(3.9 \pm 0.5) \times 10^{12}$	$(1.4 \pm 0.1) \times 10^{12}$	$(4.5 \pm 0.5) \times 10^{12}$	
A2Ar	$(7.7 \pm 0.5) \times 10^{13}$	$(8.0 \pm 0.5) \times 10^{13}$	$(2.2 \pm 0.2) \times 10^{12}$		
A2ArFG	$(1.6 \pm 0.2) \times 10^{12}$	$(2.3 \pm 0.2) \times 10^{12}$	$(6.0 \pm 0.4) \times 10^{11}$	$(1.9 \pm 0.1) \times 10^{12}$	
$A3N_2$	$(4.0 \pm 0.2) \times 10^{13}$	$(2.9 \pm 0.1) \times 10^{13}$	$(4.2 \pm 0.2) \times 10^{12}$		
$A3N_2H_2$	$< 1.0 \times 10^{12}$	$(3.4 \pm 0.1) \times 10^{12}$	$(3.0 \pm 0.2) \times 10^{12}$		
A3Ar	$(8.0 \pm 0.4) \times 10^{13}$	$(5.1 \pm 0.1) \times 10^{13}$	$(1.6 \pm 0.1) \times 10^{12}$		
$A3ArH_2$	$(1.6 \pm 0.1) \times 10^{12}$	$(2.5 \pm 0.1) \times 10^{12}$	$(1.0 \pm 0.1) \times 10^{12}$		
$A5N_2$	$(8.0 \pm 0.1) \times 10^{13}$	$(3.7 \pm 0.2) \times 10^{13}$	$(1.2 \pm 0.1) \times 10^{12}$		
$A5N_2VUV$	$(8.0 \pm 0.3) \times 10^{13}$	$(5.0 \pm 0.1) \times 10^{13}$	$(4.5 \pm 0.3) \times 10^{12}$		$(4.6 \pm 0.2) \times 10^{12}$
$A5N_2FG$	$(3.0 \pm 0.2) \times 10^{12}$	$(6.3 \pm 0.8) \times 10^{12}$	$(1.3 \pm 0.2) \times 10^{12}$	$(3.3 \pm 0.2) \times 10^{12}$	
A5Ar	$(8.4 \pm 0.5) \times 10^{13}$	$(9.1 \pm 0.2) \times 10^{13}$	$(1.6 \pm 0.1) \times 10^{12}$		
A5ArVUV	$(9.6 \pm 0.3) \times 10^{13}$	$(7.5 \pm 0.3) \times 10^{13}$	$(8.1 \pm 0.5) \times 10^{12}$		$(7.9 \pm 0.5) \times 10^{12}$
A5ArFG	$(2.3 \pm 0.3) \times 10^{12}$	$(4.7 \pm 0.3) \times 10^{12}$	$(7.0 \pm 0.7) \times 10^{11}$	$(2.7 \pm 0.4) \times 10^{12}$	
$A5ArFGH_2$	-	$(9.0 \pm 1.0) \times 10^{11}$	$(1.8 \pm 0.2) \times 10^{11}$	$(1.2 \pm 0.2) \times 10^{12}$	
BN_2	$(1.5 \pm 0.1) \times 10^{14}$	$(1.0 \pm 0.1) \times 10^{14}$	$(2.4 \pm 0.2) \times 10^{12}$		
BN_2FG	$(2.0 \pm 0.2) \times 10^{12}$	$(4.6 \pm 0.4) \times 10^{12}$	$(9.5 \pm 0.8) \times 10^{11}$	$(2.4 \pm 0.4) \times 10^{12}$	
BAr	$(1.5 \pm 0.1) \times 10^{14}$	$(1.1 \pm 0.1) \times 10^{14}$	$(1.6 \pm 0.2) \times 10^{12}$		
BArFG	$(1.6 \pm 0.1) \times 10^{12}$	$(4.8 \pm 0.4) \times 10^{12}$	$(9.0 \pm 0.4) \times 10^{11}$	$(3.4 \pm 0.3) \times 10^{12}$	

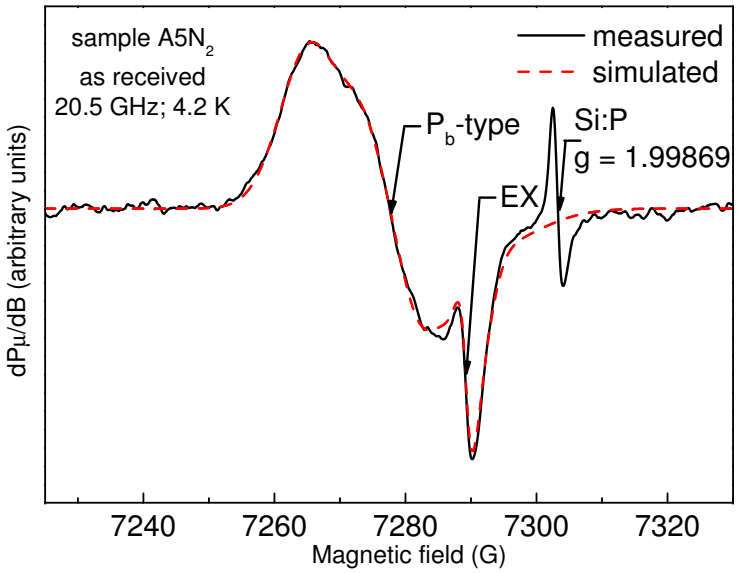

Figure 2.11: First-derivative K-band spectrum observed at 4.2 K on the as received $A5N_2$ sample using $B_m = 0.5$ G and $P_\mu = 4 \times 10^{-8}$ nW, where the latter values are reduced to avoid signal distortion.

The P_b-type centers stem from Si DB's at different crystalline orientations of the c-Si/SiO_2 interfaces. The (111) and (110) Si/SiO_2 interfaces exhibit only one type of paramagnetic defects each, i.e., P_b and P_{b0}, respectively. These are chemically identical with the P_{b0} at the (100)Si/SiO_2 interface ($Si_3{\equiv}Si^\bullet$), yet not entirely structurally. However, in the case of nc-Si particles in SiO_2 where the interfaces are randomly oriented, despite extensive ESR measurements, it has not been possible to distinguish clearly between the very similar P_b and P_{b0} signals; therefore the notation $P_{b(0)}$ has been adopted. At the macroscopic (100)Si/SiO_2 interface, both P_{b0} andP_{b1} point defects are observed. The P_{b1} is assigned to a distorted defected interfacial Si–Si dimer and the salient parameters make its signal distinguishable from the other P_b-type signals. Yet, it should be noted that this defect interpretation accounts for the macroscopic planar interface and in the case of nanoscopic nc-Si/SiO_2 interfaces the situation might be different. Assuming that macroscopic properties apply, the observed P_b-type defects are an indication that the nc-Si/SiO_2 interfaces are formed in accordance to the model previously inferred for the Si nanocrystal morphology, that is, a [100] truncated (111) Si octahedron [232]. As previously outlined, the EX centers, specific to a-SiO_2, are modeled as a positively charged Si vacancy with the unpaired electron delocalized over the four surrounding O atoms of which two are connected by a bent bond [124]. EX point defects are observed in all studied samples and seem to be a *relic* of structural

reorganization in the sample during high-T annealing.

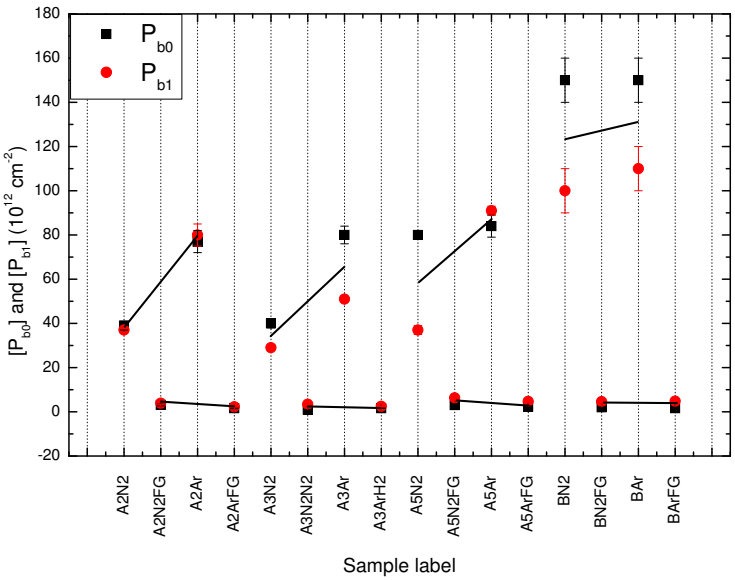

Figure 2.12: The ESR densities of P_b-type defects measured on samples A2, A5, and B, both N_2 and Ar annealed ones, before and after subsequent subjection to a forming gas passivation step, carried out within the perspective to study the influence the different anneal treatments have on the density of the ESR active centers.

In Fig. 2.12 the densities of observed P_b-type defects ($P_{b(0)}$ and P_{b1}) are plotted for each N_2, Ar, and additionally forming gas annealed sample; their densities being also listed in Table 2.3. As evident from Table 2.3, we observe for the size controlled samples (i.e., A2, A3, and A5) in average about 25-50 % less P_b-type defects for N_2 annealing than for Ar, whereas the not size controlled sample B reveals an about equal DB densities for both annealing atmospheres.

As seen in Fig. 2.12, the beneficial effect of the N_2 anneal (compared to Ar) on the obtained P_b-type Si DB's is more prominent for smaller size nc-Si. The difference between $P_{b(0)}$ and P_{b1} density increases with increasing nc-Si size. This might indicate that N atoms have a preference toward bonding to P_{b1} paramagnetic centers, the main difference from the $P_{b(0)}$ model being that one of the backbonds is strained, and larger nc's are more prone to strain. N atoms are three times coordinated, representing an adequate intermediate from the stoichiometry point of view between Si and O, an element in decreasing stress at the c-Si/a-SiO_2 interface. In the case of small nc-Si's the N atoms do not seem to have the same preference of bonding to strained centers.

Dividing the total of the P_b-type defect density at the nc-Si/SiO_2 interface (Table 2.3) by the respective number of deposited bi-layers we obtain, e.g., in the case of N_2 annealings, ∼2.3, 1.5, and 1.4 × 10^{12} cm^{-2} for samples A5N_2, A3N_2 and A2N_2, respectively. Assuming [211] a constant number of nc's per superstructure bi-layer, we observe a smaller probability of having relaxing interface point defects for smaller size nc's. More research is underway to evaluate and understand the influence of particle dimension on the presence of defects.

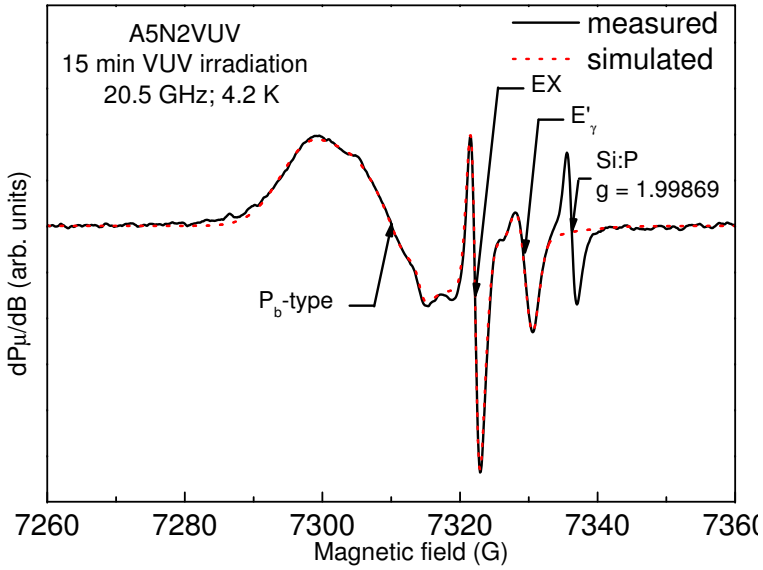

Figure 2.13: Representative K-band ESR spectrum measured at 4.2 K on an N_2-annealed sample (A5N2) subjected to 15 min VUV irradiation. The dotted curve represents an optimized spectral simulation.

Samples A5N_2VUV and A5ArVUV were subjected to VUV irradiation to maximally activate defects. Subsequent ESR measurements revealed no change in the P_b-type DB signals indicating no unintended H_2 passivation, as expected from the high degree of purity of the annealing system. Yet, now an increase in the EX density is observed and the E'_δ signal appears, as shown in Fig. 2.13 for sample A5N_2VUV. Both centers pertain to the a-SiO_2 matrix.

Figure 2.14 shows a K-band ESR spectrum measured on a N_2 annealed sample subsequently thermally treated in forming gas to passivate the paramagnetic defects. As indicated in the figure, the $P_{b(0)}$, P_{b1}, and EX defects, also observed in the as-annealed samples (cf. Fig. 2.11), remain present but in much lower densities. After subtracting through computer simulation of the intense P_b-type and EX

signals, another small signal becomes apparent in the spectrum in the vicinity of g = 2.0038 of Gaussian shape with $\Delta B_{pp} \sim 9$ G.

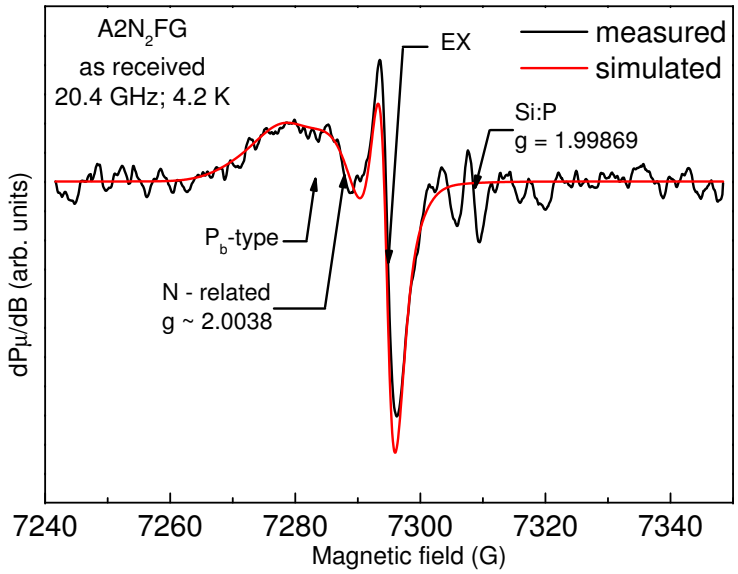

Figure 2.14: A typical ESR spectrum measured at 4.2 K using the K-band spectrometer on the N_2 annealed sample A2N_2 subsequently passivated in forming gas (sample A2N_2FG).

An ESR spectrum of the sample annealed in Ar and subsequently in forming gas is shown in Fig. 2.15. When comparing to Fig. 2.14, it can be seen it is similar to the spectrum corresponding to the N_2 and forming gas annealed superstructures, including the presence of the weak signal in the g $\sim$ 2.0038 range. The latter signal, however, has lower intensity in this case. We assign this signal, present in both types of samples, to the K center, that is, a defect associated to an unpaired electron localized on a Si backbonded to three N atoms. The K center might be close to the nc-Si/SiO_2 interface as suggested by Wilkinson et al. [149].

Nitrogen is known not to be inert during high-T annealing of the Si/SiO_2 entities and the factors affecting the nitrogen-reaction kinetics are similar to those affecting oxidation of silicon in dry oxygen [142]. This is the main reason for which Wilkinson et al. [149] are placing the incorporated N atoms at the nc-Si/SiO_2 interface. The N atoms in the anneal ambient are considered to infiltrate into the sample and suppress subsequent diffusion of Si atoms and Si clustering during high temperature thermal treatment [233] or produce Si nitridation at the nc-Si/SiO_2 interface [149]. The K center density is found to be larger for samples annealed in N_2 and subsequently in forming gas than for the samples annealed initially in Ar and in forming gas

afterwards (cf. Table 2.3), indicating that the N atoms penetrate into the samples not only during the N_2 treatment, but also during the forming gas anneal.

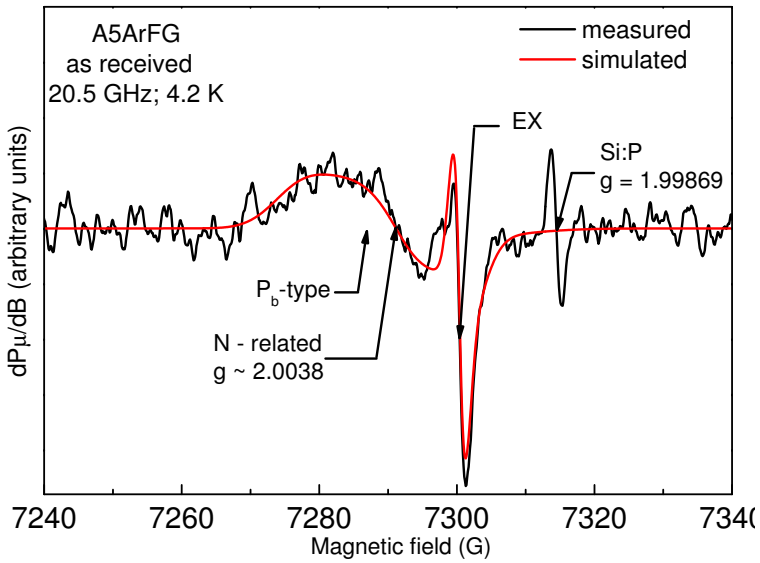

Figure 2.15: K-band ESR spectrum measured at 4.2 on the Ar annealed sample passivated in forming gas (sample A5ArFG).

Forming gas passivation results for all samples in reduced $P_{b(0)}$ and P_{b1} defect densities, now in the range (1.6 - 6) $\times$ 10^{12} cm^{-2}. However, the defect ratios remain similar and on average $\frac{[P_{b(0)}+P_{b1}]_{N_2+H_2}}{[P_{b(0)}+P_{b1}]_{Ar+H_2}} \sim 0.6$, i.e., the DB signals in the N_2 annealed and passivated samples are about 2/3 of that of Ar annealed and passivated ones. Thus, N_2 annealing of Si nc's grown in a-SiO_2 matrix is generally beneficial in terms of interface defects and PL intensity [234].

To investigate whether the forming gas anneal is as effective as pure H_2 ambient in passivating (paramagnetic) point defects, sample A5ArFG was additionally annealed in H_2. This is found to result in a reduction of the P_b and EX center densities, while $[P_{b(0)}]$ is passivated to below the ESR detection level (cf. Table 2.3) suggesting that pure H_2 would be a better passivating ambient than forming gas. For this reason samples A3 ($A3N_2$ and A3Ar) have been passivated in pure H_2 instead of forming gas. The K center signal is not observed in those samples.

2.3.6 Paramagnetic point defects and PL

Physically the same samples investigated here by ESR were also investigated by PL [234]. The as-annealed samples show intense PL that increases significantly after forming gas passivation of defects. In order to demonstrate the effect of the H_2 treatment, Fig. 2.16 shows the normalized ratio of P_b-type defects before and after passivation as well as the normalized PL intensity ratio before and after passivation for three samples (A2, A5 and B). Most notably, this reveals a clear correlation between the increase of PL intensity and the decrease of $P_{b(0)}$ defect density, which appears not to be the case for P_{b1} and EX centers. Due to the SiO_2-associated nature of the EX defect it is less expected to affect PL directly. However, the absence of any obvious corelation between PL and P_{b1} defects is noteworthy. The measurements indicate that the $P_{b(0)}$ interface defects are mainly responsible for quenching the nc luminescence while the presence of P_{b1} at the same interface plays a minor role for the PL properties [234].

As assessed by Hiller et al. [234], the passivation also results in a PL redshift (compared to the unpassivated samples), that can be explained by preferential emission enhancement from larger nc's (which are more prone to be affected by PL quenching defects [235]).

With respect to the PL peak position [234], there is a relevant difference between N_2 and Ar annealed samples when the nc-Si are small (blueshift), but the difference decreases with increasing nc-Si size. Time resolved PL experiments indicate similar lifetimes for the small nc's indifferent of the annealing ambient, which indicates identical sizes for the Si nc's attained when annealing the sample in N_2 and Ar. This finding objects to the previous inference suggesting suppression by N of Si diffusion and thus cluster growth as explanation for the PL blueshift after N_2 annealing. Instead, an alternative explanation is given starting from the electronic structure of nc-Si in various matrices influenced by different polarities of the nc terminating groups such as O and N, as modeled [236] by density functional theory (DFT). N atoms incorporated at the nc-Si/SiO_2 interface are changing the polarity of the surrounding dielectric and thereby the electronic structure of the Si nc's. Thus for the small nc size (e.g., 2 nm – sample A2) where, according to DFT calculations quantum confinement is contributing to the PL, the emission is dominated by the interface [236], and a significant blueshift is observed for the N_2 annealed sample signal compared to the Ar annealed one. For the larger nc's, since the emission is dominated by quantum confinement, the PL position is then less affected by the annealing ambient.

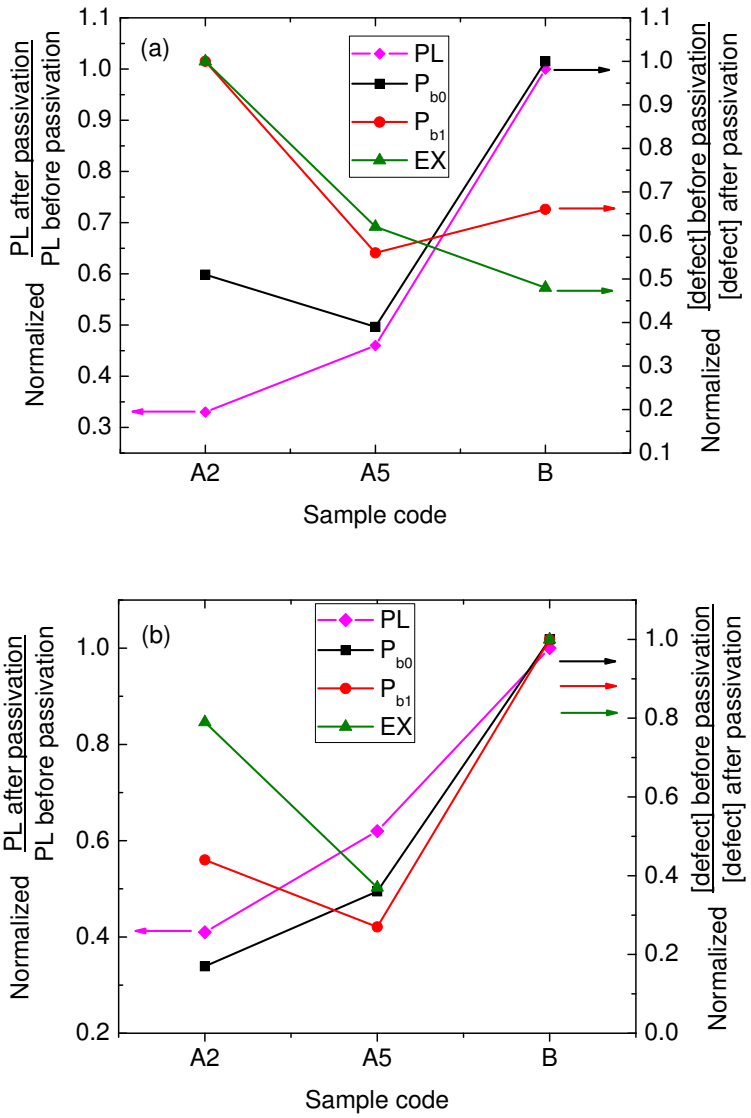

Figure 2.16: The normalized ratios of PL intensities and paramagnetic point defects densities observed on the samples A2, A5 and B annealed in (a) Ar and (b) N_2. The lines guide the eye.

2.3.7 Conclusions

In conclusion, the superior nc-Si/SiO_2 interface quality achieved by N_2 annealing in terms of P_b-type defect densities has been presented, and from comparison with PL intensity measurements, it is concluded that PL is quenched mainly by $P_{b(0)}$ defects; their influence can be minimized if passivated by bonding to H atoms. The P_{b1} and EX centers, also present in the as annealed samples, show no influence on the sample's PL behavior.

The observed $P_{b(0)}$ and P_{b1} center densities in nc-Si/SiO_2 densities are considerably larger that of EX centers in all the as-annealed samples. Annealing the samples in N_2 seems more efficient than in Ar regarding the densities of P_b-type centers, but less effective in the case of EX centers, indicating that N atoms from the annealing ambient are bonding preferentially at the nc-Si/SiO_2 interface. The N atoms seem to infiltrate into the samples structure during forming gas anneal, forming K centers which are observed in all forming gas passivated samples, their density being higher for the N_2+FG samples compared to the Ar+FG ones. The N absorption into the superstructures is cumulative for all the N-containing annealing ambients for T_{an} = 500-1100 °C.

The P_b-type density per SiO/SiO_2 bi-layer is showing a tendency towards more defects for the superstructure containing bigger nanoparticles (double P_b density for the 5 nm –sample A5– particles layers compared to the 2 nm case –sample A2), but further work is needed for a deeper understanding. The N-related centers are observed in all forming gas passivated samples, larger for the samples initially annealed in N_2 than for those annealed in Ar. Also, for smaller nc's, over all P_b-type defects the difference in density is observed in samples annealed in N_2 and Ar but is not observed for smaller nc's.

The ESR measurements on samples A2, A5, and B after annealing in forming gas (for defect passivation) show a decrease in $P_{b(0)}$, P_{b1} and EX intensity and a very small signal attributed to K centers (g $\sim$ 2.0035 - 2.0038). If present in the as annealed samples, the K centers are masked by the large signals pertaining to the interface P_b-type centers. The samples A3N_2 and A3Ar passivated in pure H_2 instead of forming gas show no evidence of K centers. The K-center signal present in samples additionally annealed in forming gas is larger for the samples where the agglomeration and crystallization of the nc-Si are effectuated in N_2 ambient, indicating that during this initial N_2 anneal N atoms are infiltrating in the structure, also resulting in an efficient PL. No such effect is observed when the superstructure is annealed in Ar.

$P_{b(0)}$ centers are more efficiently passivated by forming gas (IMTEK) than P_{b1} centers suggesting that N atoms prefer bonding to more strained paramagnetic centers (the center becomes diamagnetic). Defect passivation in forming gas works best for the A5Ar samples with an overall low P_b-type defect density obtained for

Ar annealed samples vis-à-vis N samples (weak trend). The situation is different in the case of pure H_2 passivation where the $P_{b(0)}$ centers are relatively more reduced than P_{b1}).

Annealing the samples in pure H_2 subsequent to the forming gas anneal additionally decreases the P_b-type defects (the $P_{b(0)}$ density falls below detection levels and $[P_{b1}]$ decreases ~ 5 times) and the drastic defect passivation is observed also for samples A3Ar and A3N_2 annealed in H_2 gas without a previous forming gas anneal. This points towards H_2 as a more adequate anneal ambient for nc-Si/SiO_2 structure to attain defect passivation.

Chapter 3

Influence of in situ applied ultrasound during Si^+ implantation in SiO_2 on paramagnetic defect generation

3.1 Introduction

The importance of the nc-Si particles embedded in a-SiO_2 for future technologies has been detailed in Chap. 2 together with the favored fabrication methods discussed in the literature, the majority being based on high-T annealing of Si-rich SiO_2 obtained by various methods. Within the framework of this research, combining ESR investigation of point defects with PL measurements demonstrated the possibility to control the origin of the PL between defects and quantum confinement in nanocrystalline (nc) -Si/SiO_2 entities obtained by the superlattice approach [207]. This accentuates the need to efficiently suppress point defects at nc-Si/SiO_2 interface for the emitted PL to be of quantum confinement origin, thus allowing bandgap modulation.

Implanting Si^+ ions into a target oxide to increase the Si concentration above stoichiometric values is a preferred approach [237, 238] because of its easy integration into mass fabrication procedures (implantation is routinely used for

Si IC production), and other advantages such as easy masking methods, good control on the concentration of the implanted ions, as well as on spacial distribution and ion penetration depth [239]. Also, the possibility to extend elemental cluster forming compounds using sequential implantation of different ions. One drawback, however, is the huge number of detrimental dangling bonds (DB's) introduced by the passage of the high-energy ions through the oxide: Bonds are being broken and part of the (displaced) ions left not fully integrated into the network.

Ultrasonic stimulated processes in Si and Ge were discovered long ago, and have been intensively explored over the last two decades [240, 241]. It is presently used in defect engineering, to improve the performance and reliability of electronic devices [241, 242]. As interpreted, mechanical vibrations help atomic systems to reach a better energetic state by increasing the mobility of interstitials and vacancies [243], decreasing the activation energy of point defect migration [242, 244] and affecting the kinetics of point defects [245, 246]. The enhanced mobility of the interstitial atoms would lead to enhanced annihilation with vacancies, that is, removal of intrinsic point defects [242]. The increased diffusion has also a beneficial effect on the nc nucleation and growth [240, 245]. Previous reports show that the effect of in situ applied ultrasound (US) during implantation of SiO_2 with Cu or Ag ions lowers the precipitation threshold and increases cluster size [196, 247]. It may then come as a logical extension to study the influence of applying in situ UST during ion implantation in oxides in an attempt to affect (reduce) defect densities.

In view of the observed structural modification induced by the in-situ applied US field, and the suggested role of intrinsic point defects in this effect, it would seem natural to attempt to extend experiments to analysis by electron spin resonance (ESR), the technique of choice for investigation and identification of point defects *on atomic scale*. Accordingly, we report on extensive ESR measurements carried out in the temperature range T = 4.2-300 K to monitor and unveil, on atomic scale, the effect of in situ UST during Si^+ ion implantation in thermal SiO_2. Using ESR, we effectively employ the unpaired electrons as local atomic "eyes", sensing their surrounding. The UST effect is revealed here as impressively affecting (reducing) defect formation, both regarding defect types and changes in the densities: A main finding is the drastic reduction of O-vacancy type defects in the SiO_2 matrix. A detailed assessment in terms of the atomic nature of the various types of point defects involved is included.

3.2 Experimental details

3.2.1 Sample preparation

Investigated samples were obtained starting from growing 340-nm thick thermal SiO_2 on 500-μm thick B-doped (100)Si wafers in dry oxygen at 1150 °C. Various samples were single-side implanted (into the a-SiO_2 side) in one run at 300 K with 90 keV Si^+ ions to a dose of 8×10^{16} cm^{-2}, without (reference samples 3K and 4K) or with (2KU) in situ subjection to 9.5 MHz UST for the entire duration of the implantation as reported elsewhere [196, 248]. For the ESR measurements, slices of 2×9 mm^2 main area were cut, where typically four were stacked in an ESR sample, forming a total implanted area not exceeding 0.72 mm^2. After protectively covering the implanted side, cutting and backside damage was removed through wet chemical etching (CP4). With the protective cover still on, slices were dipped in aqueous HF (5 % HF in H_2O; 30 s) prior to each ESR measurement.

High-T annealing is used to enhance the mobility of Si atoms and their agglomeration into Si nc's embedded in SiO_2. For this end, after initial ESR probing, pristine slices of samples 3K and 2KU were subjected to additional PIA at 1100 °C in N_2 for 40 min, resulting in the sets 3Kan and 2KUan, respectively. See Table 3.1 for an overview of the samples studied.

3.2.2 ESR spectroscopy

As the goal of this investigation is to trace and analyze, both qualitatively and quantitatively, the influence of in situ UST during the implantation process in terms of point defects involved, ESR is used as a tool able to provide information on the true atomic level through probing properties of the unpaired electron orbit of paramagnetic defects. ESR experiments were carried out in the range 4.2-300 K using X, K and Q band spectrometers, as outlined in Chap. 1. Conventional cw first derivative-absorption (dP_μ/dB) spectra were measured through applying sinusoidal modulation (∼100 kHz; amplitude $B_m \leq 0.8$ G) of the externally applied magnetic field $\overrightarrow{B}$, with incident microwave power $P_\mu \leq 8 \times 10^{-10}$ W, i.e., cautiously reduced to avoid signal distortion.

The implantation process is creating a high density of defects, so the small amount of the investigated sample surface/volume does not prevent attaining good ESR sensitivity. However, that situation alters after annealing. The applied thermal budget results in a drastic decrease in the defect density and, consequently, signal-to-noise ratio has to be compensated by extensive signal averaging, typically raised now to ∼100-150 scans. The relative error in defect density determination is limited (down to 3-9 %) by first computer simulating each ESR signal, including the one

pertaining to an included reference sample, using known parameters such as line shape and g values from previously reported spectra. Absolute paramagnetic defect densities were determined through double numerical integration of the computer simulations by comparison, usually, of each signal to a co-mounted Si:P marker, or to a MgO:Mn marker in the case of X-band room temperature measurements.

3.2.3 Sample morphology

After high-T annealing, with and without applied US, similar samples (600 nm instead of 340 nm thick grown a-SiO_2 implanted by 100 keV Si^+ ions) as the ones investigated here, prepared and annealed along the same procedure, were investigated by cross-sectional HRTEM, PL, and photoelectron spectroscopy (PES) measurements and the results were reported recently by Romanyuk et al. [248] . Bright field HRTEM measurements of the annealed samples indicate np-Si formation with an average size of 1.92 ± 0.7 nm and 1.97 ± 0.7 nm for the ones without or with UST, respectively, with a sharper particle size distribution for the later [248], so it seems UST is not influencing the nc-Si average diameter as it does for Ag particles [196], but stimulates a growth more uniform in size.

Using the SRIM code [249], simulation of the implanted Si^+ atom distribution in the a-SiO_2 layer gives a peak implantation depth of ∼134.2 nm (in accordance with the 130 nm value measured by dark field TEM [248]) with half-height width of ∼89 nm. Importantly, no implantation damage of the remote substrate-Si/SiO_2 interface would have occurred in any of the samples studied here.

From PES measurements Romanyuk et al. [248] observed intermediate oxidation states in the as implanted samples but not for the UST samples, indicating a sharper nc-Si/SiO_2 interface as a result of the UST application. They attribute a PL ∼ 1.5 eV line to suboxide states, relating the luminescent emission to defects at the nc-Si/SiO_2 interface (decreasing after UST) and there is no indication of quantum confinement effects in their report.

The details provided by ESR about the actual location of paramagnetic centers in the implanted SiO_2 matrix, their density, and presence of demagnetization features, are all valuable in deriving morphological properties. Information about the nc-Si/SiO_2 interface orientations can tentatively be assessed with the help of ESR active P_b-type interface defects, as discussed later.

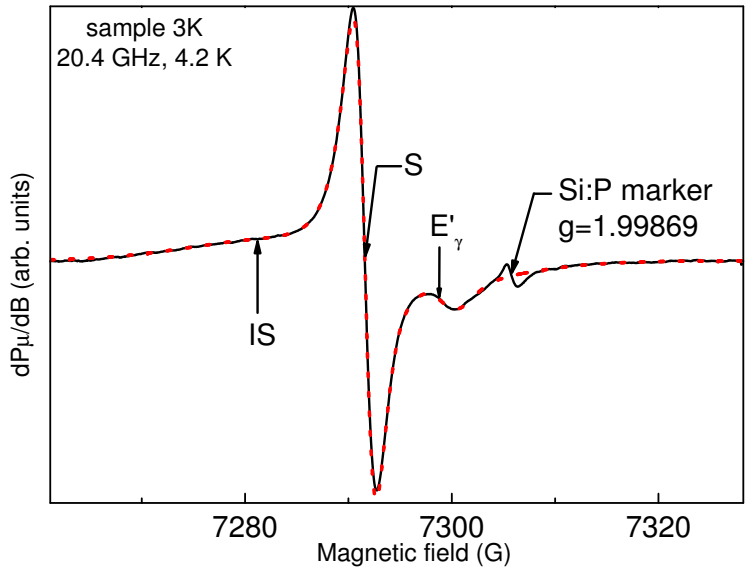

Figure 3.1: Continuous-wave low power first harmonic K-band spectrum taken on sample 3K at 4.2 K for $\varphi_B = 55\,^\circ$ using $P_\mu \approx 8 \times 10^{-10}$ W and $B_m \approx 0.5$ G. An intense spectrum is observed (solid trace) composed of three types of signals, marked as S, E'_γ, and IS. The signal at $g_c = 1.99869$ stems from a co-mounted Si:P marker sample. The dashed curve represents an optimized spectral fitting based on the powder pattern approach and known spectral properties of the resolved signals (defects).

3.3 Results and analysis

3.3.1 Paramagnetic defects in reference samples

Figure 3.1 shows a typical K-band spectrum observed for $\varphi_B = 55\,^\circ$ (the field angle of $\overrightarrow{B}$ with $\overrightarrow{n}$, the [100] Si substrate normal) on reference sample 3K, revealing the presence of various types of signals (defects). Apart from the Si:P signal, three different signals may be distinguished. Starting from the high field side, the signal closest to the marker, based on its zero crossing g value g_c =2.00055 and specific signal shape, unmistakably originates from the E'_γ center [86] (generic entity $O_3 \equiv Si^\bullet$); the identification is further supported by the observation of the 434 G associated ^{29}Si hf doublet [39, 133] (not shown here). The inferred density amounts to $[E'_\gamma] = (2.8 \pm 0.1) \times 10^{14}$ cm^{-2}.

Second, we observe an intense rather narrow symmetric signal of Lorentzian shape

with peak-to peak width $\Delta B_{pp} = 2.3 \pm 0.2$ G and corresponding density of $(2.9 \pm 0.2) \times 10^{15}$ cm^{-2}. Assuming the originating centers to be uniformly distributed over an 89 nm thick layer as obtained from SRIM calculation, this gives a high volumetric density $N_V \approx 3 \times 10^{20}$ cm^{-3}. As the ESR study concerns defects residing in an amorphous SiO_2 matrix, one would routinely expect the observation of "isotropic" or powder pattern line shapes. Yet, angular measurements for changing field angle φ_B and T-dependent study indicated the g_c of this signal (unlike the other signals observed) to exhibit a specific field anisotropy that asymptotically vanishes towards high-T. The φ_B-independent, reference value of g_c (g_{ref}) is obtained (vide infra) from room temperature (RT) X-band spectrometry as $g_{ref} = 2.00252 \pm 0.00005$. As detailed later, we assign this signal to S centers ($SiO_2 \equiv Si^{\bullet}$) [33, 130, 131], characteristic for Si-enriched SiO_2. In Fig. 3.1, this signal is noticed to be slightly asymmetric due to a slight g matrix anisotropy, as reported before [35].

Finally, the broad isotropic signal, extending over almost the whole spectrum, could be accurately simulated using a Gaussian line shape of $\Delta B_{pp} = 20.0 \pm 0.4$ G centered at $g_c = 2.0026 \pm 0.0001$, resulting in a density of $(4.2 \pm 0.4) \times 10^{15}$ cm^{-2}. No previous report of such signal could be traced in the literature. The signal is labeled as IS (Implantation induced Signal).

K-band measurements performed on sample 4K gave very similar results as sample 3K. All three types of centers are present in the same ratios (within the experimental error), indicating that the implantation method is reproducible in terms of induced paramagnetic defects.

3.3.2 Influence of UST on as-implanted samples

Figure 3.2 shows a K-band spectrum observed at 4.2 K for $\overrightarrow{B} \perp \overrightarrow{n}$ on the 2KU sample in situ treated by US during Si^+ implantation. Only the two signals corresponding to S and E'_γ centers remain visible here. Compared to the 3K reference sample (Fig. 3.1), a drastic decrease, by ∼60 times, in *total* number (signal) of defects is noticed, i.e., from $(7.3 \pm 0.5) \times 10^{15}$ cm^{-2} for 3K to $(1.2 \pm 0.1) \times 10^{14}$ cm^{-2} for 2KU, cf. Figs. 3.1 and 3.2 where the same marker was used and about equal sample area. The IS signal is seen to drop below the detection limit.

The evolution of defect density with different treatments enumerated in Tab. 3.1 is pictured in Fig. 3.3 to better expose the UST impact. Left and right parts correspond to the as-received and annealed samples, respectively. The lines guide the eye. The in situ UST applied during implantation is thus found to ensue a drastic effect on the defect densities, in the sense of improving sample quality.

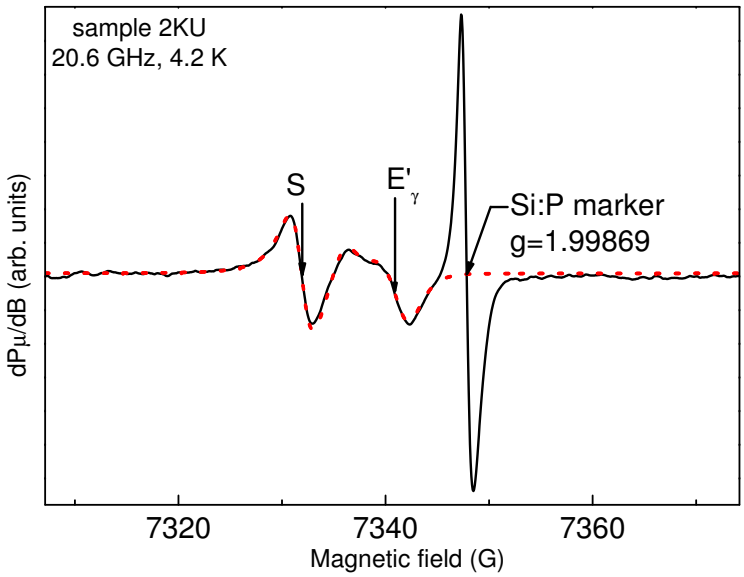

Figure 3.2: A representative low power first harmonic K-band spectrum measured on sample 2KU at 4.2 K, for $\varphi_B = 90\,^\circ$. Only S and E'_γ centers signals are observed in this case. The dotted curve represents an optimized spectral fitting.

Table 3.1: Treatments performed on (100)Si/SiO_2 structures with the SiO_2 layer implanted by 90 keV Si^+ ions (8×10^{16} cm^{-2}; 300 K). The UST was applied in situ.

Sample	UST	Anneal	
	UST frequency (MHz)	temperature (°C)	time (min)
3K	-[a]	-	-
4K	-	-	-
2KU	9.5	-	-
3Kan	-	1100	40
2KUan	9.5	1100	40

[a] - means, not applied

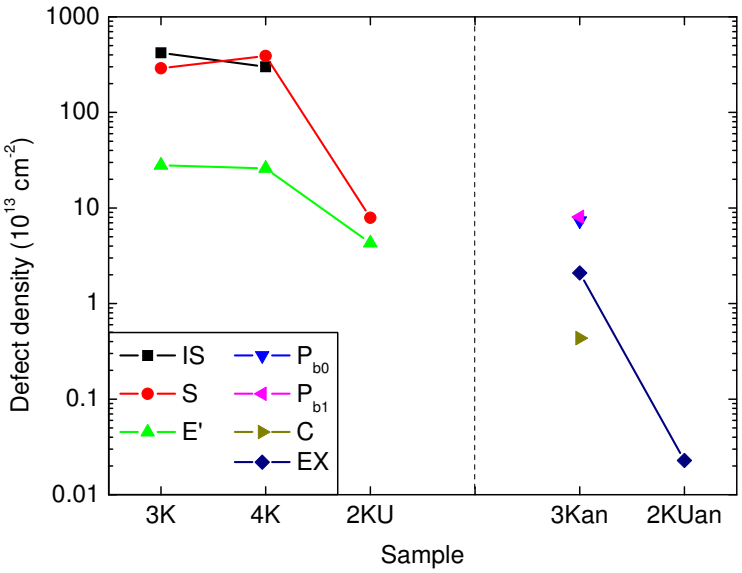

Figure 3.3: Inferred areal densities of the paramagnetic centers resolved in the as-implanted and annealed samples, both with and without UST application during implantation. The graph clearly shows the drastic impact of in situ UST in decreasing defect numbers, an effect maintained also after annealing. Error bars are within the size of the symbols.

3.3.3 Magnetism of S centers

The kind of magnetic behavior of the S defects was investigated by measuring the ESR intensity $\mathcal{I} \propto \chi$, as a function of T in the range of 4.2-36 K for $\overrightarrow{B} \parallel \overrightarrow{n}$. The data, shown in Fig. 3.4 for sample 4K as a $1/\chi$-vs.-T plot, indicate a Currie-Weiss type behavior, i.e.,

$$\chi = \frac{C}{T - T_C} = \frac{\mu_0 N_V g_c^2 \beta^2 S(S+1)}{3k_B(T - T_C)}, \tag{3.1}$$

where μ_0 is the free space magnetic permeability, β the Bohr magneton, S the defect spin, k_B the Boltzman constant, T_C is the Currie temperature, and C the Currie constant, proportional to the volumetric spin density N_V. Optimized fitting of Eq. 3.1 gives $T_C = 0 \pm 1$ K, pointing to a purely paramagnetic system comprised of negligibly interacting magnetic moments (defects).

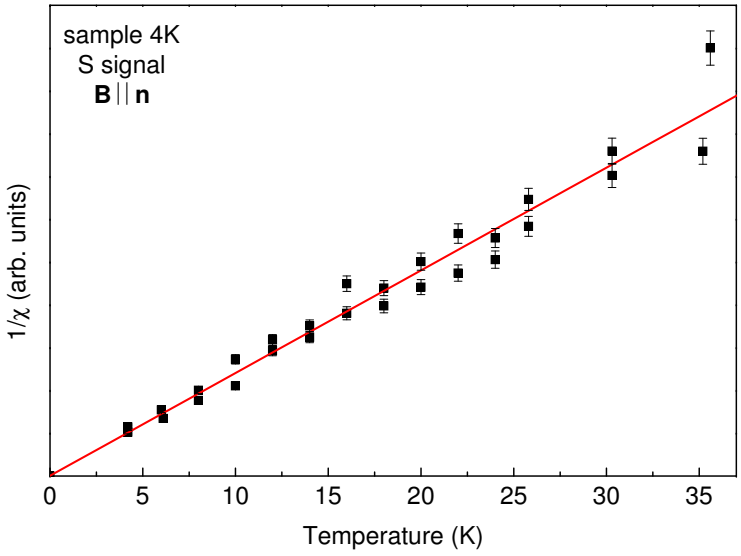

Figure 3.4: Temperature dependence of the intrinsic ESR intensity $\mathcal{I}$ ($\propto \chi$) of the S signal measured in the sample 4K for $\varphi_B = 0\,^\circ$ (K-band data). The solid line represents a fit of Eq. (1), from where a Currie temperature $T_C = 0 \pm 1$ K is inferred, pointing to a close Currie type susceptibility behavior.

3.3.4 Demagnetization effects

Commonly, no anisotropic (φ_B dependent) ESR signals are expected from ion-implanted a-SiO_2. However, such anisotropy was observed in the case of the S signal, yet not for the IS and E'_γ signals. The anisotropy could readily be traced down as originating from demagnetization effects (a sample shape effect) indicating the signal to stem from a *large* local density of defects in a planar (thin film) arrangement, consistent with the inferred large volume density (here $> 3 \times 10^{20}$ cm^{-3}) in combination with the limited Si^+ implantation depth. The effect is only observed on as-implanted samples showing a very intense S-signal –but not after annealing. Figure 3.5 depicts the dependence of g_c on φ_B, (relative accuracy $\approx$ $0.5\,^\circ$) as obtained from K-band (4.2 K) spectra for the three investigated unannealed samples. For example, in the case of sample 3K, g_c(4.2K) is seen to evolve between 2.00170 ± 0.00005 ($\vec{B} \| \vec{n}$) and 2.00307 ± 0.00005 ($\vec{B} \perp \vec{n}$), definitely well beyond experimental error. A slight decrease of ΔB_{pp} with increasing φ_B of ≈ 0.4 G was also observed, that is, from $\Delta B_{pp}(\varphi_B = 0\,^\circ) \approx 2.5$ G to $\Delta B_{pp}(\varphi_B = 90\,^\circ) \approx 2.1$ G. Figure 3.6 shows the extreme g values, $g_\parallel$ and $g_\perp$, as a function of T in the range 4.2 - 36 K for sample 4K, the one exhibiting the most pronounced anisotropy of

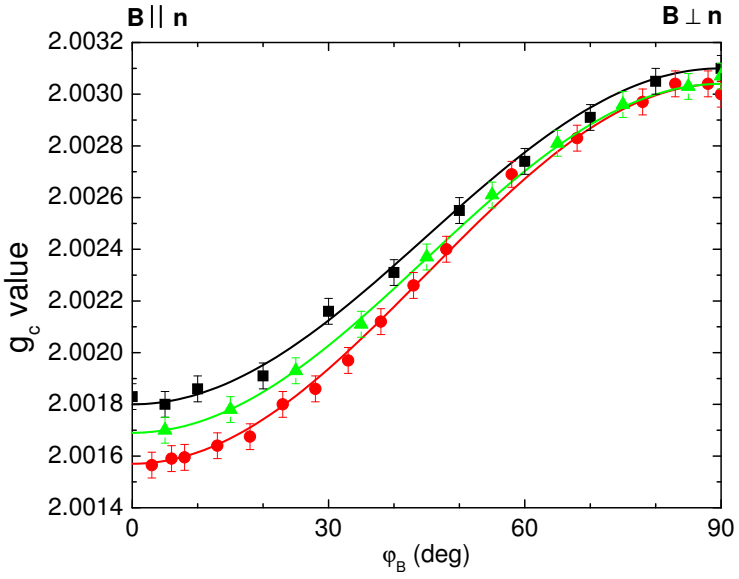

Figure 3.5: Anisotropy of the S center g_c value as a function of the magnet angle φ_B as measured by K-band ESR at 4.2 K on samples 3K(▲), 4K(■) and 2KU(●). The solid lines represent simulations using Eq. (2). The g shift arises from demagnetization (shape effect) for a system of defects of high local density residing within a thin layer.

all. It is obvious from this figure that both extremes tend to merge into a singular value at higher temperatures with attendant vanishing of the g anisotropy. The angular anisotropy is found to be suppressed in RT X-band spectra: a Lorentzian isotropic signal is observed with $\Delta B_{pp} = 2.2 \pm 0.1$ G giving for g_c the reference value $g_{ref} = 2.00252 \pm 0.00005$ unaffected by demagnetization.

3.3.5 Annealed samples

The effect of PIA (1100 °C; N_2) has been investigated with the view to trace any possible correlation of the initial implantation induced point defect damage with the post anneal result. Figure 3.7 shows (top curve) a K-band spectrum observed at 4.2 K on sample 3Kan. As expected, compared to the unannealed state (Fig. 3.1), the ESR spectrum has substantially changed, with all three previous signals –E'_γ, S and IS– being eliminated beyond detection. Computer-assisted spectral disentanglement now, instead, indicates the presence of (at least) four types of other defects, albeit with overall much reduced densities. Two pertain to the Si/SiO_2 interface, namely P_b and/or P_{b0}, and P_{b1}, in almost equal quantities,

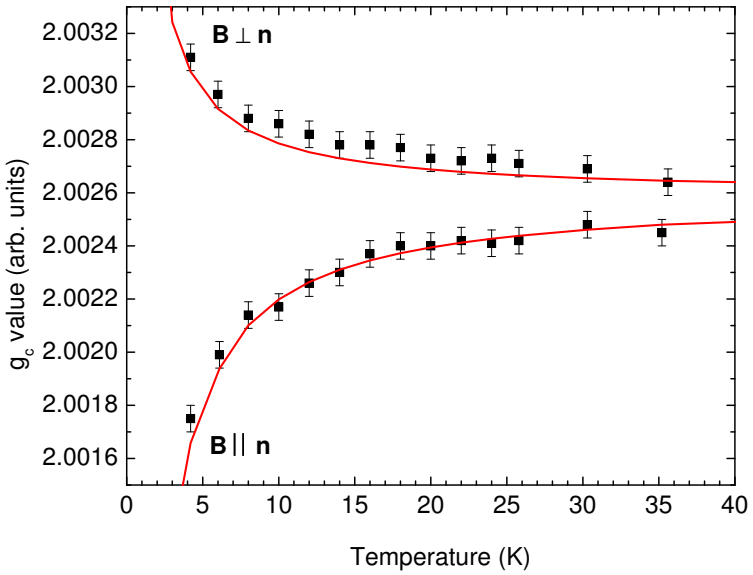

Figure 3.6: Evolution as a function of T of the extreme g_c values of the S signal obtained at K-band for $\varphi_B = 0\,^\circ$ and $\varphi_B = 90\,^\circ$ on sample 4K. The solid curves represent optimized fittings based on Eqs. 3.1 and 3.3.

summing to $(1.5 \pm 0.1) \times 10^{14}$ cm^{-2}, and indicating that nc-Si particles have been formed [232] within the a-SiO_2 matrix during the post manufacturing anneal. The observed responses exhibit powder pattern line shapes, and were simulated that way, using known principal g values, showing no $\overrightarrow{B}$ direction anisotropy.

Besides the interface specific signals, an intrinsic a-SiO_2 center emerges with density $\approx 2.1 \times 10^{13}$ cm^{-2} at $g_c = 2.00255 \pm 0.0002$, i.e., the EX defect, as confirmed by the observation of its characteristic 16.3 G split hyperfine (hf) doublet. A fourth signal at $g_c = 2.00300 \pm 0.00003$, with corresponding density of $(4.6 \pm 0.8) \times 10^{12}$ cm^{-2}, is ascribed to C impurities [50, 250, 251] in SiO_2, a contaminant probably introduced during implantation.

By contrast, a much noteworthy observation is that as illustrated in Fig. 3.7 (bottom spectrum), only a faint EX signal remains as sole ESR *relic* in the US-treated sample after annealing, 2KUan, about two orders of magnitude smaller than for the 3Kan reference sample. As the two samples were physically annealed together in the same step, it points to the in situ UST as the decisive factor of difference. This, interestingly, reveals the combination of in situ US treatment with post implantation high-T annealing as a process resulting in virtually the entire removal (prevention) of paramagnetic point defects beyond the ESR sensitivity

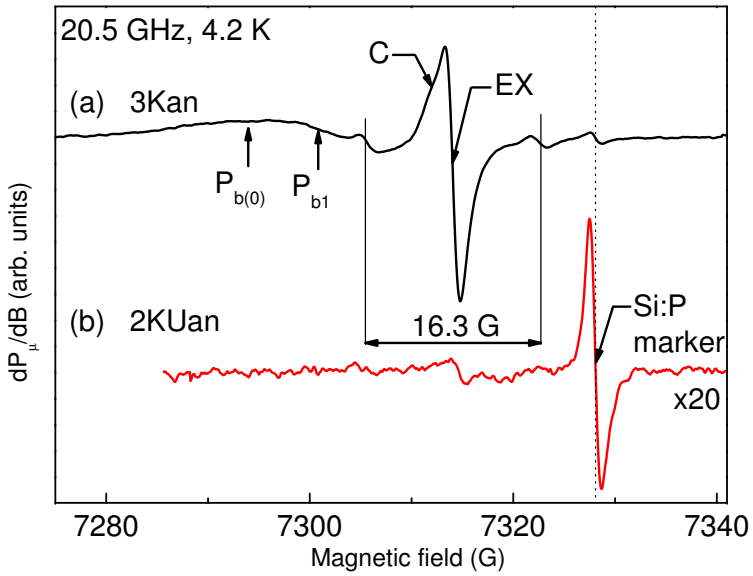

Figure 3.7: The specific K-band spectra taken at 4.2 K ($B_m \lesssim 0.6$ G; $P_\mu \approx 3 \times 10^{-10}$ W) on the annealed samples 3Kan and 2KUan (1100 °C; 40 min; N_2). The $P_{b(0)}$ and P_{b1} signals indicate nc-Si formation. Only a weak EX signal remains observable for the UST sample.

limit.

3.4 Interpretation and discussion

3.4.1 As-implanted samples

The K-band ESR spectra measured at 4.2 K on the reference samples 3K (cf. Fig. 3.1) and 4K are similar, so, we will restrict the discussion to 3K data unless specified otherwise. In the as implanted reference samples three paramagnetic defects are observed by ESR. The signal closest to the marker, as indicated in Fig. 3.1, is assigned to the a-SiO_2 specific E'_γ point defect based on the specific double peak powder pattern shape and the $g_c = 2.00055$ value [94] of the signal. As discussed in Chap. 1, the E'_γ point defect can be used as an indication of the oxide quality, the typical value [103] for standard thermally grown SiO_2 on Si substrate being $\sim 3 \times 10^{17}$ cm^{-3}. The measured density in the case of our reference samples, with a SiO_2 layer of 340 nm thick, is $(8.3 \pm 0.2) \times 10^{18}$ cm^{-3}, indicating that indeed the matrix is degraded by the implantation. For this center, we also measured in

Q band at ≈ 10K the principal hf doublet arising from central ^{29}Si isotopes [40] (4.7 % natural abundance; I=1/2). Its splitting of 434 ± 2 G is found to be larger than the standard value of 420 G reported for bulk silica glasses [40, 100]. This increased hf splitting has been explained before [133, 102] as a consequence of SiO_2 matrix densification, here effected by Si^+ ion implantation, resulting in an increase of the average bond angle between the Si DB direction and the Si back bonds to O (see Ref. [102] and references therein).

Most prominent in the ESR spectrum is the sharp intense central signal of Lorentzian line shape. This signal sweeps a spectral region between $g_{\|} \approx 2.0016$ and $g_{\perp} \approx 2.0031$ with varying φ_B (see Fig. 3.5), an unexpected behavior since the as implanted samples under investigation are amorphous and the interface with the Si substrate is not reached by the implanted Si^+ ions as evident from TEM measurements [248] and SRIM simulations. It results from demagnetization effects, as detailed before. On the basis of the inferred g_{ref}, obvious SiO_2-associated defect candidates include the EX center, with g_c values reported between [124, 125] 2.00247 and 2.0027, and the S center [33, 34, 130, 131] with [33, 35, 131] g = 2.0027 ± 0.0001 attributed to [37] the n=1 variant of the $Si_nO_{3-n}Si^{\bullet}$ (n=1, 2) type centers intermediate [130, 133] between a-SiO_2-specific E'_{γ} defects [38] ($O_3 \equiv Si^{\bullet}$) and the P_b center ($Si_3 \equiv Si^{\bullet}$), the archetypal (111)Si/SiO_2 interface defect [25, 27, 53] (for more details on the point defects see Section 1.2). In a preliminary model, the EX center has been pictured as a hole delocalized over four oxygen atoms formally at the site of a Si vacancy [124]; in another view, it can also be looked at as an agglomerate of four oxygen-related hole centers. Although the "morphology" of S and EX signals is distinct, their g_c values are close. So, additional information will be needed, e.g., hf splitting, for correct assignment. Generally, the spectra of both types of defects considered include a ^{29}Si associated hf doublet. In the case of EX centers, a 16.1 G hf doublet [17] has been reported of which an example can be seen in Fig. 3.7 (top curve) measured on the *annealed* sample 3Kan. As to the S center, two (^{29}Si) hf doublets, of splitting ≈ 162 and 289 G, have been reported where over the various reports the latter one appears to fluctuate [34, 35, 36, 133] between 230 and 289 G. Yet, no doublet centered at g ≈ 2.0025 could be measured for any of the as implanted samples. This may be explained by the strong wave function overlap at high defect concentrations, the signals being exchanged narrowed (see e.g., Refs. [11] and [252]) leading to the "collapse" of the hf lines into the central signal (vide infra). This is likely the case here, where the estimated volume density exceeds 3 × 10^{20} cm^{-3}. So, no additional (^{29}Si) hf structure for this signal could be resolved, which in addition with the featureless shape makes defect identification difficult. The excess of Si introduced by implantation makes us incline towards one or a mixture of the intermediate $Si_nO_{3-n} \equiv Si^{\bullet}$ (n=1, 2) type centers, labeled as X (n=1) and Y (n=2) centers in some works [34, 132, 253].

The spectrum in Fig. 3.1 is overlapped by an isotropic Gaussian signal of ΔB_{pp} = 20 ± 0.4 G, centered at g_c = 2.0026 ± 0.0001. The origin of this signal

remains so far unknown. Being an implantation induced signal, we labeled it IS. Although the density of IS centers is comparable to that of S centers (cf. Fig. 3.3), no demagnetization effects could be noticed, indicating then a broader depth distribution over the oxide, i.e., a lower local volumetric density.

For completeness, we mention the inferred defects densities for the other reference sample, 4K. These are given as [IS] = (3.0 ± 0.1) × 10^{15} cm^{-2}, [S] = (3.9 ± 0.1) × 10^{15} cm^{-2} and $[E'_\gamma]$ = (2.6 ± 0.1) × 10^{14} cm^{-2}, i.e., in the same range as the respective densities for the sample 3K, indicating a reproducible implantation process in terms of point defects.

3.4.2 Demagnetization

As noticed before, Fig. 3.5 reveals the remarkable observation that for all as-implanted samples, the g_c value of the main ESR signal (cf. Figs. 3.1 and 3.2) is dependent on φ_B. Yet, as it is attributed to S centers in a-$SiO_{2(x)}$, that is, an amorphous material, microscopic defect anisotropy like, e.g., due to g anisotropy will be averaged out orientationally. So, the response –a *powder pattern*– should be isotropic. As illustrated by the full curves, the experimental values, varying between $g_\parallel$ and $g_\perp$, can be well fitted by:

$$g_c = \sqrt{(g_\parallel \cos\varphi_B)^2 + (g_\perp \sin\varphi_B)^2}, \tag{3.2}$$

describing the g anisotropy for an axial symmetric (interface) defect. This axial symmetry, though, is only seeming as it is seen to disappear for increasing T (see Fig. 3.6). Rather, as mentioned before, it stems from an 'artifact', i.e., spatial defect distribution dependent demagnetization –more precisely, due to a macroscopic (sample) shape effect. Demagnetization effects on physical properties are well known, such as in relation with ferromagnetic and superconducting matter [254, 255, 256, 257]. Its impact and appearance is set by a combination of applied magnetic field direction, sample, shape, and magnetization. Anisotropic demagnetization is characteristic to magnetic samples of irregular shape put in a uniform magnetic field $\overrightarrow{B}$. The non-uniform surrounding results in an effective (local) field dependent on the direction of $\overrightarrow{B}$, emerging, e.g., in ESR, as angle dependent g_c values.

The main, most direct, hint to the influence of demagnetization comes from the g_c-vs.-T plot (Fig. 3.6), pictured in the current case as arising from a system of paramagnetic defects densely packed over a thin layer, i.e., a disk-shaped sample configuration. For such elemental case, for $\chi(T) << 1$, the effect is found to result in (SI units) [35]:

$$g_c(T) = \begin{cases} g_{\rm ref}[1 + \frac{1}{2}\chi(T)], & for \overrightarrow{B} \perp \overrightarrow{n} \\ g_{\rm ref}[1 - \chi(T)], & for \overrightarrow{B} \parallel \overrightarrow{n}. \end{cases} \tag{3.3}$$

Combining Eqs. (1) and (3) (taking $T_C = 0$, as inferred above) results in self consistent successful fitting (curves in Fig. 3.6) of the T dependence of g_c for both field orientations, from where the values $g_{\rm ref} = 2.00259 \pm 0.00005$ and $N_V = (2.6 \pm 0.2) \times 10^{20}$ cm^{-3} are inferred. While the former value is in accordance with the direct RT X-band result, the later is consistent with the value ($\approx 3 \times 10^{20}$ cm^{-3}) obtained from direct ESR defect density measurements and the SRIM width (∼89 nm), demonstrating internal consistency.

At such an elevated unpaired electron concentration, the mutual defect interaction is no longer negligible. In the case of randomly distributed diluted centers of spin s = 1/2, when less than 1% of the lattice sites [258] have an unpaired electron, as S centers here, dipolar interaction causes a (cut off) Lorentzian line shape broadening of width [259, 260]

$$\Delta B_{pp}(G) = 0.54 \times 10^{-19} \times N_V(cm^{-3}) \tag{3.4}$$

where a factor of 2/3 has been incorporated to account for (evidenced) g anisotropy [259]. Accordingly, the above encountered N_V value would entail a dipolar line width contribution of ≈ 14 G, significantly larger (∼5 times) than that of the intrinsic S signal ($\Delta B_{pp} \approx 2.6$ G) previously reported [261] for diluted systems and clearly unlike the narrow signals ($\Delta B_{pp} \approx 2.1$-2.5 G) currently observed as well. Yet, at high local spin densities, exchange interactions narrow the resonance response towards the apparent width [262, 263] $\Delta\omega = \omega_p^2/\omega_e$, where ω_p is the root-mean-square of the dipolar perturbation and ω_e the exchange narrowing, all in frequency units. If sufficiently rapid the exchange-induced interactions *inhomogenously* average out the dipolar field seen by a spin [264] resulting in a Lorentzian [258] line shape. Movaghar et al. [260] showed that for a density of ∼10^{20} cm^{-3} D centers [24] in a-Si the exchange interaction prevails, completely narrowing down *dipolar and hyperfine interactions*. Obviously, as we are dealing with defect densities $N_V \approx 2.6 \times 10^{20}$ cm^{-3}, it is clear that exchange-narrowing may well account for the observed narrow S signal of Lorentzian shape with collapsed hf structure.

As can be seen from Fig. 3.5, all three as implanted samples exhibit almost equal Δg_c values, thus suggesting similar values for N_V, although [S] is found to be drastically lower in sample 2KU. This would indicate the S centers to be distributed over a thinner layer as a result of the UST compared to the untreated samples.

3.4.3 Influence of UST

The previous paragraphs have made it clear that, as expected, the densities of intrinsic paramagnetic defects are very high in the as-implanted reference samples. It is a general main drawback of the bare implantation technique, otherwise much versatile to increase the Si density in SiO_2. Reduction (elimination) of implantation damage has been the subject of intense research in various solid state fields, such as, e.g., semiconductor technologies [242, 244, 246]. In fact, the main objective of the current research is to evaluate the application of in situ UST as a method of suppressing implantation damage. Studying the influence of US on the ionic diffusion process in semiconductors, Krevchik et al. [244] concluded that the acoustic field disturbs the equilibrium state of the phonon subsystem, resulting in an energy exchange between nonequilibrium phonons and impurity atoms, thus decreasing the activation energy for impurity migration. Improved migration was also found by Franklin and Sengupta [246] based on stimulated Raman scattering and IR absorption measurements. Also, Ostapenko [242] found that UST applied to hydrogenated Si-based thin films is beneficial in improving defect recombination (annihilation) and transport characteristics of implanted species.

In the current work on the analysis of point defect generation, the superb positive healing effect of in situ UST during Si^+ implantation is immediately evident from comparing Figs. 3.1 and 3.2, showing the ESR spectra measured on samples without or with UST applied, respectively (same Si:P marker used for both spectra). Applying UST is seen to result in a $\approx 43\times$ decrease in [S], $\approx 6\times$ decrease in $[E'_\gamma]$, while IS is suppressed below the sensitivity limit (cf. Fig. 3.3). While UST appears not equally efficient for all three types of ESR centers, the effect is impressive, confirming the drastic impact of nonequilibrium phonons on implanted species and attendantly generated point defects. In particular, we note the influence on two of the main types of defects resolved, E'_γ and S center, which, as modeled, both essentially concern O-vacancy type centers: the drastic effect of UST on the occurrence of these centers, here clearly exposed by ESR to atomic detail, thus supports previous modeling [243, 244] where, in essence, enhanced mobility of displaced atoms will result in enhanced elimination of vacancies (Frenkel pairs).

There is one more noteworthy observation: Although the S centers density is decreased about 43 times as a result of applying UST, the ESR signal still remains affected by demagnetization, to a much similar extent. The net effect seems that, as a result of in situ UST, the defects are partially annihilated while the remaining gather into a thinner layer.

3.4.4 Influence of annealing

The ESR measurements on sample 3Kan, annealed at 1100 °C, show the presence of signals ($P_{b(0)}$, P_{b1}) typical [232] for nc-Si embedded in a-SiO_2 matrix. The powder pattern signals, showing up in the low field part of spectrum in Fig. 3.7 (top curve) pertain to Si DBs of P_b-type defects, the archetypal interface point defects in thermal Si/SiO_2. Here, as in Chap. 2, we should add that, since P_b and P_{b0} basically concern the same Si DB defect (close g matrices and line width), but pertaining at different interfaces, i.e., (111)Si/SiO_2, (100)Si/SiO_2 and (110)Si/SiO_2, respectively, their powder patterns are much similar. This makes undubious distinction difficult, from where the signal is denoted as $P_{b(0)}$.

As mentioned, P_b-type defects correlate with the Si/SiO_2 interface orientation, leading to field angle dependent signals (anisotropy). The fact then that the signals are powder patterns indicates that the nc-Si/SiO_2 interfaces are randomly oriented, as it might be expected for the amorphous matrix cannot instigate a *common* crystalline orientation for the crystallites grown in it.

Noteworthy is that, despite intensively searched for under various directions of $\overrightarrow{B}$, there appears within experimental accuracy no evidence of D centers [81], Si DBs in an a-Si environment. This would indicate that of all Si np's formed in the $SiO_{2(x)}$ matrix none, or only a negligible fraction, might have been left in the amorphous state. So, most, if not all, are crystalline, as in the case of the layered nc-Si embedded in a-SiO_2 prepared by the superstructure approach [265] detailed in Chap. 2.

Since the number of the embedded Si particles is not known from independent measurements, no further conclusions on occurring number of interface defects per Si particle can be drawn. Previous ESR measurements [232] on nc-Si embedded in SiO_2 obtained by high-T annealing (same as here) of SiO/SiO_2 superlattices found a closely one-to-one P_b-type defect-per-Si nc ratio. Assuming a similar nc-Si/SiO_2 interface quality in the current case, we can estimate the order of Si nc's created at $\sim 10^{14}$ cm^{-2}. Finally, there is the signal ascribed to C impurities observed in sample 3Kan. This would mean that contamination occurred in the as-grown state (and the corresponding signal may be masked by the intense S and IS signals) or introduced during subsequent annealing. But if sample 3Kan would have been contaminated by high-T annealing, sample 2KUan should exhibit the C signal in a comparable density as well since the two samples have been annealed physically together. Yet, as the latter sample shows no C signal but only a weak EX signal ($[EX] = (2.3 \pm 0.1) \times 10^{11}$ cm^{-2}), we conclude that this impurification concerns a side effect of the implantation process.

The influence of in situ UST is stunning when comparing samples 3Kan and 2KUan as shown in Fig. 3.7 (a) and (b) respectively. For sample 2KUan only a faint EX signal remains and no P_b-type defects (cf. Fig. 3.7). Considering that the two

samples were annealed together, it would bear out the application of the in situ UST during Si^+ ion implantation as the only matter of difference. We also note that combination of UST with post-implantation high-T annealing (1100 °C; 1 atm. in N_2) almost results in the removal of virtually all ESR-active defects beyond the detection level. This ESR result is confirmed by the PL-vs-PES correlation made by Romanyuk et al. [248] on very similar samples. They reason that the 1.5-eV PL line originates from suboxide states at the nc-Si/SiO_2 matrix interface since both PL line intensity and the density of the incompletely oxidized states decrease after UST. Their conclusion that the interface between nc-Si and a-SiO_2 is sharper as a result of UST application is corroborated by the drop in ESR active P_b-type point defects seen here, indicating a better interface quality indeed. So, all measurements performed on this type of Si nc's embedded in a-SiO_2 matrix do agree in unison on the beneficial effect of the US treatment on suppressing implantation damage.

3.5 Summary and conclusions

A multi frequency ESR study has been carried out on the effect of in situ applied 9.5 MHz US excitation during the implantation of the SiO_2 layer of (100)Si/SiO_2 entities with 90 keV Si^+ ions. The UST, which is applied to promote Si nanoparticle nucleation and growth, has been found successful in previous work on Cu and Ag implantation, where the effect was attributed to enhanced diffusion of generated interstitials as a result of energy exchange with the defect system.

For the as-implanted state, significant densities of three types of paramagnetic centers are resolved including the well known E'_γ, a signal at g_{ref}(X-band) ≈ 2.00252 ascribed to S centers ($Si_nO_{3-n} \equiv Si^\bullet$; n = 1, 2), and an unknown signal, denoted IS, at $g_c \approx 2.0026$; the latter two, of comparable intensity, are the most intense, about 10× larger than $[E'_\gamma]$. As modeled, both E'_γ and S centers are O-vacancy type defects. The high-intensity S signal is observed to show demagnetization effects (field angle dependent g_c shift) characteristic for a disk-like sample shape. It points to an arrangement of a high local density of paramagnetic species over a thin layer, not unexpected for ion implantation damage in an insulator; a local density of $\approx 3 \times 10^{20}$ cm^{-3} is inferred. The signal susceptibility shows a closely Currie-type behavior, with $T_C = 0 \pm 1$ K.

On the basis of the paramagnetic defect criterion, the in situ UST is found to effectuate a substantial beneficial influence, that is, a drastic reduction in S and E'_γ centers (∼43 and ∼6 times, respectively), with elimination of IS beyond detection: UST establishes an impressive healing effect, here demonstrated quantitatively, by in situ furnishing of nonequilibrium MHz phonons. It provides atomic evidence for previous modeling where, in essence, the US activation would, via the modified

phonon system, give rise to enhanced mobility of displaced atoms with enhanced annihilation of *vacancies* as a result.

As expected, post-implantation high-T (≈1100 °C) annealing, intended to from embedded Si np's, ensued a substantial defect repairing effect, with elimination of the three dominant types of defects (E'_γ, S and IS) beyond ESR detection. Instead, 4 other types of signals, albeit in much lower (orders of magnitude) density emerge, including the P_b-type Si/SiO_2 interface centers, EX, and a weak component ascribed to C impurification. Next, combination of UST with post implantation annealing is found to result in removal of virtually all ESR active centers ($\lesssim 2 \times 10^{11}$ cm^{-2}), with only a faint EX signal remaining. The total point defect (suboxide states) density drop as a result of UST application is independently confirmed by PL and PES measurements [248]. The beneficial influence of UST is thus found retained after additional high-T annealing: combination of in situ UST with post-implantation high-T annealing emerges as a highly efficient means to remove/prevent implantation damage in terms of intrinsic point defects.

Chapter 4

Multi-frequency ESR analysis of the nature of the E'_δ defect in a-SiO_2

4.1 Introduction

Driven by its impressive range of favorable and superb physical and chemical properties, SiO_2, in various forms, has been providing over history a virtual unlimited number of highly functional applications: to name a few, this ranges from it serving as the basic material for low-loss optical fiber waveguides to serving for decades as the basic still unprecedented, high quality gate insulator in Si-based electronic devices where it is incorporated starting from the straightforward thermally grown Si/SiO_2 entity [266]; it has made a-SiO_2 probably the most studied oxide so far.

By their nature, various physical properties are, to some extent, affected by structural imperfections, such as point defects. In the case of optical fibers, they may unacceptably impair photonic transport through optical absorption [131], while in the case of serving as gate insulator in complementary metal-oxide-semiconductor (MOS) devices, they may behave as detrimental charge traps, thus deteriorating the performance of MOS devices.

Glass, unlike metals or crystals, has a random organization by nature thus being less prone to irradiation damage since its structure cannot be altered radically. High-purity vitreous (v-) silica, and optical fibers made from it, are thus candidates for use under conditions of strong irradiation, including nuclear and thermonuclear

reactors. When highly purified, the induced optical loss level in SiO_2 is basically defined by the irradiation induced concentration of intrinsic defects in the glass-forming SiO_2 network [267].

In the recent years, scientists have been trying to merge SiO_2 photonics with Si-based CMOS (complementary metal-oxide-semiconductor) technology in order to obtain *all-Si-based electronics*, avoiding thus the trouble of introducing other materials into the CMOS fabrication processes. Candidates include Si nanocrystals embedded in a-SiO_2 as the precursors of quantum computers, Si-based LED's (light emitting diodes) and flash memories. The products of Si technology are being used on ground, under water and in space, being subjected to the deliberate (e.g., light propagation through optical fiber) or environmental irradiation which creates defects, resulting in device degradation. Silica is also involved in nuclear waste management where it is heavily attacked by radiation over long periods of time.

A particular class here are comprised of the intrinsic O-vacancy related point defects in silica, referred to as the family of E' centers as detected by electron spin resonance (ESR). This technique has proven to be a most adequate tool for point defect investigation of SiO_2 since 1956, when R. A. Weeks [82] first reported a paramagnetic center in neutron-bombarded quartz and fused silica, termed E'_γ. By drawing dry a-SiO_2 into fibers, defects identical [104] to the ones created by irradiation are produced, that is, Si-O or preexisting Si-Si bonds can break and result in E' center creation [105], i.e., mechanically induced atomic rearrangement (disruption).

From extensive experimental ESR and theoretical studies, the generic entity [40] of the E' class of defects has been identified as the three-fold coordinated Si entity (O3≡$Si^\bullet$, the dot representing an unpaired electron in a sp^3-type orbital) at the site of an O-vacancy. There are different variants both in crystalline (c-) quartz (E'_1, E'_2, E'_4, ...) and a-SiO_2 (E'_α, E'_β, E'_γ, E'_δ, and E'_s) with properties reviewed in several comprehensive works [9, 102, 268]. While several centers are accepted to be reliably atomically identified, the definite atomic nature of the variant observed in a-SiO_2, E'_δ, is still elusive [269].

In tracing atomic identification, a key role is played by resolved ESR hyperfine (hf) structure, E'_δ showing one hf doublet of splitting ∼100 G compared with ∼420 G for the 'strong' doublet (hf doublet with largest splitting) of the E'_γ center. No counterpart center has so far been reported in c-quartz nor has the E'_δ been observed in standard thermal oxide. Besides the particular magnitude of measured hf splitting (hfs), correct atomic modeling hinges on knowledge of the correct relative intensities of observed hf signals, which unlike the former (E'_γ), is still a subject of dispute [269] for E'_δ.

The atomic identity of E'_δ is the subject of current work. The E'_δ point defects were concluded to have a detrimental effect on device performance [115, 270], the defects being observed in buried oxides as well as in bulk silicas. Over the 25 years

since its discovery by Griscom and Friebele [41], four atomic models have been proposed, all based on a central unpaired sp^3 Si orbital, with direct Si involvement varying from 2 to 5 Si atoms (vide infra); in shorthand, we will denote these as Si_n (n = 2-5). Yet, a unique model could still not unambiguously be assigned [269, 271, 253].

In a later report on the subject, based on proper first-derivative absorption ESR spectroscopy, Buscarino et al. [272] disqualified the Si_2 atom model but, limited by experimental results, could not definitively distinguish within experimental accuracy between the advanced Si_4 and Si_5 atomic models.

The scope of the current work is to address the E'_δ hf structure in pertinent detail through a broad multifrequency continuous wave (cw) ESR study carried out at both low and high temperature (T). In this way, it is intended, on the basis of providing a meaningful statistical averaged set of data on the relative intensity of the resolved ^{29}Si hf structure (i.e., equivalent Si sites involved) inferred through orthodox cw first harmonic ESR absorption spectroscopy, a solid ground for decisive E'_δ atomic modeling. As a major finding, the results point to a 5(4)-Si shell, thus clearly refuting the Si_2 atom dimer model.

Relatedly, within the context of the presumed (singly) positive charge state of the E'_δ when ESR active [115, 118, 116], attention is paid to the positive influence in E'_δ appearance of charge compensator units, revealing a positive correlation with co-present Al E' centers. The results are discussed within the current state of theoretical modeling.

In the next section, we discuss the known salient E'_δ properties relevant for the current study, as obtained majorly from ESR experimenting and theoretical work. Experimental details are presented in section III, followed by the presentation of the experimental results and interpretation. After discussion of the results in section V, conclusions and final remarks are given in section VI.

4.2 ESR work and current theoretical insight

The E'_δ defect was first reported by Griscom and Friebele [41] in 1986, when studying by X-band ESR the influence of different 100 keV x-ray irradiation doses applied at 77 K as function of isochronal anneals in plasma deposited Cl-rich synthetic O-deficient (type IV) silicas of low OH content. The E'_δ signal was observed as an almost isotropic, narrow signal of peak-to-peak width $\Delta B_{pp} \approx 0.65$ G and a zero crossing value $g_c \sim 2.0020$ (i.e., principal g values inferred as $g_1 = 2.0018$, $g_2 = g_3 = 2.0021$, referring to axial symmetry), with an associated strong hf doublet split by 100 G where the correlated nature of the hf doublet was concluded from the similar activation and bleaching behavior as the main central Zeeman line.

This has undubiously been confirmed in later work [119, 271]. Because the defect appears to share one principal g value (g_1) with the traditional E'-type centers (E'_α, E'_γ), it has been adopted as another species of the E' defect family as the δ variant. In that work, the intensity of the E'_δ associated hf doublet appeared too small to be measured properly in the unsaturated first harmonic detection mode. Yet, based on its observed similar saturation behavior as E'_γ, considerations about relative signal intensities were carried out based on comparison of observed *amplitudes* of first-derivative spectra of the central Zeeman signals and high-power second harmonic out-of-phase hf spectra -a not straightforward procedure (see below). For annealing above ∼200 °C, the amplitudes of the 100-G doublets were found to correlate well with the amplitude of the E'_δ central line. The hf splitting associated with E'_δ of ∼100 G is about one fourth of the normal 420 G splitting of the primary E'_γ hf doublet [40], which can be envisioned as resulting from the E'_δ electron being *delocalized* over several (four) Si atoms. This finding, together with the nearly isotropic property in addition to the presumed involvement of Cl impurities in the atomic structure, led to the idea of a delocalized E'-type defect [41]: the E'_δ center was tentatively modeled as a SiO_4 vacancy dressed with 3 Cl atoms, with the unpaired spin delocalized over 4 Si atoms. Thus, its precursor is seen as a SiO_4 vacancy decorated by 4 Cl atoms bonded the 4 Si atoms (Si_4:Cl model), from where a Cl atom has been removed by irradiation.

Besides atomic chlorine, another defect first observed in this work was a triplet state (electron spin S = 1) bi-radical, with an associated signal observed at half the resonance field ($g_c \approx 4$) of the E'_δ centers. The appearance in the same materials and the similar response to annealing and irradiation indicated a correlation between the occurrence of the S = 1 state and E'_δ defects referring to similar precursor structures at their origin. Accordingly, this S = 1 defect was modeled as an SiO_4 vacancy now decorated by only two Cl ions, wherein two unpaired spins are localized in dangling sp^3 orbitals at different Si atoms of the cavity. The signal is removed [41] by a 10 min anneal at T ≥ 200 °C.

From X-band ESR studies of the influence of ^{60}Co γ-irradiation on a variety of high-purity bulk a-SiO_2 samples, both before and after room temperature (RT) and 500 °C treatments in H_2, Tohmon et al. [117] concluded that Cl (nor F) is not a prerequisite for E'_δ center formation. Yet, from correlated infrared absorption measurements, they concluded the necessity of O-deficiency, from where it was advanced E'_δ to be an O-deficient center. So, with no impurity involvement, as alternative model they suggested an ionized single O-vacancy with the unpaired electron rather evenly delocalized over the two neighboring Si atoms (Si_2; a charged Si-Si dimer), as pictured in Fig. 4.1(a), for the positive charge state. In the same scheme, the attendantly observed triplet state (S = 1) defect was assigned to two neighboring E'_γ centers (≡$Si^\bullet$ $^\bullet$Si≡) with the two unpaired electrons having the same spin direction.

In a later extensive ESR study on Si/SiO_2 device structures [118], Vanheusden

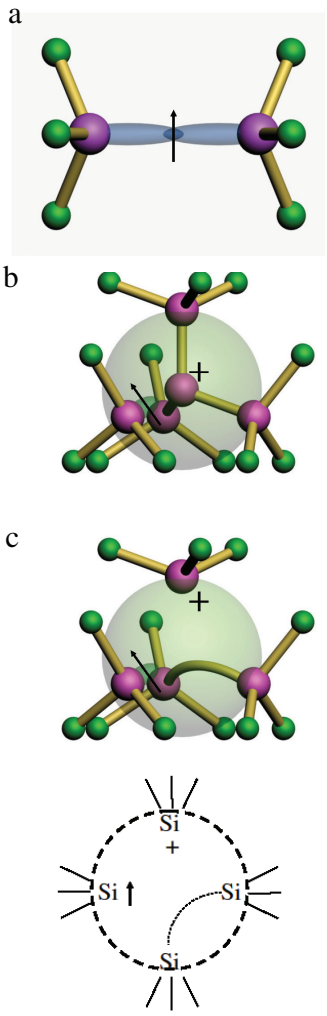

Figure 4.1: Ball-and-stick pictures of the models proposed for the E'_δ defect: (a) The Si_2 dimer where the unpaired electron spin density is predominantly delocalized between the two neighboring Si atoms, each backbonded to three oxygens of the SiO_2 matrix; (b) The Si_5 tetrahedral Si-cluster model, where the overlapping sphere suggests electron spin delocalization over the cluster; (c) The Si_4 cluster model with added a 2-dimension schematic. The dotted bow suggests dynamic (weak) bond formation. As denoted, all three models in the ESR active state represent a net charge of +1.

and Stesmans observed E'_δ centers in buried Si oxides (BOX) fabricated using the separation by implantation of oxygen (SIMOX) technique in (100)Si, the virtually Cl and F-free nature of these SIMOX oxides herewith directly disqualifying these impurities as key part of the E'_δ structure. The center is observed after ^{60}Co γ-irradiation [273], yet more outspokenly after exposure of the BOX to cathodic dc glow discharge Ar plasma treatment [118, 274]. Pertinently, as to the later Ar activation procedure, the E'_δ signal drops drastically after 10-min vacuum anneal at 200 °C, and could not be observed after reoxidation of the BOX nor, as expected, in conventional thermally grown oxide, pointing to E'_δ defect generation from specific precursor sites. It was also observed that the highest E'_δ density is obtained in the cathodic Ar bombardment configuration [118], indicative of a positively charged point defect, a hole trap, in agreement with other work [115, 116]. Moreover, depth profiling indicated enhanced E'_δ generation in regions of enhanced excess of Si, i.e., in the box layers ($\lesssim$100 nm) near to the interface with the Si substrate, unlike E'_γ centers which are produced more uniformly over the BOX. The results led to the proposal of an alternative E'_δ microstructure based in the existence of Si clusters, more precisely, the presumably positively charged Si_5 (see Fig. 4.1(b)) model where the unpaired electron delocalizes over the four Si atoms (perhaps) tetrahedrally configured around the central Si atom -in different views, basically a SiO_4 vacancy substituted by a single Si atom, or four O-vacancies clustered around a Si atom, or Si 'tetrahedron'.

In a related ESR work [275] comparing the generation of E'_δ centers in BOX by different methods, it was found that while energetic photons (x, γ) and ion bombardment activate the usual E'_δ center of axial (albeit weak) symmetry of $g_c \approx 2.0019$, hole injection combined with VUV excitation results in the generation of a (highly) isotropic type of $g_c \approx 2.0021$, termed $E'_{\delta 2}$. It indicated the E'_δ generation to be damage-agent specific. The E'_δ signal is also observed to bleach over time in room ambient (over ∼one day after hole injection; ∼weeks after dc glow discharge).

The E'_δ center was also observed [33] in ∼66-nm thick thermal grown a-SiO_2 on (100)p-Si (1000 °C; 1 atm dry O_2), reaching a maximum density of $\sim 3 \times 10^{11}$ cm^{-2}, when annealed in oxygen-free ambient at 1130 °C. The center is observed together with E'_γ, EX, and S centers generated as a result of oxide degradation effectuated by Si/SiO_2-interface initiated volatile SiO formation [276, 277].

Zvanut et al. [278] observed E'_δ center formation in x or ^{60}Co γ-irradiated BOX prepared either by thermally growing a thin oxide layer on Si and subsequent overlaying by polycrystalline Si followed by an annealing step, or in SIMOX, drawing the attention that the oxide fabrication technique is not influencing on its own the defect generation but rather the burying (O-deficient) aspect. As interpreted, out-diffusion of oxygen from the silica [279, 280] layer as volatile SiO molecules [278] created by the reaction of SiO_2 with Si (from the coating layer) during the high temperature anneal, is creating an O-deficient zone housing the E'_δ precursors. In fact, it resembles much the effect of the high-T annealing in O-free

ambient, referred to above.

In a later report, M. E. Zvanut et al. [281] observe that the defect density remains unchanged whether the samples are annealed in dry N_2 or O_2, and conclude that the removal of hydrogen, not oxygen, from the anneal ambient is essential for defect formation, but ambient moisture does not affect the annealing kinetics of E'_δ. This can be correlated with previous reports in which the H was concluded to break Si-Si bonds [117]: while irradiating the sample, the H was stripped from the structure and E'-type defects were created.

In ESR-based point defect identification, spectral hf structure plays a crucial role, to such extent that no defect can be considered reliably atomically modeled if not supported by insightfully assigned spectral hf properties, underlaid by theory. This includes hf spectral structure, hf splitting and, not the least, the relative ratio of respective signals, the latter reflecting the distribution of the unpaired electron wave function (spin density) over the defect's constituent atoms -not always paid sufficient attention to if limited ESR sensitivity. The ratio $R_{hf}(\eta, n)$ of the intensity of a hf multiplet ($\mathcal{I}_{hf}$) to that of the central main (Zeeman) signal ($\mathcal{I}_c$) is a function of η, the natural abundance of the hf-originating nuclear isotope, and n, the number of such atoms in a shell of equivalent atom sites the unpaired spin is interacting with. With η known, n provides a basic clue to convincing atomic modeling. Invariably, the correct orthodox way to determine signal intensities (area under the absorption curve $\propto \chi$") is from non-saturation conventional first harmonic ESR spectroscopy. But when in lack of sensitivity or overwhelmed by hard-to-disentangle overlapping signals, it is tempting to turn [41] to the high-power second harmonic phase-quadrature detection mode (saturation spectroscopy), which has been shown empirically to be generally a much more sensitive means to resolve hf structure for point defects in silica and oxides [14, 15, 102], among others, due to the high saturability of such defects. Under appropriate experimental conditions for a certain defect, the second harmonic saturation spectra appear identical to the direct absorption shapes (χ"), as evidenced empirically [14, 15]. So, in principle, besides revealing spectral composition, the former spectroscopy may be conventionally used for signal lineshape analysis. However, the intensity of second harmonic spectra depends in a complex manner on the relaxation times of the defects as well as on various experimental parameters such as modulation frequency and amplitude, and applied microwave frequency and power, befogging quantitative analysis. Some means of independent calibration is required.

Using X-band ESR, Zhang and Leisure [119] addressed the hf structure of E'_δ centers generated by x-ray irradiation in high purity silicas synthesized by chemical vapor deposition (CVD) which allows impurity and moisture control. They observed E'_δ signals as well as an interconversion between E'_γ and E'_β depending on anneal treatment. As a major result, these authors were first to determine R_{hf} for E'_δ giving $R_{hf} = 0.175$-0.191, from where the value n=4 was extracted. While rejecting the Si_2 atom model, this led to the proposal of the revised model for E'_δ as being a

$[SiO_4]^+$ vacancy (Si_4 model; two strained nearby O-vacancy centers), i.e., essentially the initial Griscom and Friebele [41] model with no Cl (impurity) involvement, as depicted in Fig. 4.1(c). Pertinently, one more difference to be noted is the difference in net charge state, that is, 0 and +1 for the initial and revised model, respectively. Based on the n = 4 result, also the Si_5 model was deemed untenable, adding that it is highly unlikely that such clusters would be present in the studied fused silica.

There is a similarity between the E'_δ model proposed by Zhang and Leisure [119] and that of the EX center proposed by Stesmans and Scheerlinck [124], both starting from the existence of the OH-decorated SiO_4 vacancy in α-quartz [282]. While the E'_δ defect is centered on a SiO_4 vacancy where the unpaired electron is delocalized over the surrounding 4 Si atoms, the EX is centered on a Si vacancy. The delocalized unpaired electron in the EX model shows hf interaction with a shell of 4 (inequivalent) O atoms and a superfine interaction with a Si_4 shell.

The three models, Si_2, Si_4, and Si_5, thus far proposed for E'_δ have been evaluated by Karna et al. [121] using first-principles quantum mechanical calculations concluding that the E'_δ center is a symmetric variant of E'_γ, i.e., symmetrically relaxed O monovacancy, also referred to as the Si dimer configuration (Si_2) of the positively charged O vacancy in SiO_2. In α-quartz, it is known as the short Si-Si distance ($\sim$2.7 Å) variant [283, 284] of E'_1 in near-perfect crystal (NPC) equilibrium symmetry [283]. Its properties have been addressed in various theoretical works [120, 121, 269, 283, 285, 286]. The E'_δ hf structure consists of a single doublet of which, as turns out, the splitting is physically determined by the isotropic Fermi-contact part (within experimental accuracy, no anisotropic contribution could be sofar been isolated from simulations of the observed powder patterns) generally given as $a_{iso} = \frac{2}{3}\mu_0 g_N \beta_N g_e \beta |\Psi_s(0)|^2$, where g_N and g_e are the nuclear and electron g factors, β_N and β are the nuclear and Bohr magneton, and μ_0 the vacuum permeability; $|\Psi_s(0)|^2$ is the unpaired spin density (s part) at the interacting nuclei, here ascribed to ^{29}Si isotopes (nuclear spin I = $\frac{1}{2}$; η = 4.67 %). Spin density calculations [120] indicate that the unpaired electron is not delocalized over the entire cluster but preferentially on a single Si atom in case of the "Si_5" model or on (between) a single pair of Si atoms for the other two cases, reducing the s-orbital contribution on the Si nuclei. The symmetry reduction of the electronic wavefunction when considering the Si_4 and Si_5 tetrahedral clusters was attributed to a dynamic Jahn-Teller effect. Molecular calculations [285] show that the main difference between positively charged E'_δ and E'_γ point defects is reflected in the distance between the two constituent Si atoms: if the Si-Si distance is small enough the two potential wells combine into a single one and an E'_δ center is obtained.

The E'_δ defect has initially been associated with the Si_2 dimer on the basis of the calculated hf splitting of 100 to 135 G [120, 287]. It has since been supported by various theoretical works [269, 286]. The E'_δ has been described as a metastable non-puckered form of the E'_γ, the later one being perhaps a few tenth of meV more

stable. But as to a-SiO_2, this is still in dispute [93, 288]. Other theoretical work [289] has concluded that the positively charged Si dimer is the stable configuration for ∼80% of the O vacancy sites. Later work [290] addressing spectroscopic aspects of E'_δ has calculated the principal g matrix values ($g_1 = 2.0018$, $g_2 = 2.0034$, $g_3 = 2.0043$), which are found in good agreement with initial experimental results [41] ($g_1 = 2.0018$, $g_2 = g_3 = 2.0021$). The optical absorption energy for E'_δ was calculated as 6.33 eV, to be compared with the known value of 5.8 eV for E'_γ.

In recent theoretical work [269], Tuttle and Pantelides studied Si clusters in a-SiO_2 described as arising from vacancy clusters n(V_O), with n in the range 1-7: (a) Based on the calculation of the formation energy per Si-Si bond, it is found than the Si_5 cluster (4 O-vacancy cluster) is the most stable, significantly (∼0.23 eV per Si-Si) more favorable to form that the Si_2 dimer. Yet, while theory would thus favor V_O clustering, it was considered not to become necessarily expressed that way in practice due to silica growth conditions. (b) Comparable isotropic hfs values are found, given as ∼100 G for Si_2, with a somewhat broader range of 80-120 G for the Si_5 model. (c) Based on additional considerations about g value anisotropy, it is concluded that the Si_2 defect is the favored candidate for E'_δ, herewith declining the yet solid experimental counter result on equivalent Si sites participating in $a_{\rm iso}$ provided by Buscarino et al. [271] (see below).

Buscarino et al.[271] were first to detect the E'_δ hf structure in the first-harmonic ESR detection mode using RT X-band spectrometry. The maximum E'_δ density of $\approx 2 \times 10^{16}$ cm^{-3} was reported for an a-SiO_2 type-I sample Pursil 453, ^{60}Co γ-irradiated at RT to a dose of 1000 kGy, subsequently annealed isochronally (∼25 min) up to 580 K. Saturation in E'_δ production is observed for doses above ∼5000 kGy, while E'_δ is observed to increase for $T_{\rm an}$ increasing in the range 520-580 K and to decrease for higher $T_{\rm an}$ [271, 291]. The inferred value $R_{hf} = 0.16$ was concluded to be compatible with Si_4 and Si_5 configurations, while the O monovacancy dimer model was ruled out. Yet, their observations appear hampered by co-existing numerous other interfering signals from centers such as E'_γ, E'_α, $[AlO_4]^0$, and E'_{74} ascribed to $O_2H{\equiv}Si^\bullet$ variant [15, 128, 129, 292] of E'_γ (showing a 74-G split doublet) which may urge more experimental substantiation. Following the defect density dependence on $T_{\rm an}$, above 500 K a hole transfer from the $[AlO_4]^0$ centers to the precursors of E'_γ and E'_δ centers can occur. The E'_γ and E'_δ centers show similar relaxation properties evidenced by the similar saturation behavior of their main hf doublets [293]. It is also suggested that both E'_γ and E'_δ centers can be used to characterize the O deficiency of the SiO_2.

4.3 Experimental details

4.3.1 Sample preparation

The samples investigated are all commercial low OH content fused quartzes: PH 370 [294], KI [295], Infrasil 301 [296], KUVI [295], Suprasil 300 [296], Suprasil 311 [296]. We succeeded to activate E'_δ signals only in the first three glasses, while, in the other, it was difficult to activate any defect at all. According to the supplier, the sample KI has total metallic impurity content (including Al) < 15 ppm and OH content ≤ 0.2 ppm; the KUVI one is specified as metallic impurities content ≤ 0.1 ppm, [OH] ≤ 0.1 ppm and [Cl] ≤ 0.2 ppm. Sample PH 370 is a low alkaline content fused quartz that came from the manufacturer in the shape of tubes of $\sim$10 mm diameter and $\sim$7 mm thick walls, the other three glasses were 2-4 mm thick plates. Suprasil samples contain $\sim$1 ppm OH, ≤ 0.01 of Na and < 0.01 ppm of Al. Since the sample volume that can be introduced into the ESR cavity is limited, the glasses were cut into thin slices of size $\sim 0.1 \times 2 \times 10$ mm^3 used for VUV treatments and bars of $\sim 2 \times 2 \times 10$ mm^3 used for UV and γ-irradiation.

After cutting and before any other treatment the silica pieces have been etched in aqueous HF (5 % HF in H_2O by volume) to remove cutting damage. In some case, the etching was also used to thin down slices to desired thickness. To ESR activate defects, different samples have been subjected to three types of irradiations: room ambient vacuum ultraviolet (VUV) (10-eV photons, flux $\sim 10^{15}$ cm^{-2}s^{-1}) and UV (1.2-6.8 eV range) irradiation was applied using MgF_2-windowed Kr discharge lamp and 150-W Xe arc lamp, respectively. As the penetration depth of VUV photons in a-SiO_2 is $\sim$10 nm [297, 298], the effective sample area is enhanced by stacking thin slices irradiated both sides. The ^{60}Co γ-irradiation was performed at 30 ± 5 °C in dry air at a rate of 40 kGy/h to doses between 20 and 1200 kGy, most samples being irradiated up to 20, 80, 200, 500 kGy, labeled as R1, R2, R3, and R4, respectively. All irradiations were performed in room ambient at RT. Before γ-irradiation part of the KI, KUVI and Infrasil 301 samples were annealed in vacuum ($< 4 \times 10^{-6}$ Torr) at 1175 °C for $\sim$170 min, with the aim to desorb hydrogen (OH groups) from the oxide. Some of the irradiated samples have been selectively treated at desired temperatures in the range 50-346 °C, either in room ambient or Ar, typically for $\sim$8 min.

4.3.2 ESR spectroscopy

ESR spectra were taken at three different microwave frequencies, i.e., X- ($\sim$9.0 GHz), K- ($\sim$20.5 GHz) and Q-band ($\sim$34.0 GHz), operated in the T range 4.2-300 K using a Q-band commercial Bruker EMX and locally constructed K-band spectrometer, the latter providing the best sensitivity at low T. Depending on

the observational T, X-band observations were made either using a Jeol JES-FA 100 spectrometer (RT investigations) or a locally designed one optimized for low T (liquid He) measurements. All four spectrometers were driven in the adiabatic mode. Routinely, conventional cw low-power first derivative-absorption (dP_μ/dB) spectra were detected through applying sinusoidal modulation (∼100 kHz; amplitude $B_m \geq 0.08$ G) of the externally applied static field $\overrightarrow{B}$, and were complemented with saturation spectroscopy –high-power second harmonic dispersion mode– measurements (see e.g., Ref. [14]) to disentangle overlapping signals and probe signal lineshape.

While generally beneficial for signal sensitivity (Boltzmann factor, noise level, etc.), low-T measurements often suffer from enhanced signal saturation (distortion) effects with decreasing entropy, which requests appropriate reduction of the incident microwave power P_μ, at times beyond spectrometer capabilities. This appeared a burden for the Q-band spectrometer where, for signals such as E'_δ, E'_α, and E'_γ, the operational P_μ could not be sufficiently reduced to take the signal intensity dependence on P_μ down to the linear range, not even at RT (although it may approach close enough not to induce signal shape distortion, but only intensity reduction), so extreme caution is needed with extracted absolute E' densities from those measurements.

Since most of the observed (central) signals are powder patterns, their width is changing with the microwave frequency used, so the value of B_m was adapted for each individual case to such levels causing no visible signal distortion. For the broader hf structure signals, we used larger B_m values of ≈1 G. The signal-to-noise ratio was improved by appropriate signal averaging, depending on the signal strength, even up to 10000 scans for a single spectrum of the hf structure.

Defect densities were determined through double numerical integration of the detected dP_μ/dB signals using a co-mounted point-like reference. Depending on spectral composition and/or ESR parameter aimed to isolate, this was a Si:P marker [18] ($S = 1/2$, $g = 1.99869 \pm 0.00002$ at 4.2 K), a Li:F marker [19] ($S = 1/2$, $g = 2.00229 \pm 0.00002$), or DPPH [20, 21] ($S=1/2$, $g = 2.00357 \pm 0.00005$ at RT), all three also serving as g-markers (attained accuracy $\pm 5 \times 10^{-5}$). Proper corrections for the actual relative positions of the sample studied and co-mounted marker in the cavity were taken into account to infer correct absolute intensities of detected signals.

Two simulation codes were used for ESR spectra analysis: Bruker Simfonia (based on perturbation theory, with manual parameter optimization) for E'-type centers, and a code based on exact matrix diagonallization (EPR-NMR; courtesy of J. A. Weil) for Al E' centers.

4.4 Results and interpretation

Here we expand the standard cw adsorption ESR research on the E'_δ signal in silica to multi-frequency observations at different temperatures to supply an extended and detailed set of data on the E'_δ center, in particular its hf structure. The a-SiO_2 samples have been subjected to different treatments in an attempt to maximize the intensity of E'_δ defects, both in absolute values and also relative to the co-present other signals.

4.4.1 E'-type defects

As to VUV irradiation, E'_δ defects could be generated only in three of the studied silica glasses: PH 370, Infrasil 301, and KI, henceforth referred to as the E'_δ-glasses. In fact we did not manage to activate E'_δ centers in KUVI samples with any of the performed treatments (not even after VUV or γ-irradiation combined with post irradiation thermal treatments), unlike previous reports by Buscarino et al. [293]: better results for KUVI than for KI glasses. This dissonance may simply have arisen from inadvertent exchange in sample labeling, but otherwise immaterial for the current study.

Shown in Fig. 4.2 is a typical RT Q-band spectrum of the near g $\sim$ 2 region measured on Infrasil 301 thin slices subjected to VUV irradiation of both sides for 14 h. The spectrum represents a superposition of three signals arising from point defects all intrinsic to a-SiO_2: E'_α, E'_γ, and the defect of interest, E'_δ, all being part of the E' defect family. Common for all defects of this group is a principal g-value $\approx$2.0018 and the fact they all appear associated with O-vacancy in a-SiO_2.

The favored model, underlayed by theory, pictures E'_1 as a positively charged (1+) asymmetrically relaxed $O_3 \equiv Si^\bullet \ldots {}^+Si \equiv O3$ unit [96, 97, 98, 299] at the site of an O-vacancy, that is, composed of an sp^3 hybridized Si dangling bond ($\equiv Si^\bullet$), and a positively charged Si back-puckered through its basal oxygen plane towards a lattice O atom that effectively takes 3-fold coordination [90, 91, 92, 93]. Based on observed ESR parameters, the E'_γ center is considered the closest analogue to the basic E'_1 center in α-quartz, although the complete model is still under dispute [95]. But while related to the same generic entity, the overall defect models in α-quartz and a-SiO_2 need not necessarily be the same. In fact, in thermally grown a-SiO_2 on Si, strong evidence has been provided [99, 300] for the E'_γ simply to concern the neutral $O_3 \equiv Si^\bullet$ unit, i.e., the generic entity of the E' group of defects.

An ^{29}Si hf structure of the E'_γ center in γ-irradiated a-SiO_2 was observed first by Griscom et al. [40] revealing a doublet with splitting of $a_{\rm iso} = 420 \pm 3$ G (in unstrained SiO_2), close to the value $a_{\rm iso} = 410$ G reported [86] for E'_1 indicating a

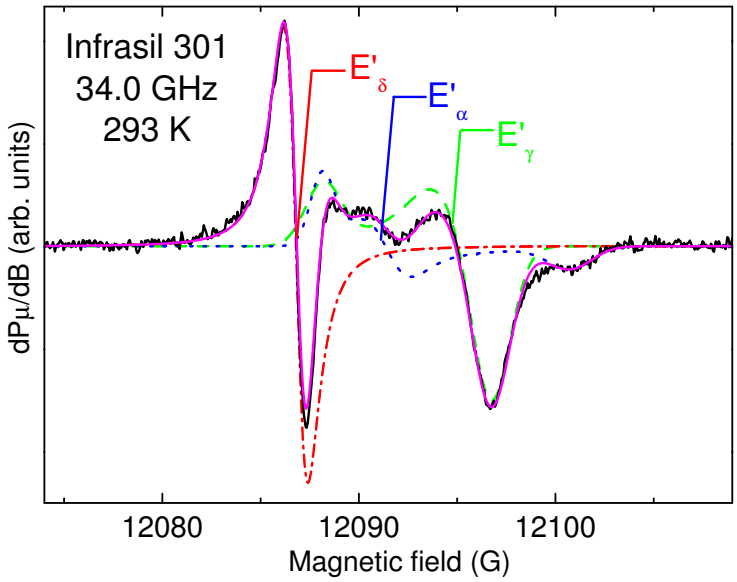

Figure 4.2: Q-band low power first harmonic spectrum (central Zeeman part; full curve) of the E' centers measured at RT on Infrasil 301 VUV irradiated for 14 h each side, using $P_\mu = 1.6 \times 10^{-7}$ W and $B_m = 0.4$ G. The superimposed continuous curve represents the optimized fitting result obtained as a weighed sum of the three constituent signals of which the Gaussian powder patterns fittings, E'_δ (dot dashed curve), E'_α (dotted curve), and E'_γ (dashed curve), using the parameters listed in Table 4.1 are also shown.

resemblance E'_γ to the E'_1 defect in α-quartz [88]. They also report an anisotropic [40] contribution $a_{\text{aniso}} \approx 22$ G to the hf coupling constant.

Griscom [100] first observed the E'_α signal in high-purity a-SiO_2 x-ray irradiated at 77K, showing $g_1 = 2.0017$, $g_2 = 2.0013$ and $g_3 = 1.9998$ and an associated ^{29}Si hf doublet of 420 G splitting, the same as for E'_γ. The asymmetry of the g matrix was supposed to arise from a Si dangling bond that has in a second neighborhood position an oxygen in a peroxy-like linkage, an atom that is displaced from its normal position as a result of irradiation. However, a recent report [107] revealed that the strong hf structure corresponding to E'_α is in fact a 490-G split doublet –not 420 G– with a g matrix similar as reported here (see Table 4.1); the successful discrimination compared to initial reports [100, 41] may have arisen from different defect activation treatments. The latest model [107] pictures E'_α as a hole trapped at an O-vacancy with the unpaired sp^3 Si orbital pointing away from the vacancy in a back-projected configuration and interacting with one more oxygen atom of the a-SiO_2 matrix [107, 108, 109].

Table 4.1: Inferred Q-band ESR parameters, using Gaussian convolution lineshapes of width ΔB_{ppi} along the respective g_i axes, from the optimized spectral simulations of the E'-type centers encountered in all three E'_δ glasses, either VUV or ^{60}Co γ-irradiated. A mild annealing step (320-350 °C) was applied to the samples γ-irradiated to maximally activate the E'_δ defect signal. The two different kinds of irradiations seem to introduce only slight variations in the simulation parameters.

Defect	g_1	g_2	g_3	ΔB_{pp1} (G)	ΔB_{pp2} (G)	ΔB_{pp3} (G)	irradiation applied
E'_α	2.0017	2.0012	1.9996	1.2	2	2.2	VUV
	2.0018	2.0009	1.9997	0.6	1.8	2.1	γ
E'_γ	2.0017	2.0005	2.0003	1.8	2.7	1.8	VUV
	2.0018	2.0005	2.0003	0.57	1.37	1.1	γ
E'_δ	2.0018	2.0020	2.0020	0.9	1.4	1.25	VUV
	2.0019	2.0020	2.0020	3	0.6	0.8	γ

As can be seen from, e.g., Fig. 4.2, showing a Q-band spectrum (near g = 2 range) observed on Infrasil 301 subjected to VUV irradiation (14 h both sides), the overlap of the E'_α, E'_δ and E'_γ signals makes disentanglement tedious, with consequent impact on the precision attained of the ESR parameters inferred through spectra simulation using the Simfonia software. Simulations of the central part of the observed E' defect spectra has been carried out for all three types of silica in which the E'_δ defect could be activated, and for both VUV and γ-irradiation treatments, using Gaussian convolution lineshapes. The inferred principal axes g values and applied Gaussian broadenings are listed in Table 4.1, where, consistently, the fitting parameters obtained per kind of defect and irradiation treatment are found to be equal within experimental error. As illustrated in Fig. 4.2, the experimental spectra could be accurately simulated, from where the defect densities listed in Table 4.2 are obtained. As to the PH 370 glass provided in the shape of tubes, there was no difference in of E'_δ defect appearances between inner and the outer surface subjected to VUV irradiation.

4.4.2 E'_δ optimization

The correct measurement of the E'_δ hf structure intensity using the mandatory first harmonic detection mode requires, for sensitivity reasons, utmost optimization of the E'_δ defect density. For this end, in a comparative manner, different irradiation treatments in combination with thermal steps have been explored.

The influence of VUV irradiation time on the induced E'_δ defect density was

Table 4.2: Inferred densities of observed E'-type centers in those vitreous silica samples in which the E'_δ signal could be activated by irradiation, together with some sample treatment specifications. As VUV is penetrating only a surface layer (∼10 nm) in contrast with γ-irradiation penetrating the whole sample body, the defect densities are specified in units of cm^{-2} (in blue) or cm^{-3}(in black), respectively. Where not specified, relative errors on the inferred densities are estimated ≤6 %. For the VUV irradiation, the indicated exposure time is per sample side.

Sample designation	Irradiation treatment	Additional anneal(∼336 °C air; 8 min)	$[E'_\delta]$	$[E'_\alpha]$	$[E'_\gamma]$	[Al E'][a]
PH 370	VUV (201 h)	-[b]	$(3.5 \pm 1) \times 10^{13}$	$(5.4 \pm 0.5) \times 10^{13}$	$(1.1 \pm 0.1) \times 10^{14}$	NA[c]
	γ (500 kGy)	-	$< 1 \times 10^{14}$	2.5×10^{16}	2.6×10^{17}	3.0×10^{15}
		+	9.6×10^{14}	2.9×10^{16}	2.1×10^{17}	NO
Infrasil 301	VUV (77 h)	-	$(7.9 \pm 0.7) \times 10^{12}$	2.6×10^{13}	$(1.9 \pm 0.2) \times 10^{13}$	NA
	γ (500 kGy)	-	$< 5 \times 10^{14}$	5.6×10^{16}	5.3×10^{17}	2.9×10^{15}
		+	$< 5 \times 10^{14}$	3.3×10^{16}	3.1×10^{17}	NO
KI	VUV (20 h)	-	1.4×10^{13}	7.9×10^{13}	4.0×10^{13}	NA
	γ (200 kGy)	-	$< 7 \times 10^{13}$	$< 4.7 \times 10^{15}$	2.8×10^{16}	NA
	γ (200 kGy)	+	$(1.1 \pm 0.1) \times 10^{16}$	$(2.9 \pm 0.2) \times 10^{16}$	$(4.0 \pm 0.2) \times 10^{16}$	NO
	γ (500 kGy)	-	$< 8 \times 10^{14}$	$< 9 \times 10^{15}$	4.1×10^{16}	4.5×10^{15}
	γ (500 kGy)	+	1.5×10^{16}	3.4×10^{16}	6.5×10^{16}	NO

[a] Though useful for relative comparison, the specified Al E' densities in absolute terms should be considered rather as indicative, as these are obtained assuming that the Al E' signal exhibits the same saturation properties as the strong E'_γ hf doublet.

[b] -: not applied; +: applied.

[c] NO: not observed; NA: not available

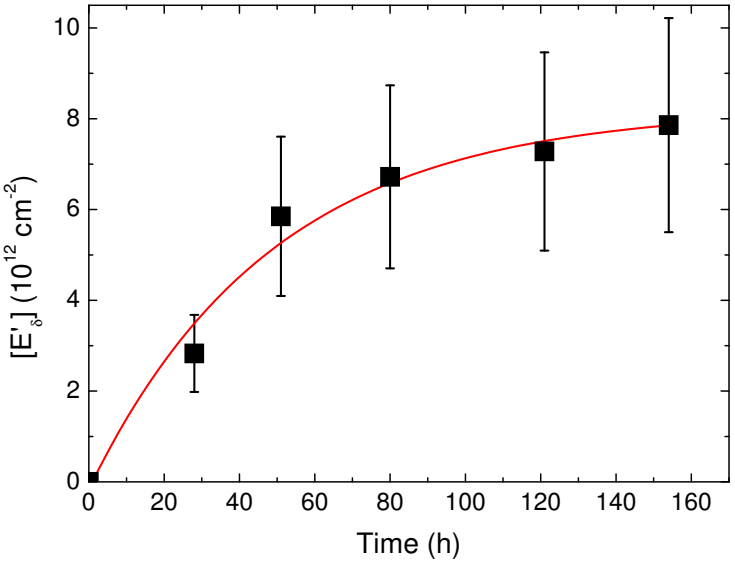

Figure 4.3: The evolution of E'_δ defect production as function of the total VUV irradiation time in Infrasil 301 glass. The curve is meant to guide the eye.

monitored for the three E'_δ glasses by Q-band measurements taken within maximum a few days after each irradiation step; Figure 4.3 shows the evolution for the Infrasil 301 sample. Left in room ambient, the E'_δ signals nor those of other E' centers was found not to change appreciably over months after irradiation. The E'_δ density in VUV irradiated samples could be somewhat improved by thermal treatment, yet not significantly.

Figure 4.4 shows some representative 200 G wide Q-band spectra (i.e., excluding the E'_γ and E'_α strong hf range) observed after extensive VUV irradiation for on the PH370 (t ∼201 h; bottom curve) and on KI (t ∼77 h; middle curve) glasses. As it offers generally a much enhanced signal-to-noise ratio in the case of highly saturable (low defect density) signals, the second harmonic saturation detection method is used here to optimally trace and reveal occurring hf structure signals. In the ∼100 G-splitting range, two main doublets, of 74 and 120 G splitting are observed, badly overwhelming the aimed for E'_δ hf structure of interest. The spectra here were normalized to the amplitude of the E'_γ (absorption like) signal for each sample.

The 74 G doublet centered at g ≈ 2.0016, stems from the E'_{74} defect [15, 128] is evidencing the silica to contain OH groups [129]. A doublet of ≈119 G splitting, associated with a defect of axial [126] g symmetry ($g_\parallel = 1.999 \pm 0.001$, $g_\perp = 1.992 \pm 0.001$), was modeled as an irradiation-induced impurity-related defect

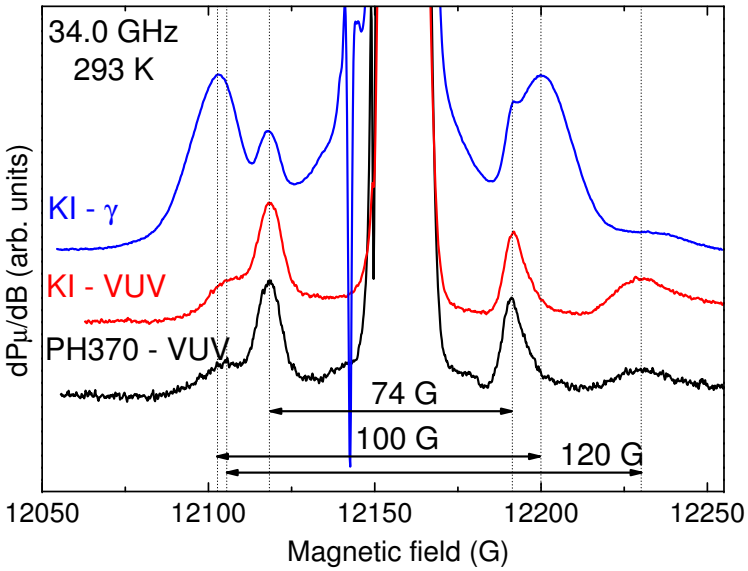

Figure 4.4: Comparison of representative high power second harmonic Q-band ESR spectra measured at RT using P_μ = 1.6 mW and B_m = 0.5-1 G on two types of silica samples subjected to γ (and subsequent anneal at 336 °C 8 min; air) and VUV irradiation. The spectra are enlarged to expose the hf structure in the neighborhood of the central E' main signals (blown up off scale in the center of the spectrum). The 120 G doublet, ascribed to a $O_2H{\equiv}Ge^\bullet$ defect, is quite intense in the VUV-irradiated samples spectra, while it appears relatively much reduced in the γ-irradiated sample. The 100 G-split EE'_δ hf doublet is clearly prominent only in the γ-irradiated sample spectrum. The 74 G-split doublet stems from the E'_{74} ($O_2H{\equiv}Si^\bullet$) defect.

which involves an electron trapped at a H-compensated Ge impurity in a-SiO_2 ($O_2H{\equiv}Ge^\bullet$). The signals of the 120 G doublet observed here as activated by VUV, measured in the unsaturated first harmonic mode (not shown), show similar asymmetric shapes as reported by Vitko [126], yet there is no indication of Ge in the suppliers's specifications of glass composition.

For the current purpose, the observations as illustrated in Fig. 4.4 immediately bear out the inadequacy of the VUV treatment for these kind of glasses, a situation which cannot be cured, not even by extended VUV irradiation times. Reliable extraction of the E'_δ-associated 100-G hf doublet appears virtually impossible, a situation even far worse for the first-harmonic detection mode method. So, VUV irradiation is concluded inadequate.

Also attempted was subjecting the E'_δ-glasses to UV irradiation, which is supposed to partially bleach the 74 G doublet [129]. While much deeper penetrating into the sample, unfortunately, UV treatment was found to activate only E'_γ and E'_α defects, in line with previous results [129, 301, 302]. We found no trace of E'_δ thus outright disqualifying UV irradiation for the intended purpose.

Separate samples of the three glasses that showed E'_δ signals after VUV treatment, were γ-irradiated with doses of 20, 80, 200 and 500 kGy: indeed, again an E'_δ signal was found to be generated in all three, albeit small in comparison to E'_γ and E'_α. Noteworthy, in the other glasses, γ-irradiated only to the highest doses, still no E'_δ signal could be observed. Thus only the three types of the investigated glasses appear prone to the E'_δ generation and by both VUV and ^{60}Co γ-irradiation. From the four applied γ-doses, the 200 kGy one seems to be the best in terms of E'_δ intensity relative to the E'_γ and E'_α signals and overall spectral appearance, although 80 and 500 kGy give satisfactory results as well. In an attempt to reduce the H-related 74 G doublet, also observed after γ-irradiation, some samples were vacuum annealed (1175 °C) before γ-irradiation, yet without ensuing any noticeable difference. In line with previous work [271], applying thermal treatment after γ-irradiation increases the absolute E'_δ-density drastically (orders of magnitude), as well as increasing its density relative to those of the (invariably) co-present E'_γ and E'_α defects. The former is demonstrated in Fig. 4.5 by isochronal annealing (8 min) results of the absolute E'_δ defect density in γ-irradiated (200 kGy) KI silica as function of $T_{\rm an}$, indicating that an optimum is reached for $T_{\rm an} \approx 326$ °C, similar to previous results [271]. This establishes the current optimum E'_δ generation method.

In Fig. 4.4 is shown a Q-band second harmonic saturation spectrum (top curve) observed on a γ-irradiated (200 kGy) KI sample subsequently annealed at ∼336 °C, where now the 100-G E'_δ hf doublet is clearly and intensely revealed, much enhanced (compared to the UV and VUV data) relative to co-present 74-G and 120-G doublets. Pertinently, the applied thermal step also eliminates at ones the S = 1 triplet state spectrum [41]. It opens the route for correct E'_δ hf structure analysis, i.e., signal disentanglement and correct intensity determination. In terms of the exposed 100-G doublet intensity, and hence overall E'_δ defect density, comparison of this spectrum in Fig. 4.4 with the middle one, observed on the sample KI material but subjected to VUV irradiation, immediately bears out the impressive superiority of γ-irradiation plus annealing in E'_δ generation. Here again we should stress the (drastic) influence of post-irradiation annealing, to such extend that in the as γ-irradiated state, the observed E'_δ signal intensities did not much exceed the VUV results.

Over all E'_δ-glasses, we also monitored the strong hf structure splitting of E'_γ and E'_α defects, reported to be $a_{\rm iso}$ ≈420 G [14, 40, 303], $a_{\rm aniso} \approx 20$ G [40] and $a_{\rm iso} \approx 490$ G [107] respectively. Optimized fitting (EPR-NMR software [304]) of the E'_γ and E'_α hf signals (powder patterns) using Gaussian convoluting lineshapes (width $\Delta B_{\rm pp} = 26.5$ and 45 G, respectively) gives the average hf matrix values

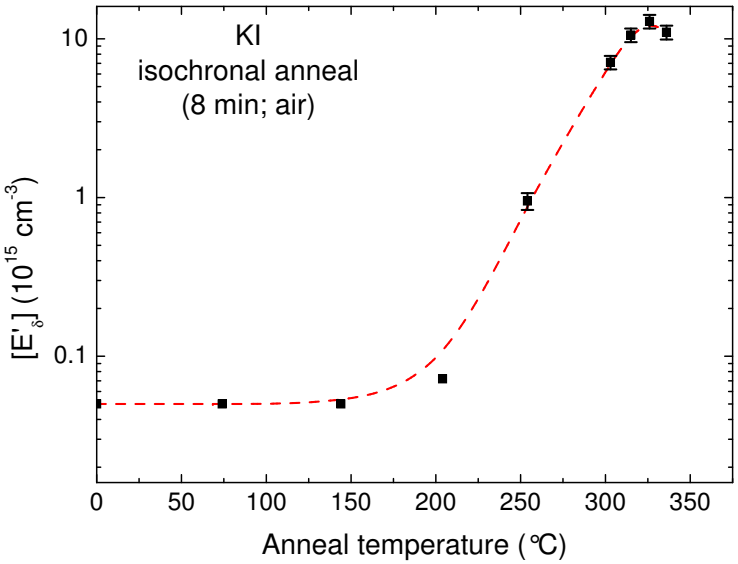

Figure 4.5: Variation of the E'_δ density for the 200 kGy γ-irradiated KI sample as a function of sequential 8-min isochronal annealing. The maximum density is obtained for ≈326 °C. Densities were determined from first harmonic Q-band spectra taken at RT. The curve guides the eye.

$a_{\rm iso} = 424 \pm 4$ G, $a_{\rm aniso} = 20 \pm 3$ G and $a_{\rm iso} = 455 \pm 4$ G, $a_{\rm aniso} = 20 \pm 3$ G for the E'_γ and E'_α defect, respectively. The substantial difference of the E'_α $a_{\rm iso}$ value with literature is likely due to having carried out a fitting involving both $a_{\rm iso}$ and $a_{\rm aniso}$ in contrast with previous work only based on $a_{\rm iso}$ [107]. For all samples in which E'_δ defects are observed, we find that the E'_γ effective hf splitting (distance between the top of the simulated absorption-like signals) is 421-424 G, that is, somewhat larger than the common 418 G value [102]. The increased splitting has been ascribed to enhanced local strain in the vicinity of the E'_γ defects [102]. Local strain in the oxide may be beneficial for E'_δ defect generation.

4.4.3 Al-related signals

During second harmonic saturation mode measurements over enhanced magnetic field range, we noticed the presence in some samples of a low intensity 6-line spectrum which was readily traced back as originating from the Al E' center [46, 47], the 6-line structure stemming from the interaction of the unpaired electron with an Al nucleus (I = 5/2; η = 99.9 %). The observed signal is demonstrated in Fig. 4.6, showing a RT Q-band second harmonic saturation spectrum observed on

a γ-irradiated (200 kGy) KI sample. Inferred defect densities are listed in Table 4.2. Since the signal eludes standard first harmonic detection (too weak), these have been determined from the second harmonic saturation spectra through simulation of the observed spectra (see below) and assuming similar saturation behavior of the Al E' and E'_γ centers: the intensity of the 6-lines spectrum simulation was compared to that of the 420 G E'_γ doublet detected in the same scan, where the correct E'_γ defect density (associated hf doublet is 4.67 % of the central line) is independently obtained from standard first harmonic spectra by comparison to a co-mounted marker. Optimized Al E' signal simulation was obtained using ESR parameters: $a_{\rm iso} = 416$ G, $a_{\rm aniso} = 16$ G, $g_{iso} = 2.0011$, $g_{aniso} = 0.0007$, a Gaussian distribution in $a_{\rm iso}$ of spread $\Delta a_{\rm iso} = 26$ G (standard deviation), and a Gaussian convolution function of width $\Delta {\rm B}_{\rm pp} = 12$ G. To emulate this distribution on $a_{\rm iso}$ we have calculated spectra for 20 $a_{\rm iso}$ values evenly spread over the whole Gaussian $a_{\rm iso}$ interval, and added the weighed spectra to obtain the simulation shown in Fig. 4.6. While reliable relatively, the inferred densities in absolute terms should be considered rather as indicative. As it is clear from Table 4.2, the Al E' signal is observed, *before annealing*, in γ-irradiated samples, but only in those that also show the E'_δ signal (the E'_δ-glasses); annealing at $\sim$326 °C eliminates the signal.

The Al E' center, first observed by Brower [46, 47] in natural vitreous silica exposed to ionizing irradiation, was attributed to an electron captured on an ^{27}Al atom in a Si-substitutional position bonded to three oxygen atoms in a-SiO_2 matrix. Pertinently, the center was found to need a charge compensator to remain paramagnetic (ESR-active) above 57 °C; it stays paramagnetic up to 277 °C if stabilized by alkali ions and up to 377 °C if hydrogen is involved, otherwise it turns to its neutral, diamagnetic Al$\equiv$O$_3$ ($AlO^0_{3/2}$) state. As analyzed in detail [46, 47], the hf coupling matrix is influenced by the compensating agent. On these grounds, we may conclude that in the current case the compensating agent [47] is likely Na^+, an assignment apparently in agreement with the observation that the signal disappears after annealing at 326 °C.

Upon annealing ($T_{\rm an} \geq 326$ °C) the Al E' signal disappears in all the E'_δ samples. As illustrated in Fig. 4.7 showing a first harmonic RT X-band spectrum taken on γ-irradiated (200 kGy) and subsequently annealed ($\sim$336 °C) KI silica, there is a prominent broad signal overlapping the E'-defect range. The superimposed simulation represents Lorentzian broadening functions of width $\Delta {\rm B}_{\rm pp1} = 6.0$ G, $\Delta {\rm B}_{\rm pp2} = 6.5$ G, and $\Delta {\rm B}_{\rm pp3} = 10.5$ G broad along the principal g_1, g_2, and g_3 axes respectively, the g values reported in the literature for the $[AlO_4]^0$ center in both crystalline [42, 43] and vitreous [44] SiO_2, that is, $g_1 = 2.060$, $g_2 = 2.00854$, $g_3 = 2.00195$, and [43] $a_{\rm iso}(^{27}{\rm Al}) = 8.4$ G. The satisfactory fitting convincingly assigns this signal (also reported in previous ESR work [271] on E'_δ) to an Al atom substituting for a four-coordinated Si with an unpaired electron on a 2p nonbridging oxygen orbital [43]. This signal, extending over $\sim$100-G wide range at X-band (cf. Fig. 4.7), comes as a background on top of the E' spectra; it poses no problem,

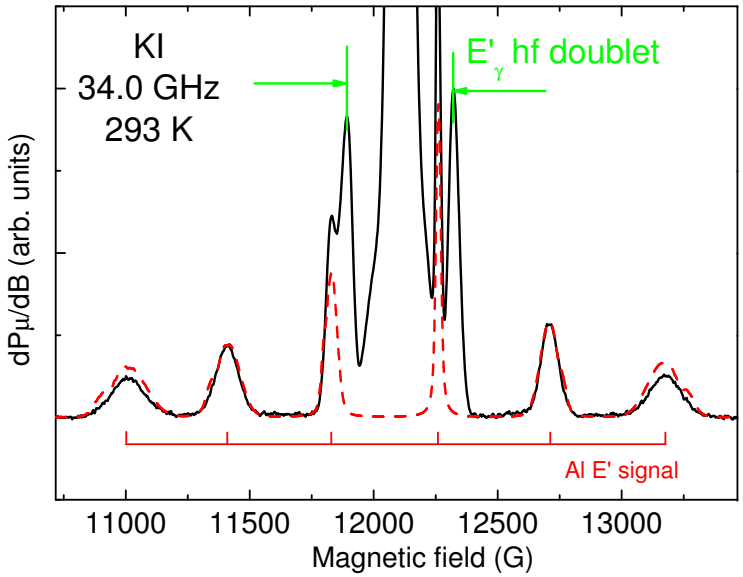

Figure 4.6: Room temperature Q-band second harmonic saturation spectrum (full curve) observed using $P_\mu = 1.6$ mW and $B_m = 1.5$ G on sample KI after 200 kGy γ-irradiation in the as-irradiated state, clearly showing the ^{27}Al hf six-line spectrum of the Al E' center. The superimposed dashed curve represents an optimized computer simulation giving $a_{iso} = 416$ G, $a_{aniso} = 16$ G, a Gaussian distribution in a_{iso} of $\Delta a_{iso} = 26$ G, $g_{iso} = 2.0011$ and $g_{aniso} = 0.0007$, and where a Gaussian convolution function of width $\Delta B_{pp} = 12$ G has been used. For more details, see text. The main 420-G E'_γ hf doublet is also marked. The off scale central part of the spectrum corresponds to the E' main signals.

i.e., not observably, for small-width small-B_m sweeps probing the central E' center lines (see e.g., Fig. 4.2). Yet for broader sweeps probing the E' hf structure using high(er) B_m, it does interfere. So, its presence has to be additionally taken into account for correct spectroscopic assessment of the E'_δ (100-G doublet) hf structure (cf. Fig. 4.7, where the high-field 100-G doublet signal is marked by arrow 2).

4.4.4 E'_δ spectrum and lineshape

As concluded previously, over all the a-silica samples studied and treatments applied here, the γ-irradiated (200 kGy), subsequently annealed (315-336 °C), KI sample turns out as the best one for the study of E'_δ signal and corresponding hf structure. Figure 4.8 shows the low power first harmonic ESR spectra of the E' main signals measured on γ-irradiated (200 kGy) and annealed (∼336 °C) KI

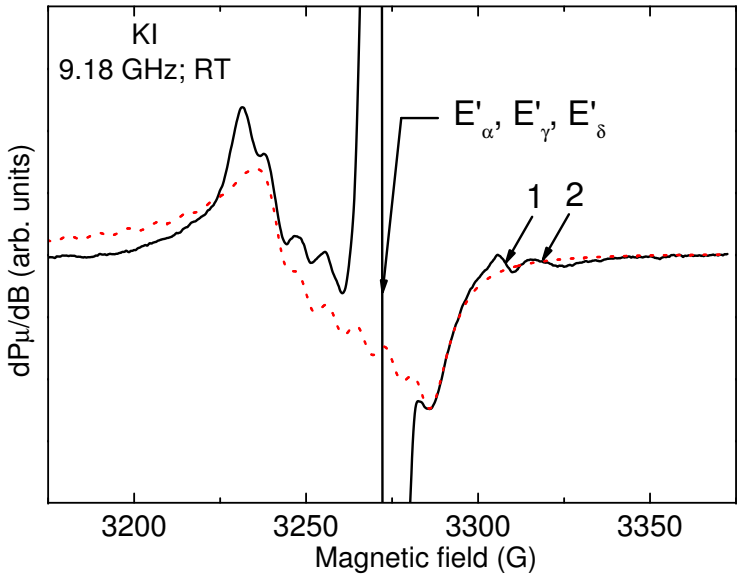

Figure 4.7: First harmonic X-band RT spectrum (full curve) observed using P_μ = 0.01 mW and B_m = 2.5 G on sample KI γ-irradiated to a dose of 200 kGy and subsequently annealed at 326 °C (8 min). In addition to the summed central main Zeeman E'_α, E'_δ, and E'_γ signals (off scale), the spectrum shows the $[AlO_4]^0$ signal. The high field components of the 74 G and 100 G hf doublets are indicated by the arrows (1) and (2), respectively (the low field components are masked in this high power scan by the overlapping $[AlO_4]^0$ signal). The dotted curve represents a powder pattern simulation obtained using $g_1 = 2.060$, $g_2 = 2.00854$, and $g_3 = 2.00195$, Lorentzian broadening functions of width $\Delta B_{pp1} = 6.0$ G, $\Delta B_{pp2} = 6.5$ G, and $\Delta B_{pp3} = 10.5$ G along the principal g axes, respectively, and $a_{iso}(^{27}Al) = 8.4$ G. The figure clearly illustrates that it is the Lorentzian tail of the $[AlO_4]^0$ signal which predominantly disturbs the indicated hf structure, not the Gaussian tail of the central E' signals.

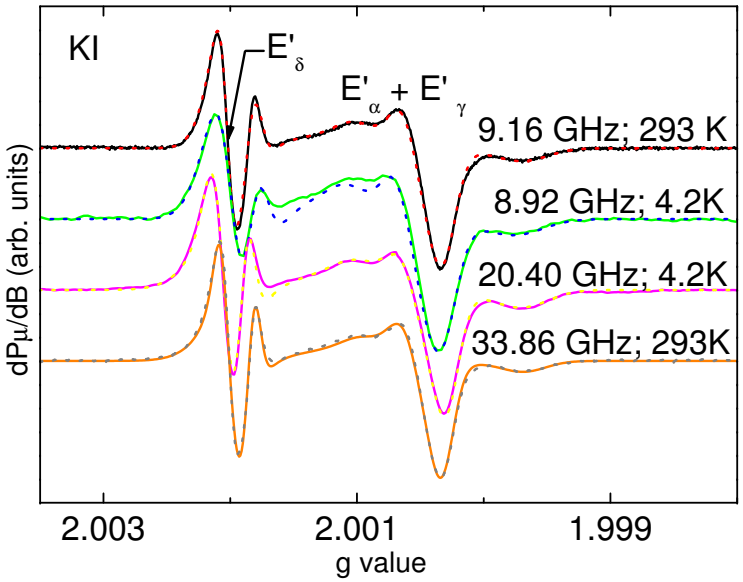

Figure 4.8: First harmonic low-power ($P_\mu < 1.6 \times 10^{-7}$ W and $B_m < 0.25$ G) spectra of the central E' signals measured on annealed γ-irradiated (200 kGy) and subsequently annealed (336-346 °C; air) KI samples at the microwave frequencies and temperatures indicated. Superimposed on each spectrum (dotted curve) is the weighed sum of separately optimized simulations of the constituent E'_α, E'_γ, and E'_δ signals using the g values listed in Table 4.1 but different broadenings for the different microwave frequencies.

silica in 4 spectrometers at 4.2 K or RT, as indicated. The Jeol X-band cavity, providing the largest sample space, enabled to fit in three samples bars ($\approx 2 \times 2 \times 10$ mm^3) at a time; For the other spectrometers, this was restricted to a single bar only. As the operational microwave power of the Q-band spectrometer cannot be sufficiently reduced, signal saturation prevents correct extraction of the absolute defect densities (e.g., Fig. 4.8 bottom spectrum): only the spectral shape parameters obtained from simulation are considered reliable. The dotted curves in Fig. 4.8 represent optimized spectra simulations obtained as weighed sum of the individual E'_δ, E'_α and E'_γ signal simulations using the parameters listed in Table 4.1 and Gaussian convoluting lineshapes. From X- and K-band simulations like these we obtained the individual E'_δ, E'_α and E'_γ defect densities.

For the splitting of the E'_δ hf doublet we measure 100 ± 1 G for all three microwave frequencies, independent of T in the interval 4.2 - 300 K. Figure 4.9 shows representative high P_μ second harmonic phase quadrature spectra observed at various microwave frequencies and temperatures on annealed (∼336 °C) γ-

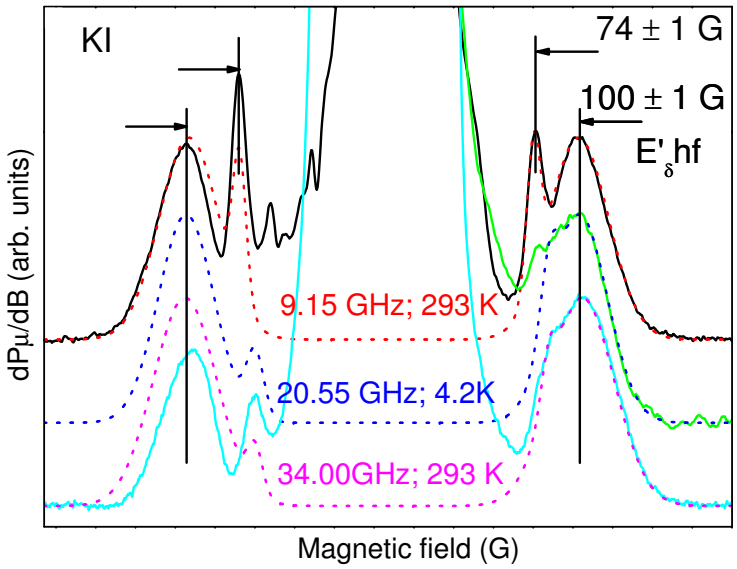

Figure 4.9: Second derivative phase quadrature saturation spectra ($P_\mu < 1.6$ mW, $\Delta B_{pp} < 1.5$ G) obtained on the same KI samples as dealt with in Fig. 8. The superimposed dotted curves each represents the weighted sum of the simulation of two isotropic doublets using Gaussian shapes, corresponding to the E'_{74} 74 G and E'_δ ^{29}Si 100 G-split hf doublets, as indicated. The extracted simulation parameters were used for disentangling of the corresponding direct detection (first harmonic) mode spectra shown in Fig. 10. In the K-band spectrum (middle curve) the left side is overwhelmed by the $[AlO_4]^0$ absorption signal (off scale at the low magnetic field side of the spectrum).

irradiation KI silica, focused on the E'_δ hf structure spectral region. In this detection mode the hf signals appear as closely resembling the direct absorption shapes, and because of the offered enhanced sensitivity, these spectra were taken to analyze, in a comparative manner, the E'_δ hf signal shape over various observational T's and microwave frequencies. From spectral simulations, optimized at the less perturbed high field signals (cf., dotted curves in Fig. 4.9), it is inferred that both the 74 G and 100 G doublets peaks shape in closely Gaussian of half-width at half height $\Delta B = 3.7 \pm 0.5$ G and 15 ± 0.5 G, respectively, independent of observational P_μ and T. The constant broadening likely results from strain-induced spread in (principal) hf matrix constants (a_{iso}, a_{aniso}). This assembled information is considered essential for the final step in analysis, that is, correct interpretation of the ultimate properly measured first harmonic E'_δ hf structure.

Since the E'_δ center is part of the same defect family as E'_γ (and perhaps E'_α) for

which we need anisotropic hf matrices to correctly simulate the corresponding doublets, we also tried to fit the 74 G and 100 G doublets using appropriate anisotropic hf matrices. Yet, due to the rather small hf splitting of both doublets, the added hf anisotropy is barely affecting the doublet shapes. Therefore, within the view of limiting the fewest number of variables for the same result, we simulated the doublets as being isotropic Gaussians, but still recall that an anisotropic lineshape may be fitted as well.

Unlike X- and Q-band observations, in the K-band low-T (4.2 K) saturation spectra we also observe the $[AlO_4]^0$ absorption signal, probably due to a favorable choice of parameter settings (see e.g., Fig. 4.9). That is why for the 20.55 GHz spectra we restricted the simulations to the high-field peaks (cf. Fig. 4.9).

Since the E' central signals and the 100 G doublet hf peaks show distinct differences in their widths, amplitudes, and saturation levels, we choose to adapt part of the measurement parameters, like B_m and P_μ, so as to individually optimize the signal-to-noise ratio for each type of signal studied, yet without distorting it. For this reason, measuring the two groups of signals in the same scan proves not optimal, so we measured them separately but carefully compensated for the different parameter settings used when calculating the corresponding intensities and densities.

As a main focal point, Fig. 4.10 shows zoomed in low P_μ and B_m first harmonic spectra observed at various P_μ's and T's of the high field component of the E'_δ hf doublet, with on top, the analogous 74-G doublet component (marked (2) and (1), respectively). The signals have been corrected for an underlying Lorentzian background pertaining to $[AlO_4]^0$ centers. Indeed, as evident from Fig. 4.7, the high field E'_δ hf peak is mainly perturbed by this $[AlO_4]^0$ signal shape and not by the tail of the central E' signals. The dotted curves in Fig. 4.10 represent optimized simulations for which the previously inferred information (lineshape, broadening) from the corresponding saturation spectra has been consistently used. Finally, from this detailed hf structure analysis combined with the (previously) inferred intensities of the central E'_δ ESR signal, we obtain over the analysis of various spectra for R_{hf} the values: (19.7 ± 2.5) % at 4.2 K and (20.3 ± 2.0) % at RT from X-band measurements, and (20.9 ± 1.3) % for the K-band 4.2 K data, where the error bars represent standard deviation. While reassuringly coinciding within experimental error, the data directly and importantly show R_{hf} to be T-*independent* over the range 4.2-295 K. It indicates there would be no dynamic averaging effects of the unpaired electron involved. Taking the average over all the data points obtained from measurements at different frequencies and temperatures we obtain, as a global average, $R_{hf,av}$ = (20.3 ± 1.9 %).

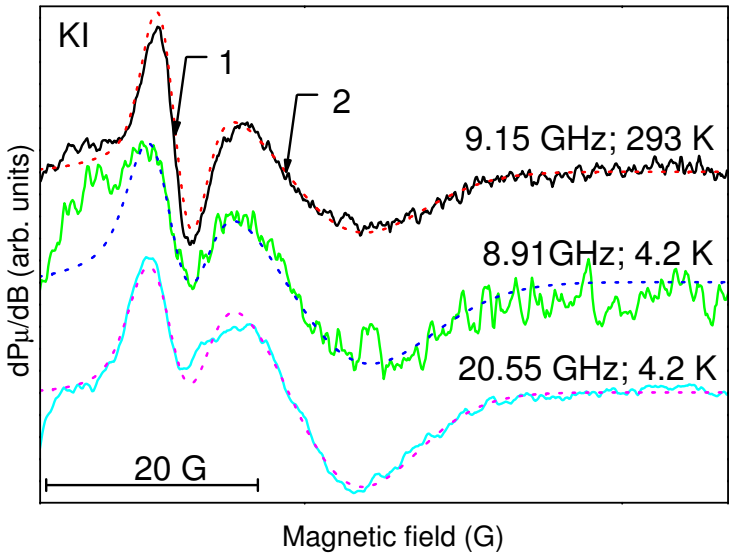

Figure 4.10: First harmonic low power mode ESR spectra measured at various microwave frequencies and two temperatures on the sample the ^{60}Co γ-irradiated KI samples addressed in Figs. 4.8 and 4.9. The spectral window is focused on the high-field signals of the 74-G (1) and E'_δ 100-G hf (2) doublets, as indicated. The observed curves have been corrected for an underlying Lorentzian background shape pertaining to the overlapping $[AlO_4]^0$ signal. The dotted curves represent optimized simulations making use of the previously derived spectral information from measurements such as shown in Figs. 4.7 and 4.9. In combination with the analysis of the central E'_δ signal, the R_{hf} ratio inference was based on these simulations, leading to an average value $R_{hf,av} = 20.3 \pm 1.9$ %.

4.5 Analysis and discussion

4.5.1 E'_δ occurrence and stability

Over all the vitreous silica glasses studied, and the three types of irradiations applied, we found that the E'_δ signal could only be produced in three kinds of silica: PH370, Infrasil 301, and KI (cf. Table 4.2), and this only, yet always also, by two types of damaging: VUV (10.0 eV) and ^{60}Co γ-rays. But with the E'_δ signal barely detectable in the as-irradiated state, the later method requires an extra post-irradiation short anneal ($\sim$326 °C; 8 min) to fully turn on the E'_δ defect signal ($\sim 10^3$ fold increase). No such anneal is required after VUV irradiation. No E'_δ could be produced by UV photons ($h\nu \leq 6.5$ eV) in agreement with previous

work [301, 305]. Only E'_α and E'_γ signals were observed.

We should underline the fact that the VUV and ^{60}Co γ-irradiations came as a match for each other in terms of effective E'_δ production. Given the distinct disparity regarding energetic quantum (10 eV vs. ∼1.17 - 1.33 MeV photons), this clearly bears out the importance in glass nature for E'_δ occurrence in that it must meet some precursor requirements such as, likely for the current case, O-deficiency and possibly, the presence of charge compensating units.

Furthermore, comparison of UV with VUV and γ-irradiation results suggest that E'_δ signal activation starts from preexisting sites: indeed, the observation that the E'_δ signal appears after irradiation with $h\nu > E_{g,SiO_2}$ (the SiO_2 band gap; over band gap excitation) indicates ESR defect activation as a result of ionization rather than displacement process. Also, as to the applied UV doses, the two-photon process [306] appears insufficient for the E'_δ activation to a detectable level, unlike E'_γ and E'_α. We further notice that, compared to γ damaging, VUV irradiation appears exhaustively efficient on this matter as an additional thermal step only slightly increases the E'_δ signal. In one view, if change compensators are involved [45], it might indicate that an intense fluence of VUV photons over a limited volume may enhance compensator migration at RT.

As to γ-irradiation, the maximum volumetric E'_δ density of $\approx 1.1 \times 10^{16}$ cm^{-3} is obtained for KI silica subjected to 200 kGy ^{60}Co γ-rays and subsequent thermal treatment at 336 °C. For comparison, VUV irradiation for 20 h of the same KI silica results in an areal E'_δ density $\approx 1.4 \times 10^{13}$ cm^{-2} (determined from the main central ESR line) located in the thin surface layer it penetrates. If assuming a mean VUV penetration depth [297, 298] of ∼10 nm, this would translate to a volume density of $\sim 1.4 \times 10^{19}$ cm^{-3} –much larger than the above volumic density obtained by ^{60}Co γ-irradiation. However, this value is likely overestimated: if assuming, as likely, that the over bandgap e-h pair production is essential in ESR-activating E'_δ defects, the much deeper diffusion of e-h pairs (orders of magnitude) [307] will result in a more likely local E'_δ density in the range (1-10) $\times 10^{16}$ cm^{-3}, compatible with the ^{60}Co γ-irradiation result. Yet, it cannot be excluded that SiO_2 layers closer to surface are more prone to E'_δ production as, e.g., reported before for BOX [118]. In the current work, the E'_δ-glasses may be in that case (cf. Table 4.2).

Left in room ambient after production by irradiation, the E'_δ signal was found to bleach in time, though on a larger time scale than reported before [275]. For VUV-activated E'_δ centers, the decay time is $\gtrsim$1 year, while $\gtrsim \frac{1}{2}$ year for γ-ray treatment. This contrasts with the behavior reported for BOX samples, where almost total bleaching of the E'_δ signal is observed ∼days after activation with positive biased corona/VUV activation [308] or conventional electrode positive bias/VUV photoinjection [275], and weeks in the case of positive dc glow discharge irradiation [275]. Interestingly, regarding this E'_δ signal decay, the former ESR work has suggested direct evidence for increase of the E'_γ signal at the expense

of E'_δ centers due to direct defect-defect hole transfer [308]. The fact that the E'_δ centers density saturates with VUV irradiation time indicates a generation from precursor sites, which can be removed by reoxidation [274].

4.5.2 E'_δ: hf structure intensity

As firmly evidenced in previous ESR works [41, 271], the observed 100-G doublet constitutes the principal hf structure associated with the E'_δ center, showing close correlation, both qualitatively and quantitatively, with the central E'_δ Zeeman signal. Various ESR studies on different types of SiO_2 have led to the net conclusion E'_δ to be an E'-type intrinsic defect, i.e., no direct involvement of an impurity in the defect kernel. So, based on the non-zero nuclear spin (I $\neq$ 0) isotropic composition of ordinary SiO_2, the hf structure is logically ascribed to interaction of the unpaired electron with the ^{29}Si (I = 1/2; η = 4.67 %) isotopes. On grounds of ESR feasibility considerations, interaction with ^{17}O (I = 5/2; η = 0.034 %) is to be excluded as alternative.

As outlined, a decisive key factor in steering reliable atomic defects modeling is the number n of (nearly) equivalent Si sites involved in the hf interaction, that is, over which the unpaired electron wave function is delocalized. This must be obtained from correct determination of the ratio $R_{hf}(\eta, n)$ which for small η values is given to good approximation by the expression in Eq. 1.25, where the simultaneous occurrence of two or more I $\neq$ 0 isotopes in a shell has been neglected (for Si, maximum error <0.2 % for n < 6). The expected values for Si shells (n = 1-6) are listed in Table 1.1.

Comparison to Table 1.1 of the experimental value $R_{hf,av}$ = (20.3 $\pm$ 1.9)%, measured by the orthodox first harmonic non saturation mode, clearly shows that the n = 2 case (Si_2 dimer model) invariably promoted by theory is to be ruled out definitively, in agreement with previous result [271]. In passing to remunerate first assignment [41], there should thus be an overturn in the attitude in labeling, that is, discontinue the usage of the label E'_δ, first given to the observed ESR spectrum, for the Si_2 (charged Si dimer) defect calculated by theory [93, 121, 286, 269]. In fact, the comparison shows the experimental $R_{hf,av}$ value falls between the n = 4 and n = 5, closest to the former, so concluding the 4-Si case would seem straightforward. Yet, some caution should be urged regarding this direct inference. In line with scientific rigor, we here should refer to the experimental determination of R_{hf} pertaining to other point defects involving unpaired sp^3 Si hybrids in Si/SiO_2 entities. In this context, previous works have reported on measured R_{hf} values generally somewhat smaller than expected, where the loss in hf intensity was attributed to *broadened portions* of the ^{29}Si spectrum lost in the noise [27] as a result of varying local strain over the defect sites [309]. The further a hf component is split out, the more strongly it becomes broadened as a result of the

weak site-dependent modifications in the distribution of the unpaired electron's wave function over the interacting nuclei due to the local weak alterations in the defect atomic structure when embedded in an amorphous, like a-SiO_2, structure (the glass effect) [303]. On this account, we cannot exclude n = 5 as a valid option.

Thus, on grounds of simply counting numbers of Si atoms figuring in atomic models, the obtained experimental n = 4-5 result would seem to plainly select out either Si_4 or Si_5 as suitable model. But, looking deeper, based on the current strict result neither of these (4- and 5-Si) can be retained on theoretical grounds, basically because, as jointly calculated [120, 121, 269, 285], the spin density of the unpaired Si electron asymmetrises for whatever cluster model, in the sense it gets localized to a large extent in an elongated bond between two adjacent Si atoms (Si_4), or primarily on a single Si atom (Si_5), so these models would, like the Si_2 one, correspond to the n = 2 situation as well. This leaves us with an uncomfortable hiat: there appears so far no acceptable atomic model for E'_δ at hand. Hinging on theory, it means our current perception of the E'_δ center needs revolutionizing. This conflicting situation will be elaborated upon below.

4.5.3 E'_δ correlation with Al-related defects

A noteworthy observation is that, as to the ^{60}Co γ-irradiation damaging, we could observe (generate) an E'_δ signal (albeit after annealing) only in those vitreous silica types also showing the Al E' center (perhaps compensated by Na^+ ion in its vicinity) in the as-irradiated state; as is seen from Table 4.2, all three E'_δ-silica exhibit an Al E' density in the range (3 - 5) $\pm$ 10^{15} cm^{-3}. As also evident from Table 4.2, no Al E' signal could be detected after VUV irradiation, which, however, does turn on the E'_δ ESR signal. This is ascribed to the limited penetration depth of the VUV irradiation in SiO_2, failing to establish an ESR-detectable sufficient overall number of Al E' centers within one ESR sample in the cavity. We further notice that there seems no correlation between the occurrence of E'_γ and Al E'.

So, the revealed systematic co-presence of Al impurities, here exposed in the form of Al E' centers, might suggest some determinative influence on E'_δ generation. Obviously, within the current admitted understanding of both types of defects, the process cannot concern direct charge transfer between the centers, i.e., electron transfer from the neutral E'_δ precursor to the negatively charged Al E' center. Yet, dealing with charged defects, as admitted, the negatively charged Al E' center (without compensator) could operate as a charge compensator for the positively charged E'_δ. But apparently not so. Rather than both types of defects increasing in tandem, their *non-simultaneous* observability indicates anticorrelation: The E'_δ centers seem to emerge at the expense of Al E' defects. One possibility for the disappearance of Al E' centers upon annealing is through exchange, i.e., electron

transfer, from the ESR-active Al E' to a $[AlO_4]^+$ precursor, the latter now becoming paramagnetic.

In this context, we may also refer to the various other ESR works reporting the co-observation of Al-related defects in studies of E'-type centers in quartz [43, 45, 271, 46, 47, 291, 310]. For one, Buscarino et al. in their work [291] on the E'_δ in v-SiO_2 suggested a correlation between the E'_δ and E'_γ activation and the presence of $[AlO_4]^0$ centers, in the sense of hole transfer during thermal treatment (T $\geq$ 500 °C) from $[AlO_4]^0$ to diamagnetic E' precursors. Such limited correlation was previously concluded [45] to exist between the production of the E'_1 centers and $[AlO_4]^0$ concentration, through continuously adding that the E'_1 production may be more complex than simple hole transfer.

In these schemes, discussing the correlated presence of Al-related defects and E' center activation, the key influence of charge compensators has emerged [45, 46, 47]. In an archival work, the aspect of charge transfer between negatively charged [AlO4]- and neutral AlO_3 entities upon irradiation, and correlated movement of charge compensators has been demonstrated by Brower [46, 47]. In this perspective, the essential point in co-observation of Al E' centers may be bearing out the importance of charge compensators for E'_δ activation.

Finally, in keeping with scientific objectivity, one may take a totally contrasting view, deferring any correlation: the ESR observation of Al E' centers might just constitute one more evidence for the E'_δ-silica being O-deficient [47], an admitted requirement for a silica glass to enable E'_δ production. So, while the presence of Al impurities seems not merely coincidental to E'_δ activation, understanding its precise correlative nature must await further detailed experimenting.

4.5.4 Lack of Si dimer (Si_2) signal

With the E'_δ ESR signal decisively excluded as pertaining to the positively charged Si dimer (Si_2) defect, we (still) face the astonishing situation that the latter center has so far not been experimentally observed, at least not recognized as such -this unlike broad and concurring theoretical outcome, favoring the occurrence of this center as a *natural* defect in both crystalline [93, 283, 284, 286, 287] and amorphous [109, 269, 289] SiO_2. Upon hole trapping at the neutral O-vacancy precursor site (O_3 ≡Si-Si≡O_3) in c-SiO_2, the (calculated) probability for either ending up in E'_δ or E'_1 formation is calculated to be close, although the actual value may be somewhat uncertain [93, 283, 311]. As to a-SiO_2, it has been calculated that ∼80 % of the single O vacancies would remain in the dimer configuration upon hole trapping [289]. What is the origin of this apparent paradox? There may be several suggestions:

In a first view, it might simply result from the idea of unfavorable ESR signal

properties, such as excessive line broadening, preventing Si_2 observation on pure experimental grounds. Yet, based on general ESR experimental experience with, and insight on, E'-type defects in SiO_2, this suggestion can hardly be retained.

As another spectroscopic feature a second more far-fetched possibility may start from the notion that the theoretically predicted ESR properties for the positively charged Si dimer (Si_2), i.e., regarding g matrix and hf doublet splitting (yet not relative hf structure intensity) comply with the experimental E'_δ properties. So, should the Si_2 defect persistently coexist only as a limited fraction (say $\lesssim 20$ %) of E'_δ, it will remain spectroscopically unresolved, including, within current experimental error, what concerns the observed R_{hf} value -a case of inextricable signal overlap. In this context, we notice that previous work [275] has suggested the existence of two E'_δ variants. Obviously, such overlap (n = 2 for Si_2) would result in effective lowering of the relative hf structure intensity, so that the true R_{hf} value of E'_δ will be larger than actually measured. But then, of course, the question arises:Why E'_δ-silent silica is (only) showing E'_1 (E'_γ) and E'_α signals?

This leads us to a next possibility, based on calculated defect formation energies. A theoretical work on c-SiO_2 (α-quartz) concludes [283] that the formation of a positively charged Si dimer is, compared to that of E'_1, energetically unfavorable. So, E'_1 will be the dominant E'-type defect in (damaged) c-SiO_2. But apparently, while supported by one work [93], it is contradicted by other theoretical works [109, 289, 311] on E'-type centers in a-SiO_2. Yet, in this respect, as cautioned by Mukhopadhyay et al. [109], we note that the accurate prediction of relative concentrations of possibly coexisting E'-type centers remains a key issue. It may still appear undecided.

But perhaps, in a contrary view, the Si_2 has already been observed: indeed, as it stands today, the disproval of Si_2 as E'_δ model has only been correctly established in commercial ^{60}Co γ-irradiated fused quartzes and, perhaps to a different extent [119] in CVD-made silica subjected to x-rays. Should, e.g., dissimilar defect generation schemes (e.g., different types of samples, irradiation etc.) result in generation of the supposedly two types of centers in different proportions, then unless ascertained by correct analysis of the ^{29}Si hf structure, one cannot be sure about the exact origin of the observed spectrum in terms of originating defect. It may all appear rather far-fetched, but if true the anticipated highly isospectral appearances of E'_δ and Si_2, utmost care is required, the more given the fact that the experimental situation is invariably aggravated by overlapping intense signals of other co-existing defects.

4.6 Conclusions and final remarks

A multifrequency ESR study has been performed on E'-type point defects in amorphous silica, with main focus on the E'_δ center, for which a trustworthy atomic

model remains elusive. This has been carried out at both cryogenic and room temperatures using two types of ESR detection modes on six types of commercial vitreous silicas, subjected to three types of irradiations (UV, VUV, and ^{60}Co γ photons), with the intend to provide a consolidating expanded and statistically relevant set of data, over a broad range of ESR variables, on the ^{29}Si E'_δ hf structure -all aimed to further decisive atomic modeling. Much effort has been devoted to correct determination, by means of orthodox non-saturation cw first harmonic mode ESR spectroscopy, of the relative intensity $R_{hf}(\eta, n)$ of the associated ^{29}Si hf structure to the central Zeeman signal. The investigation has lead to several results.

The E'_δ signal could be generated only in three types of a-silica, and only, yet always, by two types of irradiation, i.e., VUV and ^{60}Co γ rays. This suggests that E'_δ generation predominantly starts from preexisting sites where the signal 'switching on' after irradiation with photons $h\nu > E_{g,SiO_2}$ (e-h pair generation) indicates as key scenario activation as a result of ionization rather than atom displacement processes. We further notice that, unlike VUV, the ^{60}Co γ-irradiation damaging requires an additional mild thermal step ($T_{an} \simeq$ 320-350 °C) to fully expose the E'_δ signal.

Apart from Si E'-type centers, Al-related defects were observed as well. Besides the 'common' $[AlO_4]^0$ center, using second harmonic saturation spectroscopy, the Al E'-defect is revealed in as γ-irradiated silica, but pertinently, only in those three showing the E'_δ center as well –bearing out these glasses to share (a) structural/compositional aspect(s) fit for common E'_δ and Al E' generation. Upon additional annealing, the E'_δ signal is seen to ramp up at the cost of the vanishing Al E'. While direct inter-defect charge exchange is likely to be excluded, yet, the correlated occurrence of both types of centers might suggest some indirect effect of Al-related centers in the E'_δ appearance. For one, it could signify some indirect role of charge compensators in activating and/or stabilizing E'_δ centers. The observation may inspire future work. However, in a contrasting view, the co-appearance of E'_δ and Al E' centers in the same glasses might just be seen as putting forward one more evidence one is dealing with O-deficient a-silica, as admittedly required for the occurrence of E'_δ centers.

As a main result, the various $R_{hf,av}$ values measured on the γ-irradiation KI-type a-silica are found reassuringly coinciding (within experimental error) over all three observational frequencies and temperatures applied. The obtained average value ($R_{hf} \approx 20.3$ %) points to ^{29}Si hf interaction of the unpaired E'_δ electron with n = 4(5) equivalent Si sites in a shell, herewith, in line with a previous result, decisively refuting the repeatedly proposed positively charged Si-dimer (Si_2) model for the E'_δ center. The bare as-inferred value would plainly point to the n = 4 case, as initially proposed, yet, it is felt the n = 5 case cannot be excluded, and in fact is given full consideration, in view of previous experience with measurement of ^{29}Si hf structure of the Si dangling bond defects.

In fact, according to current theoretical insight, none of the thus far advanced atomic structures can be retained as valuable candidate basically because the Si_4 and Si_5 models, like Si_2, essentially correspond to n = 2 and n = 1 cases a result of the localization of the unpaired spin density to large extend, either in an elongated bond between a pair of Si atoms (Si_4), or primarily on a single Si atom (Si_5): the unpaired spin does not delocalize over the entire cluster, whose reduction in symmetry of the electron wave function was attributed to the dynamic Jahn-Teller effect. Although E'_δ is widely accepted as a member of the specific O-vacancy related E'-defect family, clearly this leaves a paradoxical situation.

As a corollary, attention is called for consistency in labeling, that is, the use of the E'_δ label, a defect spectrum observed by ESR, for the Si_2 model propagated by theory, should be discontinued: Si_2 is not E'_δ.

The E'_δ ESR signal parameters (such as g matrix, linewidth) as well as the hf structure are shown to be T-independent in the range T = 4.2-300 K, indicating that, should there be involved any dynamical averaging process over electronically equivalent defect configurations, it must so already be established at T < 4.2 K, putting strict limits on such possibility. As the hf data reveal, neither does there occur any T-dependent redistribution of the unpaired electron orbital over adjacent atomic (Si) sites. It all points to an electronically rigid structure. So, if E'_δ is admitted to be a delocalized electron center, it will concern a chemically fixed delocalized bonding (arrangement).

With the revealed incompatibility of the Si_2 model with the E'_δ center, it appears that we have slided into the situation that over the numerous ESR studies carried out on SiO_2, the existence of the former has, so far, not been experimentally demonstrated, which, depending on E'_s view, may come as a surprise. It leaves an uncomfortable hiatus in insight, for which several possibilities may be offered. As a tentative, perhaps naive one, the Si_2 defect may have escaped ESR evidencing as a result of its projected, closely isospectral ESR appearance as the E'_δ signal, so it may remain unresolved should it, for some unknown reason, only occur as a limited fraction of E'_δ. More possibilities have been discussed in the text.

Finally, in assessing the implications of the current work, more research will be required regarding modeling of E'_δ in vitreous SiO_2 and, correlated herewith, establishing, perhaps also experimentally, the fate of the anticipated Si_2 centers. As alluded above, this research may be hampered by the very exceptional encounter of dealing with two variants of the defects showing highly isospectral ESR characteristics (apart, of course, of the respective R_{hf} values). It may inspire theoreticians to take a next step is the demanding task of modeling of defects in a-SiO_2 that is taking into consideration additional complexing factors, such as the occurrence of charge compensators, dynamical averaging phenomena, and influence of H.

Conclusions and future work

This work is concerned with an elaborate ESR study of, mostly native, point defects in different kinds of structures consisting of nanocrystalline-Si particles embedded in an a-SiO_2 matrix. This includes superstructures manufactured through thermal treatment of the as deposited SiO/SiO_2 multilayers on Si, and Si^+ implanted thermal SiO_2 assisted by in situ UST. Additionally, the efforts given to trace the true atomic nature of the illusive E'_δ defect in a-SiO_2 can be seen along these lines. We monitored and characterized the different varieties of point defects in those structures both in the as-produced state as well as after different treatments such as annealing in different ambient gases (N_2, Ar, room ambient, H_2) as well as pre- or post-anneal irradiations (UV, VUV, and ^{60}Co γ-rays) to alter the paramagnetic point defect densities, that is, lowering them in the case of nc-Si's but increasing them in the case of E'_δ defect investigation.

As to nc-Si/SiO_2 superstructures, an important result attained by combining extensive ESR and PL spectroscopies using passivation and depassivation of paramagnetic defects is to demonstrate the possibility of switching from defect related PL to quantum confinement originating PL and viceversa in the same sample.

Another major result indicates that, in fact, $P_{b(0)}$ point defects are *quenching* the PL emission of nc-Si in a-SiO_2.

Relying on the known properties of P_b-type defects in standard microscopic Si/SiO_2, the data in this thesis would comply with Si nanocrystallites, in average, predominantly bordered by (111) and (100) facets, perhaps with morphology, schematically, of (100) truncated (111) octahedrons. Based on independent nc particle counting, there appears to be one strain releasing P_b-type center for each Si nc.

On the basis of the observed intrinsic point defects, the SiO_2/c-Si nanoparticles interface subjected to high-T annealing appears to approach that of standard thermal Si/SiO_2 structures. It indicates that the superb microscopic Si/SiO_2 properties are *retained down to the nanoscale*. The structure proves to be stable

from the viewpoint of the interface defects, without any inadvertent significant H passivation of dangling bonds having occurred during sample fabrication.

The ambient used to anneal Si-rich SiO_2 is influencing the atomic configuration of the samples and to some extent the PL properties. N_2 is diffusing towards the nc-Si/SiO_2 interface *bonding into the structure*. This results in local strain release (25 % less P_b-type defects than in the Ar annealed samples) but also in a PL signal blueshift that can be interpreted as resulting from the influence of different polarities of the nc terminating groups such as O and N.

A connection between nc-Si size and strain release through P_b-type defects at their interface with the surrounding matrix is a research line that can be followed to assess the *optimal size* of the Si nanocrystals for the different intended applications. This must be associated with an independent particle count for the different nc-Si sizes.

A second main part of this work has addressed the influence of *in situ* applied ultrasound during Si^+ implantation in a-SiO_2 thermally grown on Si. The in situ UST during ion implantation has been reported previously to ensue a beneficial effect on various properties, such as improvement of performance and reliability of electronic devices, and stimulate cluster precipitation and growth. In the current work, the ESR technique has first been applied to asses the effects of UST on true atomic level, viz., probing of point defects and their behavior over various treatments. This indeed reveals an impressive *healing* effect of in situ UST.

Our results indicate that in situ UST during ion implantation has a *gettering* effect on the defects made by the implanted ions, resulting in defect density decrease, viz., Frenkel pair elimination, and the remaining paramagnetic defects are distributed in a thinner layer than in the case of non-UST. The beneficial effects are retained also after high-T anneal, resulting in the *removal of virtually all ESR active centers*. Thus UST turns out to improve system relaxation and internal strain, producing a *reduced defect system* with an interface quality approaching the one of the thermally grown a-SiO_2 on Si that is taken as reference.

In a final part, the atomic hf structure of the E'_δ point defect in a-SiO_2, focusing on R_{hf}, was investigated extensively. The obtained value for the latter at different microwave frequencies and measurement temperatures excludes the Si_2 atomic model advocated by theory, leaving the Si_4 and Si_5 models standing. Previous experience with R_{hf} determination of other Si related defects in Si/SiO_2 entities make us incline towards the Si_5 as the atomic model for this center.

During the research on the ^{29}Si hf structure of E'_δ center, the exclusive co-presence, always, has been revealed of the Al E' center in glasses in which E'_δ centers could be activated through irradiation –"the E'_δ-glasses"; pertinently, the Al E' could not be traced in the E'_δ-silent glasses. Perhaps, as one consequence, the co-occurrence of Al impurities may account for the high stability of the observed E'_δ defect in

this work, that is, ∼1-2 years as compared to one week reported in other cases. Although a direct correlation between the Al E' centers and the E'_δ centers is not obvious, the presence of the two centers only in the E'_δ-glasses indicates the need of a correlative research following this line.

Lately, the solar cell industry is driving towards the nanotechnology approach in an attempt to improve efficiency. Given the knowledge accumulated in the research of nc-Si embedded in SiO_2, ESR can prove to be a key technique in understanding fundamental aspects regarding solar cells, and thus, potentially contributing to find methods to improve the solar energy conversion efficiency.

Bibliography

[1] D. Bishop. *Bell Labs Technol. J.*, 10:23, 2005.

[2] L. Pavesi. *J. Phys.: Condens. Matter*, 15:R1169, 2003.

[3] G. G. Ross, D. Barba, and F. Martin. *Int. J. Nanotechnol.*, 5(9):984, 2008.

[4] M. Porti, M. Avidano, M. Nafria, X. Aymerich, J. Carreras, O. Jambois, and B. Garrido. *J. Appl. Phys.*, 101(6):064509, 2007.

[5] K. I. Han, Y. M. Park, S. Kim, S. H. Choi, K. J. Kim, I. H. Park, and B. G. Park. *IEEE Trans. Electron Devices*, 54(2):359, 2007.

[6] T. Z. Lu, J. Shen, B. Mereu, M. Alexe, R. Scholz, V. Talalaev, and M. Zacharias. *Appl. Phys. A*, 80(8):1631, 2005.

[7] S. Pizzini, M. Acciarri, S. Binetti, D. Cavalcoli, A. Cavallini, D. Chrastina, L. Colombo, E. Grilli, G. Isella, M. Lancin, A. Le Donne, A. Mattoni, K. Peter, B. Pichaud, E. Poliani, M. Rossi, S. Sanguinetti, M. Texier, and H. von Kanel. *Mater. Sci. Eng. B*, 134(2-3):118, 2006.

[8] E. Zavoiskii. *J. Phys. U. S. S. R.*, 9:211, 1945.

[9] D. L. Griscom. In G. Pacchioni, L. Skuja, and D. L. Griscom, editors, *Defects in SiO_2 and Related Dielectrics: Science and Technology*, page 117. Kluwer Academic, Dordrecht, 2000.

[10] Charles P. Poole. *Electron Spin Resonance. A Comprehensive Treatise on Experimental Techniques.* Dover Publications, New York, second edition, 1996.

[11] John E. Wertz and James R. Bolton. *Electron Spin Resonance. Elementary Theory and Practical Applications.* New York, 2nd edition, 1986.

[12] A. Abragam and Bleany B. *Electron Paramagnetic Resonance of Transition Ions.* Clarendon Press, Oxford, 1970.

[13] J.-M. Spaeth, Niklasm J. R., and R. H. Bartram. *Structural Analysis of Point Defects in Solids: An Introduction to Multiple Magnetic Resonance Spectroscopy*. Springer-Verlag, Heidelberg, 1992.

[14] D. L. Griscom. *Phys. Rev. B*, 20(5):1823, 1979.

[15] T. E. Tsai and D. L. Griscom. *J. Non-Cryst. Solids*, 91(2):170, 1987.

[16] G Feher. *Bell Syst. Technol. J*, 36(2):448, 1957.

[17] A. Stesmans. *Phys. Rev. B*, 45(16):9501, 1992.

[18] A. Stesmans. *J. Magn. Reson.*, 76(1):14, 1988.

[19] A. Stesmans and Y. Wu. *J. Phys. D*, 21(7):1205, 1988.

[20] N. D. Yordanov and A. Christova. *Appl. Magn. Reson.*, 6(1):341, 1994.

[21] J. Krzystek, A. Sienkiewicz, L. Pardi, and L. C. Brunel. *J. Magn. Reson.*, 125(1):207, 1997.

[22] I. B. Goldberg. *Spec. Prog. Rep.: Electron Spin Reson.*, 6:1, 1981.

[23] M. H. Brodsky and R. S. Title. *Phys. Rev. Lett.*, 23:581, 1969.

[24] M. Stutzmann and D. K. Biegelsen. *Phys. Rev. B*, 40(14):9834, 1989.

[25] P. J. Caplan, E. H. Poindexter, B. E. Deal, and R. R. Razouk. *J. Appl. Phys.*, 50:5847, 1979.

[26] E. H. Poindexter, P. J. Caplan, B. E. Deal, and R. R. Razouk. *J. Appl. Phys.*, 52(2):879, 1981.

[27] K. L. Brower. *Appl. Phys. Lett.*, 43:1111, 1983.

[28] A. Stesmans and V. V. Afanas'ev. *J. Appl. Phys.*, 83(5):2449, 1998.

[29] H. J. von Bardeleben, C. Ortega, A. Grosman, V. Morazzani, J. Siejka, and D. Stievenard. *J. Lumin.*, 57(1):301, 1993.

[30] A. Stesmans, B. Nouwen, and V. V. Afanas'ev. *Phys. Rev. B*, 58(23):15801, 1998.

[31] A. Stesmans and V. V. Afanas'ev. *Phys. Rev. B*, 57(16):10030, 1998.

[32] E. H. Poindexter and P. J. Caplan. In M Schultz and G. Pensl, editors, *Insulating Films on Semiconductors*, page 150. Springer, Berlin, 1981.

[33] A. Stesmans and V. V. Afanas'ev. *Appl. Phys. Lett.*, 69(14):2056, 1996.

[34] S. P. Karna, H. A. Kurtz, W. M. Shedd, R. D. Pugh, and B. K. Singaraju. *IEEE Trans. Nucl. Sci.*, 46:1544, 1999.

[35] A. Stesmans, B. Nouwen, and V. V. Afanas'ev. *Phys. Rev. B*, 66(4):045307, 2002.

[36] M. Mizuguchi, H. Hosono, and H. Kawazoe. *Mater. Sci. Eng. B*, 54:38, 1998.

[37] A. Stirling and A. Pasquarello. *Phys. Rev. B*, 66(24):245201, 2002.

[38] D. L. Griscom. *Phys. Rev. B*, 22(9):4192, 1980.

[39] D. L. Griscom. In D. L. Uhlmann and N. J. Kreidl, editors, *Glass Sci. Technol.*, volume 4B, page 151. Academic Press, New York, 1990.

[40] D. L. Griscom, E. J. Friebele, and G. H. Sigel. *Solid State Commun.*, 15(3):479, 1974.

[41] D. L. Griscom and E. J. Friebele. *Phys. Rev. B*, 34(11):7524, 1986.

[42] M. C. M. O' Brien. *Proc. R. Soc. London Ser. A*, 231(1186):404, 1955.

[43] R. H. D. Nuttall and J. A. Weil. *Can. J. Phys.*, 59(12):1886, 1981.

[44] R. Schnadt and A. Rauber. *Solid State Commun.*, 9(2):159, 1971.

[45] M. G. Jani, R. B. Bossoli, and L. E. Halliburton. *Phys. Rev. B*, 27:2285, 1983.

[46] K. L. Brower. *Phys. Rev. Lett.*, 41:879, 1978.

[47] K. L. Brower. *Phys. Rev. B*, 20:1799, 1979.

[48] DT Krick, PM Lenahan, and Kanicki. *Phys. Rev. B*, 38(12):8226, 1988.

[49] W. L. Warren, P. M. Lenahan, and S. E. Curry. *Phys. Rev. Lett.*, 65(2):207, 1990.

[50] V. V. Afanas'ev, A. Stesmans, and M. O. Andersson. *Phys. Rev. B*, 54:10820, 1996.

[51] D. L. Griscom, C. I. Merzbacher, R. A. Weeks, and R. A. Zuhr. *J. Non-Cryst. Solids*, 258(1):34, 1999.

[52] D. L. Griscom. *J. Appl. Phys.*, 58(7):2524, 1985.

[53] A. Stesmans. *Phys. Rev. B*, 48(4):2418, 1993.

[54] C. R. Helms and E. H. Poindexter. *Rep. Prog. Phys.*, 57(8):791, 1994.

[55] K. L. Brower. *Phys. Rev. B*, 33:4471, 1986.

[56] A. Stesmans. *Appl. Phys. Lett.*, 48(15):972, 1986.

[57] K. L. Brower. *Phys. Rev. B*, 38:9657, 1988.

[58] K. L. Brower. *Appl. Phys. Lett.*, 53:508, 1988.

[59] A. Stesmans. *Appl. Phys. Lett.*, 68(19):2723, 1996.

[60] A. Stesmans. *Appl. Phys. Lett.*, 68(15):2076, 1996.

[61] A. Stesmans and G. Van Gorp. *Appl. Phys. Lett.*, 57(25):2663, 1990.

[62] A. Stesmans. *J. Appl. Phys.*, 88(1):489, 2000.

[63] K. L. Brower and S. M. Meyers. *Appl. Phys. Lett.*, 57:162, 1990.

[64] A. Stesmans and V. V. Afanas'ev. *Phys. Rev. B*, 54(16):R11129, 1996.

[65] W. Futako, N. Mizuochi, and S. Yamasaki. *Phys. Rev. Lett.*, 92(10):105505, 2004.

[66] A. Stirling, A. Pasquarello, J. C. Charlier, and R. Car. *Phys. Rev. Lett.*, 85(13):2773, 2000.

[67] T. Sato, Y. Takeishi, H. Hara, and Y. Okamoto. *Phys. Rev. B*, 4(6):1950, 1971.

[68] M Yang, VWC Chan, KK Chan, L Shi, DM Fried, JH Stathis, AI Chou, E Gusev, JA Ott, LE Burns, MV Fischetti, and M Ieong. *IEEE Trans. Electron Devices*, 53:965, 2006.

[69] E. H. Poindexter. *Semicond. Sci. Technol.*, 4(12):961, 1989.

[70] A. Stesmans, B. Nouwen, and V. V. Afanas'ev. *J. Phys.: Condens. Matter*, 10(27):L465, 1998.

[71] J. P. Campbell and P. M. Lenahan. *Appl. Phys. Lett.*, 80(11):1945, 2002.

[72] D Hisamoto, WC Lee, J Kedzierski, H Takeuchi, K Asano, C Kuo, E Anderson, TJ King, J Bokor, and CM Hu. *IEEE Trans. Electron Devices*, 47:2320, 2000.

[73] B Goebel, D Schumann, and E Bertagnolli. *IEEE Trans. Electron Devices*, 48:897, 2001.

[74] XJ Huang, WC Lee, C Kuo, D Hisamoto, LL Chang, J Kedzierski, E Anderson, H Takeuchi, YK Choi, K Asano, V Subramanian, TJ King, J Bokor, and CM Hu. *IEEE Trans. Electron Devices*, 48:880, 2001.

[75] L. L. Chang, M. Ieong, and M. Yang. *IEEE Trans. Electron Devices*, 51(10):1621, 2004.

[76] S. Gangwal, S. Mukhopadhyay, and K. Roy. In *Proc. IEEE 2006 Custom Integrated Circuits Conf.*, page 433. 2006.

[77] M. M. de Lima, P. C. Taylor, S. Morrison, A. LeGeune, and F. C. Marques. *Phys. Rev. B*, 65:235324, 2002.

[78] R. C. Fletcher, W. A. Yager, G. L. Pearson, A. N. Holden, W. T. Read, and F. R. Merritt. *Phys. Rev.*, 94:1392, 1954.

[79] P. C. Taylor. In J. I. Pankove, editor, *Semiconductors and Semimetals*, volume 21, page 99. Academic Press, New York, 1984.

[80] D. K. Biegelsen and M. Stutzmann. *Phys. Rev. B*, 33:3006, 1986.

[81] T. Umeda, S. Yamasaki, J. Isoya, and K. Tanaka. *Phys. Rev. B*, 59(7):4849, 1999.

[82] R. A. Weeks. *J. Appl. Phys.*, 27(11):1376, 1956.

[83] R. A. Weeks. *Phys. Rev.*, 130(2):570, 1963.

[84] L. E. Halliburton, B. D. Perlson, R. A. Weeks, J. A. Weil, and M. C. Wintersgill. *Solid State Commun.*, 30(9):575, 1979.

[85] L. Skuja. *J. Non-Cryst. Solids*, 239(1-3):16, 1998.

[86] R. H. Silsbee. *J. Appl. Phys.*, 32(8):1459, 1961.

[87] G. Hochstrasser and J. F. Antonini. *Surf. Sci.*, 32(3):644, 1972.

[88] F. J. Feigl, W. B. Fowler, and K. L. Yip. *Solid State Commun.*, 14(3):225, 1974.

[89] Kwok Leung Yip and W. Beall Fowler. *Phys. Rev. B*, 11(6):2327, 1975.

[90] J. K. Rudra and W. B. Fowler. *Phys. Rev. B*, 35:8223, 1987.

[91] *Faraday Discuss.*, 106:155, 1997.

[92] *J. Am. Ceram. Soc.*, 73:3247, 1990.

[93] M. Boero, A. Pasquarello, J. Sarnthein, and R. Car. *Phys. Rev. Lett.*, 78:887, 1997.

[94] D. L. Griscom. *J. Non-Cryst. Solids*, 31(1-2):241, 1978.

[95] S. T. Pantelides, Z. Y. Lu, C. Nicklaw, T. Bakos, S. N. Rashkeev, D. M. Fleetwood, and R. D. Schrimpf. *J. Non-Cryst. Solids*, 354(2):217, 2008.

[96] P. M. Lenahan and P. V. Dressendorfer. *J. Appl. Phys.*, 55(10):3495, 1984.

[97] L. Lipkin, L. Rowan, A. Reisman, and C. K. Williams. *J. Electrochem. Soc.*, 138(7):2050, 1991.

[98] A. Kalnitsky, J. P. Ellul, E. H. Poindexter, P. J. Caplan, R. A. Lux, and A. R. Boothroyd. *J. Appl. Phys.*, 67(12):7359, 1990.

[99] V. V. Afanas'ev and A. Stesmans. *J. Phys.: Condens. Matter*, 12:2285, 2000.

[100] D. L. Griscom. *Nucl. Instrum. Methods Phys. Res. B*, 229(2):481, 1984.

[101] R. A. B. Devine and J. Arndt. *Phys. Rev. B*, 35(17):9376, 1987.

[102] A. Stesmans, K. Clemer, and V. V. Afanas'ev. *Phys. Rev. B*, 77(9):094130, 2008.

[103] A. Stesmans and V. V. Afanas'ev. *J. Appl. Phys.*, 97(3):033510, 2004.

[104] E. J. Friebele, G. H. Sigel, and D. L. Griscom. *Appl. Phys. Lett*, 28:516, 1976.

[105] Y. Hibino and H. Hanafusa. *Appl. Phys. Lett.*, 45(6):614, 1984.

[106] T. Uchino, M. Takahashi, and T. Yoko. *Appl. Phys. Lett*, 78(18):2730, 2001.

[107] G. Buscarino, S. Agnello, and F. M. Gelardi. *Phys. Rev. Lett.*, 97:135502, 2006.

[108] D. L. Griscom and M. Cook. *J. Non-Cryst. Solids*, 182(1):119, 1995.

[109] S. Mukhopadhyay, P. V. Sushko, A. M. Stoneham, and A. L. Shluger. *Phys. Rev. B*, 70(19):15, 2004.

[110] A. N. Trukhin, J. Troks, and D. L. Griscom. *J. Non-Cryst. Solids*, 353(16):1560, 2007.

[111] G. Buscarino, R. Boscaino, S. Agnello, and F. M. Gelardi. *Phys. Rev. B*, 77:155214, 2008.

[112] G. Buscarino, G. Vaccaro, S. Agnello, and F. M. Gelardi. *J. Non-Cryst. Solids*, 355(18):1092, 2009.

[113] D. L. Griscom, M. Stapelbroek, and E. J. Friebele. *J. Chem. Phys.*, 78(4):1638, 1983.

[114] F. J. Feigl and J. H. Anderson. *J. Phys. Chem. Solids*, 31:575, 1970.

[115] J. F. Conley, P. M. Lenahan, H. L. Evans, R. K. Lowry, and T. J. Morthorst. *J. Appl. Phys.*, 76:8186, 1994.

[116] W. L. Warren, D. M. Fleetwood, M. R. Shaneyfelt, J. R. Schwank, P. S. Winokur, and R. A. B. Devine. *Appl. Phys. Lett.*, 62:3330, 1993.

[117] R. Tohmon, Y. Shimogaichi, Y. Tsuta, S. Munekuni, Y. Ohki, Y. Hama, and K. Nagasawa. *Phys. Rev. B*, 41(10):7258, 1990.

[118] K. Vanheusden and A. Stesmans. *J. Appl. Phys.*, 74(1):275, 1993.

[119] L. Zhang and R. G. Leisure. *J. Appl. Phys.*, 80(7):3744, 1996.

[120] J. R. Chavez, S. P. Karna, K. Vanheusden, C. P. Brothers, R. D. Pugh, B. K. Singaraju, W. L. Warren, and R. A. B. Devine. *IEEE Trans. Nucl. Sci.*, 44:1799, 1997.

[121] SP Karna, AC Pineda, RD Pugh, WM Shedd, and TR Oldham. *IEEE Trans. Nucl. Sci.*, 47(6):2316, 2000.

[122] A. Stesmans and F. Scheerlinck. *J. Appl. Phys.*, 75(2):1047, 1994.

[123] K. Clemer, A. Stesmans, V. V. Afanas'ev, L. F. Edge, and D. G. Schlom. *J. Appl. Phys.*, 102(3):034516, 2007.

[124] A. Stesmans and F. Scheerlinck. *Phys. Rev. B*, 50(8):5204, 1994.

[125] M. E. Zvanut and T. L. Chen. In *Proc. 13th Int. Conf. Defects Insul. Mater. - ICDIM 96*, volume 239 of *Mater. Science Forum*, page 7. Trans Tech, Zurich-Uetikon, 1997.

[126] J. Vitko. *J. Appl. Phys.*, 49(11):5530, 1978.

[127] S Agnello, R Boscaino, FM Gelardi, and B Boizot. *J. Appl. Phys.*, 89(11, Part 1):6002, 2001.

[128] A. H. Edwards and G. Germann. *Nucl. Instrum. Methods Phys. Res. Sect. B*, 32(1):238, 1988.

[129] H. Nishikawa, R. Nakamura, Y. Ohki, and Y. Hama. *Phys. Rev. B*, 48(21):15584, 1993.

[130] E. Holzenkampfer, F. W. Richter, J. Stuke, and U. Voget-Grote. *J. Non-Cryst. Solids*, 32(1):327, 1979.

[131] D. L. Griscom, E. J. Friebele, K. J. Long, and J. W. Fleming. *J. Appl. Phys.*, 54(7):3743, 1983.

[132] H. Hosono and R. A. Weeks. *Phys. Rev. B*, 40(15):10543, 1989.

[133] H. Hosono, H. Kawazoe, K. Oyoshi, and S. Tanaka. *J. Non-Cryst. Solids*, 179:39, 1994.

[134] A. Stesmans and V. V. Afanas'ev. *Microelectron. Eng.*, 36(1):201, 1997.

[135] S. P. Karna and H. A. Kurtz. *Microelectron. Eng.*, 48:109, 1999.

[136] A Stirling, A Pasquarello, JC Charlier, and R Car. In HZ Massoud, IJR Baumvol, M Hirose, and EH Poindexter, editors, *Electrochem. Soc. Ser.*, page 283. 2000.

[137] J. Robertson. *Adv. Phys.*, 35(4):317, 1986.

[138] S. Charpentier, A. Kassiba, J. Emery, and M. Cauchetier. *J. Phys.: Condens. Matter*, 11:4887, 1999.

[139] Y. Nakao, S. adn Kamigaki, J. Ushio, T. Hamada, T. Ohno, M. Kato, K. Yoneda, S. Kondo, and N. Kobayashi. *Japn. K. Appl. Phys.*, 46:3351, 2007.

[140] A. Kassiba, M. Makowska-Janusik, J. Boucle, J. F. Bardeau, A. Bulou, N. Herlin, M. Mayne, and X. Armand. *Diam. Rel. Mater.*, 11(3):1243, 2002.

[141] G. Wagoner. *Phys. Rev.*, 118(3):647, 1960.

[142] SI Raider, RA Gdula, and JR Petrak. *Appl. Phys. Lett.*, 27(3):150, 1975.

[143] YC Cheng. *Progr. Surf. Sci.*, 8(5):182, 1977.

[144] Y. Miura and S. Fujieda. *J. Appl. Phys.*, 95(8):4096, 2004.

[145] M Revitz, SI Raider, and RA Gdula. *J. Vac. Sci. Technol.*, 16(2):345, 1979.

[146] A. Stesmans, V. V. Afanas'ev, F. Chen, and S. A. Campbell. *Mater. Sci. Semicond. Process*, 7(4):197, 2004.

[147] ML Green, T Sorsch, LC Feldman, EP Gusev, E Garfunkel, HC Lu, and T Gustafsson. *Appl. Phys. Lett.*, 71(20):2978, 1997.

[148] S. K. Ghandi. *VLSI Fabrication Principles: Silicon and Gallium Arsenide*. Wiley, New York, 2nd edition, 1994.

[149] A. R. Wilkinson and R. G. Elliman. *J. Appl. Phys.*, 96(7):4018, 2004.

[150] TL Chu, JR Szedon, and C Lee. *Solid-State Electron.*, 10:897, 1967.

[151] WL Warren and PM Lenahan. *Phys. Rev. B*, 42(3):1773, 1990.

[152] D. Jousse, J. Kanicki, and J. H. Stathis. *Appl. Surf. Sci.*, 39(1):412, 1989.

[153] J Robertson. *J. Philos. Mag. B*, 63(1):47, 1991.

[154] D. Kovalev, H. Heckler, G. Polisski, and F. Koch. *Phys. Stat. Solidi B*, 215(2):871, 1999.

[155] H. Takagi, H. Ogawa, Y. Yamazaki, A. Ishizaki, and T. Nakagiri. *Appl. Phys. Lett.*, 56(24):2379, 1990.

[156] M. S. Yang, J. H. Shn, and K. J. Kim. *J. Korean Phys. Soc.*, 48(6):1291, 2006.

[157] M. A. Green, J. H. Zhao, A. H. Wang, P. J. Reece, and M. Gal. *Nature*, 412(6849):805, 2001.

[158] G. Y. Sung, N. M. Park, J. H. Shin, K. H. Kim, T. Y. Kim, K. S. Cho, and C. Huh. *IEEE J. Quantum Electron.*, 12(6):1545, 2006.

[159] G. R. Lin, C. J. Lin, and C. K. Lin. *Opt. Express*, 15(5):2555, 2007.

[160] A. Madan. *Mater. Manuf. Process.*, 22(4):412, 2007.

[161] M. Dinu, R. Rapaport, G. Chen, H. R. Stuart, and R. Giles. *Bell Labs Technol. J.*, 10(3):215, 2005.

[162] L. T. Canham. *Appl. Phys. Lett.*, 57:1046, 1990.

[163] V. Lehmann and U. Goesele. *Appl. Phys. Lett.*, 58(8):856, 1991.

[164] G. C. John and V. A. Singh. *Phys. Rev. B*, 50(8):5329, 1994.

[165] L. Pavesi. *J. Appl. Phys.*, 80(1):216, 1996.

[166] S. Takeoka, M. Fujii, and S. Hayashi. *Phys. Rev. B*, 62(24):16820, 2000.

[167] G. Ledoux, J. Gong, F. Huisken, O. Guillois, and C. Reynaud. *Appl. Phys. Lett.*, 80(25):4834, 2002.

[168] J. Heitmann, F. Muller, L. X. Yi, M. Zacharias, D. Kovalev, and F. Eichhorn. *Phys. Rev. B*, 69(19):195309, 2004.

[169] A. N. Obraztsov, V. Y. Timoshenko, H. Okushi, and H. Watanabe. *Semiconductors*, 33(3):323, 1999.

[170] X. M. Bao, X. He, T. Gao, F. Yan, and H. L. Chen. *Solid State Commun.*, 109:169, 1999.

[171] L. Pavesi, L. Dal Negro, C. Mazzoleni, G. Franzo, and F. Priolo. *Nature*, 408(6811):440, 2000.

[172] B. Averboukh, R. Huber, K. W. Cheah, Y. R. Shen, G. G. Qin, Z. C. Ma, and W. H. Zong. *J. Appl. Phys.*, 92:3564, 2002.

[173] N. Daldosso, M. Luppi, S. Ossicini, E. Degoli, R. Magri, G. Dalba, P. Fornasini, R. Grisenti, F. Rocca, L. Pavesi, S. Boninelli, F. Priolo, C. Spinella, and F. Iacona. *Phys. Rev. B*, 68:085327, 2003.

[174] C. Ternon, C. Dufour, F. Gourbilleau, and R. Rizk. *Eur. Phys. J. B*, 41(3):325, 2004.

[175] M. Luppi and S. Ossicini. *J. Appl. Phys.*, 94(3):2130, 2003.

[176] E. Luppi, F. Iori, R. Magri, O. Pulci, S. Ossicini, E. Degoli, and V. Olevano. *Phys. Rev. B*, 75(3):033303, 2007.

[177] R. J. Walters, P. G. Kik, J. D. Casperson, H. A. Atwater, R. Lindstedt, M. Giorgi, and G. Bourianoff. *Appl. Phys. Lett.*, 85(13):2622, 2004.

[178] T. Puritis and J. Kaupuzs. *Physica E*, 35(1):16, 2006.

[179] R. J. Baierle, M. J. Caldas, E. Molinari, and S. Ossicini. *Solid State Commun.*, 102:545, 1997.

[180] J. X. Mei, Y. J. Rui, Z. Y. Ma, J. Xu, D. Zhu, L. Yang, X. Li, W. Li, X. F. Huang, and K. J. Chen. *Solid State Commun.*, 131(11):701, 2004.

[181] X. X. Wang, J. G. Zhang, L. Ding, B. W. Cheng, W. K. Ge, J. Z. Yu, and Q. M. Wang. *Phys. Rev. B*, 72(19):195313, 2005.

[182] M. H. Wang, D. S. Li, Z. Yuan, D. R. Yang, and D. L. Que. *Appl. Phys. Lett.*, 90(13):131903, 2007.

[183] S. Y. Turishchev, V. Terekhov, V. M. Kashkarov, E. P. Domashevskaya, S. L. Molodtsov, and D. V. Vyalykh. *J. Electron Spectrosc. Relat. Phenom.*, 156:445, 2007.

[184] A. Szekeres, T. Nikolova, A. Paneva, A. Cziraki, G. J. Kovacs, I. Lisovskyy, D. Mazunov, I. Indutnyy, and P. Shepehavyi. *Mater. Sci. Eng. B*, 124:504, 2005.

[185] O. Jambois, H. Rinnert, X. Devaux, and M. Vergnat. *J. Appl. Phys.*, 100(12):123504, 2006.

[186] T. Suominen, P. Paturi, H. Huhtinen, L. Heikkila, H. P. Hedman, R. Punkkinen, and R. Laiho. *Appl. Surf. Sci.*, 222(1-4):131, 2004.

[187] B. Pivac, I. Kovacevic, P. Dubcek, N. Radic, and S. Bernstoff. *Thin Solid Films*, 515(2):756, 2006.

[188] M. Cazzanelli, D. Navarro-Urrios, F. Riboli, N. Daldosso, L. Pavesi, J. Heitmann, L. X. Yi, R. Scholz, M. Zacharias, and U. Goesele. *J. Appl. Phys.*, 96:3164, 2004.

[189] B. Gallas, I. Stenger, C. C. Kao, S. Fisson, G. Vuye, and J. Rivory. *Phys. Rev. B*, 72(15):155319, 2005.

[190] J. Bauer, F. Fleischer, O. Breitenstein, L. Schubert, P. Werner, U. Goesele, and M. Zacharias. *Appl. Phys. Lett.*, 90, 2007.

[191] N. Nedev, D. Nesheva, E. Manolov, R. Bruggemann, S. Meier, K. Kirilov, and Z. Levi. *J. Optoelectron. Adv. Mater.*, 9(1):182, 2007.

[192] G. Hadjisavvas and P. C. Kelires. *Phys. Rev. Lett.*, 93(22):226104, 2004.

[193] C. Delerue and G. Allan. *Appl. Phys. Lett.*, 88:173117, 2006.

[194] B. K. Meyer, D. M. Hofmann, W. Stadler, V. Petrovakoch, F. Koch, P. Omling, and P. Emanuelsson. *Appl. Phys. Lett.*, 63(15):2120, 1993.

[195] U. Serincan, S. Yerci, M. Kulakci, and R. Turan. *Nucl. Instrum. Methods Phys. Res. Sect. B*, 239(4):419, 2005.

[196] A. Romanyuk, V. Spassov, and V. Melnik. *J. Appl. Phys.*, 99(3):034314, 2006.

[197] M. Zacharias, J. Heitmann, R. Scholz, U. Kahler, M. Schmidt, and J. Blasing. *Appl. Phys. Lett.*, 80(4):661, 2002.

[198] M. Fujii, A. Mimura, S. Hayashi, K. Yamamoto, C. Urakawa, and H. Ohta. *J. Appl. Phys.*, 87(4):1855, 2000.

[199] M. Fujii, A. Mimura, S. Hayashi, Y. Yamamoto, and K. Murakami. *Phys. Rev. Lett.*, 89(20):206805, 2002.

[200] K. Sumida, K. Ninomiya, M. Fujii, K. Fujio, S. Hayashi, M. Kodama, and H. Ohta. *J. Appl. Phys.*, 101(3):033504, 2007.

[201] A. Baumer, M. Stutzmann, M. S. Brandt, F. C. K. Au, and S. T. Lee. *Appl. Phys. Lett.*, 85:943, 2004.

[202] R. P. Wang. *Appl. Phys. Lett.*, 88(14):142104, 2006.

[203] V. Y. Bratus', V. A. Yukhimchuk, L. I. Berezhinsky, M. Y. Valakh, I. P. Vorona, I. Z. Indutnyi, T. T. Petrenko, P. E. Shepeliavyi, and I. B. Yanchuk. *Semiconductors*, 35:821, 2001.

[204] L. X. Yi, J. Heitmann, R. Scholz, and M. Zacharias. *J. Phys.: Condens. Matter*, 15(39):S2887, 2003.

[205] V. M. Burlakov, G. A. D. Briggs, A. P. Sutton, A. Bongiorno, and A. Pasquarello. *Phys. Rev. Lett.*, 93:135501, 2004.

[206] L. X. Yi, J. Heitmann, R. Scholz, and M. Zacharias. *Appl. Phys. Lett.*, 81(22):4248, 2002.

[207] S. Godefroo, M. Hayne, M. Jivanescu, A. Stesmans, M. Zacharias, O. I. Lebedev, G. Van Tendeloo, and V. V. Moshchalkov. *Nature Nanotechnol.*, 3:174, 2008.

[208] D. C. Yu, S. H. Lee, and G. S. Hwang. *J. Appl. Phys.*, 102(8):6, 2007.

[209] X. H. Peng, S. Ganti, A. Alizadeh, P. Sharma, S. K. Kumar, and S. K. Nayak. *Phys. Rev. B*, 74(3):035339, 2006.

[210] H. Ohta, T. Watanabe, and I. Ohdomari. *Jpn. J. Appl. Phys.*, 46(5B):3277, 2007.

[211] T. Z. Lu, M. Alexe, R. Scholz, V. Talalaev, R. J. Zhang, and M. Zacharias. *J. Appl. Phys.*, 100(1):014310, 2006.

[212] S. Godefroo. *Photoluminescence of Semiconductor Nanostructures in High Magnetic Fields*. PhD thesis, K. U. Leuven, 2007.

[213] S. C. Vitkavage, E. A. Irene, and H. Z. Massoud. *J. Appl. Phys.*, 68(10):5262, 1990.

[214] J. H. Stathis and L. Dori. *Appl. Phys. Lett.*, 58(15):1641, 1991.

[215] V. Kapaklis, C. Politis, P. Poulopoulos, and P. Schweiss. *Mater. Sci. Eng. B*, 124:475, 2005.

[216] A. Zimina, S. Eisebitt, W. Eberhardt, J. Heitmann, and M. Zacharias. *Appl. Phys. Lett.*, 88(16):163103, 2006.

[217] G. K. Celler. *Solid State Technol.*, 30:93, 1987.

[218] S. Cheylan, N. Langford, and R. G. Elliman. *Nucl. Instrum. Methods Phys. Res. Sect. B*, 166:851, 2000.

[219] G. Hadjisavvas and P. C. Kelires. *Physica E*, 38(1):99, 2007.

[220] I. N. Yassievich, A. S. Moskalenko, and A. A. Prokofiev. *Mater. Sci. Eng. C*, 27(5-8):1386, 2007.

[221] D. Pierreux and A. Stesmans. *J. Appl. Phys.*, 93(7):4331, 2003.

[222] C. J. Sofield and A. M. Stoneham. *Semicond. Sci. Technol.*, 10(3):215, 1995.

[223] C. Delerue, G. Allan, and M. Lannoo. *Phys. Rev. B*, 48:11024, 1993.

[224] L. Muller-Kirsch, A. Schliwa, O. Stier, R. Heitz, H. Kirmse, W. Neumann, and D. Bimberg. *Phys. Status Solidi B*, 224(2):349, 2001.

[225] M. Lopez, B. Garrido, C. Garcia, P. Pellegrino, A. Perez-Rodriguez, J. R. Morante, C. Bonafos, M. Carrada, and A. Claverie. *Appl. Phys. Lett.*, 80(9):1637, 2002.

[226] A. Stesmans, F. Scheerlinck, and V. Afanas'ev. *Appl. Phys. Lett.*, 64(17):2282, 1994.

[227] S. J. Pearton, A. J. Tavendale, and E. M. Lawson. *Radiat. Eff. Defects Solids*, 79(1-4):21, 1983.

[228] A. R. Wilkinson and R. G. Elliman. *Appl. Phys. Lett.*, 83(26):5512, 2003.

[229] D. Comedi, O. H. Y. Zalloum, and P. Mascher. *Appl. Phys. Lett.*, 87:213110, 2005.

[230] M. Bolduc, G. Genard, M. Yedji, D. Barba, F. Martin, G. Terwagne, and G. G. Ross. *J. Appl. Phys.*, 105:013108, 2009.

[231] D. Hiller, S. Godze, E. Pippel, P. Werner, N. Zakharov, W. Gerlach, M. Jivanescu, F. Munnik, A. Stesmans, and M. Zacharias. *Phys. Rev. B*, 2010. (*submitted*).

[232] M. Jivanescu, A. Stesmans, and M. Zacharias. *J. Appl. Phys.*, 104(10):14, 2008.

[233] V Mulloni, P Bellutti, and L Vanzetti. *Surf. Sci.*, 585:137, 2005.

[234] D. Hiller, M. Jivanescu, A. Stesmans, and M. Zacharias. *J. Appl. Phys.*, 107:084309, 2010.

[235] S. Cheylan and R. G. Elliman. *Appl. Phys. Lett.*, 78:1912, 2001.

[236] Dirk Koenig, James Rudd, Martin A. Green, and Gavin Conibeer. *Phys. Rev. B*, 78:035339, 2008.

[237] V. Levitcharsky, R. G. Saint-Jacques, Y. Q. Wang, L. Nikolova, R. Smirani, and G. G. Ross. *Surf. Coat. Technol.*, 201(19):8547, 2007.

[238] T. Shimizu-Iwayama, D. E. Hole, and P. D. Townsend. *J. Lumin.*, 80(1):235, 1999.

[239] S. Dhara. *Crit. Rev. Solid State Mater. Sci.*, 32(1):1, 2007.

[240] I. V. Ostrovskii and V. N. Lysenko. *Sov. Phys. Solid State*, 24(4):682, 1982.

[241] S. Ostapenko, N. E. Korsunskaya, M. K Sheinkman, and S. V. Koveshnikiv. *Encyclopedia of Electrical and Electronics Engineering.* Wiley, New York, 1999.

[242] S. Ostapenko. *Appl. Phys. A*, 69(2):225, 1999.

[243] D. Kruger, B. Romanyuk, V. Melnik, Y. Olikh, and R. Kurps. *J. Vac. Sci. Technol. B*, 20(4):1448, 2002.

[244] V. D. Krevchik, R. A. Muminov, and A. Y. Yafasov. *Phys. Status Solidi A*, 63:K159, 1981.

[245] V. N. Pavlovich. *Phys. Status Solidi B*, 180(1):97, 1993.

[246] W. M. Franklin and P. Sengupta. *IEEE J. Quant. Electron.*, QE 8(4):393, 1972.

[247] A. Romanyuk, P. Oelhafen, R. Kurps, and V. Melnik. *Appl. Phys. Lett.*, 90(1):3, 2007.

[248] A. Romanyuk, V. Melnik, Y. Olikh, J. Biskupek, U. Kaiser, M. Feneberg, K. Thonke, and P. Oelhafen. *J. Lumin.*, 130:87, 2010.

[249] http://www.srim.org/.

[250] M. R. Mucalo, D. G. McGavin, and N. B. Milestone. *J. Mat. Sci.*, 32(12):3271, 1997.

[251] R. Blinc, D. Arcon, P. Cevc, I. Pocsik, M. Koos, Z. Trontelj, and Z. Jaglicic. *J. Phys.: Condens. Matter*, 10:6813, 1998.

[252] H. J. Von Bardeleben, J. L. Cantin, J. J. Ganem, I. Trimaille, and E. P. Gusev. In E. Gusev, editor, *Defects in high-κ Gate Dielectric Stacks*, volume 220, page 249. Springer, Dordrecht, 2005.

[253] S. P. Karna, H. A. Kurtz, A. C. Pineda, W. M. Shedd, and R. D. Pugh. In G. Pacchioni, L. Skuja, and D. L. Griscom, editors, *Defects in SiO_2 and Related Dielectrics: Science and Technology*, page 599. Kluwer, Dordrecht, 2000.

[254] C. Kittel. *Phys. Rev.*, 73(2):155, 1948.

[255] I. Svare and G. Seidel. *Phys. Rev.*, 134(1A):A172, 1964.

[256] R. B. Flippen. *Phys. Rev. B*, 44(14):7708, 1991.

[257] J. L. Stanger, J. J. Andre, P. Turek, Y. Hosokoshi, M. Tamura, M. Kinoshita, P. Rey, J. Cirujeda, and J. Veciana. *Phys. Rev. B*, 55(13):8398, 1997.

[258] C. Kittel and E. Abrahams. *Phys. Rev.*, 90(2):238, 1953.

[259] S. J. Wyard. *Proc. Phys. Soc. London*, 86:587, 1965.

[260] B. Movaghar, L. Schweitzer, and H. Overhof. *Phil. Mag. B*, 37(6):683, 1978.

[261] E. J. Friebele, D. L. Griscom, M. Stapelbroek, and R. A. Weeks. *Phys. Rev. Lett.*, 42(20):1346, 1979.

[262] P. W. Anderson and P. P. Weiss. *Rev. Mod. Phys.*, 25:269, 1953.

[263] R. Kobo and K. Tomita. *J. Phys. Soc. Jap.*, 9:888, 1954.

[264] P. M. Richards and M. B. Salamon. *Phys. Rev. B*, 9(1):32, 1974.

[265] A. Stesmans, M. Jivanescu, S. Godefroo, and M. Zacharias. *Appl. Phys. Lett.*, 93(2), 2008.

[266] D. A. Buchanan. *IBM J. Res. Dev.*, 43(3):245, 1999.

[267] II Cheremisin, I. A. Ermolenko, I. K. Evlampiev, S. A. Popov, P. K. Turoverov, K. M. Golant, and M. O. Zabezhajlov. *Plasma Devices Oper.*, 12:1, 2004.

[268] R. A. Weeks. *J. Non-Cryst. Solids*, 179:1, 1994.

[269] B. R. Tuttle and S. T. Pantelides. *Phys. Rev. B*, 79(11), 2009.

[270] M. E. Zvanut, F. J. Feigl, W. B. Fowler, J. K. Rudra, P. J. Caplan, E. H. Poindexter, and J. D. Zook. *Appl. Phys. Lett.*, 54(21):2118, 1989.

[271] G. Buscarino, S. Agnello, and F. M. Gelardi. *Phys. Rev. Lett.*, 94:4, 2005.

[272] G. Buscarino, S. Agnello, and F. M. Gelardi. *J. Phys.: Condens. Matter*, 18:5213, 2006.

[273] A. Stesmans, R. Devine, A. G. Revesz, and H. Hughes. *IEEE Trans. Nucl. Sci.*, 37(6):2008, 1990.

[274] K. Vanheusden and A. Stesmans. *Appl. Phys. Lett.*, 62(19):2405, 1993.

[275] A. Stesmans and K. Vanheusden. *J. Appl. Phys.*, 76(3):1681, 1994.

[276] K. Hofmann, G. W. Rubloff, and D. R. Young. *J. Appl. Phys.*, 61(9):4584, 1987.

[277] R. E. Walkup and S. I. Raider. *Appl. Phys. Lett.*, 53(10):888, 1988.

[278] M. E. Zvanut, T. L. Chen, R. E. Stahlbush, E. S. Steigenvalt, and G. A. Brown. *J. Appl. Phys.*, 77(9):4329, 1995.

[279] R. A. B. Devine, D. Mathiot, W. L. Warren, D. M. Fleetwood, and B. Aspar. *Appl. Phys. Lett.*, 63(21):2926, 1993.

[280] R. A. B. Devine, D. Mathiot, W. L. Warren, and B. Aspar. *J. Appl. Phys.*, 79(5):2302, 1996.

[281] M. E. Zvanut and T. L. Chen. *Appl. Phys. Lett.*, 69(1):28, 1996.

[282] R. H. D. Nuttall and J. A. Weil. *Solid State Commun.*, 33(1):99, 1980.

[283] K. C. Snyder and W. B. Fowler. *Phys. Rev. B*, 48(18):13238, 1993.

[284] G. Pacchioni, G. Ierano, and A. M. Marquez. *Phys. Rev. Lett.*, 81(2):377, 1998.

[285] S. Mukhopadhyay, P. V. Sushko, A. H. Edwards, and A. L. Shluger. *J. Non-Cryst. Solids*, 345:703, 2004.

[286] P. E. Blochl. *Phys. Rev. B*, 62:6158, 2000.

[287] A. C. Pineda and S. P. Karna. *J. Phys. Chem. A*, 104(20):4699, 2000.

[288] N. Lopez, M. Vitiello, F. Illas, and G. Pacchioni. *J. Non-Cryst. Solids*, 271(1):56, 2000.

[289] Z. Y. Lu, C. J. Nicklaw, D. M. Fleetwood, R. D. Schrimpf, and S. T. Pantelides. *Phys. Rev. Lett.*, 89(28):285505, 2002.

[290] S. Mukhopadhyay, P. V. Sushko, V. A. Mashkov, and A. L. Shluger. *J. Phys.: Condens. Matter*, 17(8):1311, 2005.

[291] G. Buscarino, S. Agnello, and F. M. Gelardi. *Phys. Rev. B*, 73:8, 2006.

[292] L. Skuja, K. Kajihara, M. Hirano, and H. Hosono. In *14th Int. Conf. on Radiation Effects in Insulators (REI-14)*, page 2971. Elsevier Science, Caen, 2007.

[293] G. Buscarino, S. Agnello, and F. M. Gelardi. *Mod. Phys. Lett. B*, 20:451, 2006.

[294] www.lighting.philips.com.

[295] www.almazoptics.com.

[296] www.heraeus-quarzglas.com.

[297] T. Tatsumi, S. Fukuda, and S. Kadomura. *Jpn. J. Appl. Phys.*, 33(4B):2175, 1994.

[298] R. J. Powell and G. F. Derbenwi. *IEEE Trans. Nucl. Sci.*, NS18(6):99, 1971.

[299] W. L. Warren, P. M. Lenahan, and C. J. Brinker. *J. Non-Cryst. Solids*, 136(1):151, 1991.

[300] V. V. Afanas'ev and A. Stesmans. *Europhys. Lett.*, 53:233, 2001.

[301] L. Skuja, K. Kajihara, M. Hirano, and H. Hosono. *Nucl. Instrum. Methods Phys. Res. Sect. B*, 266:2971, 2008.

[302] L. Skuja, K. Kajihara, M. Hirano, A. Saitoh, and H. Hosono. *J. Non-Cryst Solids*, 352(23):2297, 2006.

[303] D. L. Griscom. *Rev. Solid State Sci.*, 4(2):565, 1990.

[304] http://www.chem.queensu.ca/eprnmr/. Epr-nmr.

[305] H. Nishikawa, R. Nakamura, R. Tohmon, Y. Ohki, Y. Sakurai, K. Nagasawa, and Y. Hama. *Phys. Rev. B*, 41(11):7828, 1990.

[306] T. E. Tsai, D. L. Griscom, and E. J. Friebele. *Phys. Rev. Lett.*, 61(4):444, 1988.

[307] S. T. Chang, J. K. Wu, and S. A. Lyon. *Appl. Phys. Lett.*, 48:662, 1986.

[308] W. L. Warren, D. M. Fleetwood, M. R. Shaneyfelt, P. S. Winokur, and R. A. B. Devine. *Phys. Rev. B*, 50:14710, 1994.

[309] A. Stesmans. *J. Non-Cryst. Solids*, 179:10, 1994.

[310] J. Isoya, J. A. Weil, and L. E. Halliburton. *J. Chem. Phys.*, 74(10):5436, 1981.

[311] N. Lopez, F. Illas, and G. Pacchioni. *J. Phys. Chem. B*, 104(23):5471, 2000.

List of publications

1. M. Jivanescu, A. Stesmans, S. Godefroo, and M. Zacharias,
Electron Spin Resonance analysis of Si nanocrystals embedded in a SiO_2 matrix,
J. Optoelectron. Adv. Mater. **9**, 721 (2007).

2. M. Jivanescu, A. Stesmans, S. Godefroo, and M. Zacharias,
Influence of point defects on the photoluminescence of phase-separated SiO/SiO_2 superstructures revealed by electron spin resonance,
Nanospec conference book, Bad-Honnef, Germany, 14 jun 2007.

3. S. Godefroo, M. Hayne, M. Jivanescu, A. Stesmans, M. Zacharias, O.I. Lebedev, G. Van Tendeloo, and V.V. Moshchalkov,
Classification and control of the origin of photoluminescence from Si nanocrystals,
Nat. Nanotechnol. **3**, 174 (2008).

4. Stesmans, M. Jivanescu, S. Godefroo, and M. Zacharias,
Paramagnetic point defects at SiO_2/nanocrystalline Si interfaces,
Appl. Phys. Lett. **93**, 023123 (2008).

5. M. Jivanescu, A. Stesmans, and M. Zacharias,
Inherent paramagnetic defects in layered nanocrystalline Si/SiO_2 superstructures,
Physica E **41**, 947 (2008).

6. M. Jivanescu, A. Stesmans, and M. Zacharias,
Inherent paramagnetic defects in layered Si/SiO_2 superstructures with Si nanocrystals,
J. Appl. Phys **104**, 103518 (2008).

7. M. Jivanescu, A. Stesmans, and A. Romanyuk,
Electron spin resonance study on the influence of in situ ultrasound applied during Si^+ implantation in SiO_2,
7th Symposium: SiO_2Advanced Dielectrics and Related Devices, Saint-Etienne, France, June 30th - July 2nd, 2008.

8. A. Romanyuk, V. Melnik, M. Jivanescu, A. Stesmans, J. Biskupek, U. Kaiser, M. Feneberg, K. Thonke, Y. Olnikh, I. Khatsevich, and P. Oelhafen,
Ultrasonically enhanced silicon mobility in Si-implanted SiO_2,
Nucl. Intrum. Methods Phys. Res. B (*submitted*).

9. D. Hiller, R. Zierold, J. Bachmann, M. Alexe, Y. Yang, J. W. Gerlach, A. Stesmans, M. Jivanescu, U. Muller, J. Vogt, H. Hilmer, P. Loper, M. Kunle, F. Munnik, K. Nielsch, and M. Zacharias,
Low temperature silicon dioxide by thermal atomic layer deposition: Investigation of material properties,
J. Appl. Phys. **107**, 064314 (2010).

10. S. Vandeleene, M. Jivanescu, A. Stesmans, J. Cuppens, M. J. Van Bael, H. Yamada, N. Sato, T. Verbiest, and G. Koeckelberghs,
Magnetic properties of substituted poly(thiophene)s in their neutral state,
Macromolecules **43**, 2910 (2010).

11. M. Jivanescu, A. Romanyuk, and A. Stesmans,
Influence of in situ applied ultrasound during Si^+ implantation in SiO_2 on paramagnetic defect generation,
J. Appl. Phys. **107**, 114307 (2010).

12. D. Hiller, M. Jivanescu, A. Stesmans, and M. Zacharias,
Pb(0) centers at the Si-nanocrystal/SiO2 interface as the dominant photoluminescence quenching defect,
J. Appl. Phys. **107**, 084309 (2010).

13. D. Hiller, S. Gotze, F. Munnik, M. Jivanescu, J. W. Gerlach, J. Vogt, E. Pippel, N. Zakharov, A. Stesmans, and M. Zacharias,
On the influence of nitrogen at the Si-nanocrystal/SiO2 interface on luminescence and interface defects,
Phys. Rev. B (*submitted*).

14. M. Jivanescu, V. V. Afanas'ev, and A. Stesmans,
Multi-frequency ESR analysis of the nature of the E'_δ defect in a-SiO_2,
(*To be submitted*).